ABSTRACT

Title of thesis: EFFECTS OF BLADE TIP SHAPE
ON ROTOR IN-GROUND-EFFECT AERODYNAMICS

Joseph Ignazio Milluzzo, Master of Science, 2012

Thesis directed by: Professor J. Gordon Leishman
Department of Aerospace Engineering

High-speed videographic flow visualization and detailed two-component particle image velocimetry (PIV) measurements were conducted to examine the wake produced by a hovering single-bladed rotor as it interacted with a horizontal ground plane. The motivation of the work was to better understand the nature of the flow field at the ground and the possible aerodynamic mechanisms that create brownout dust clouds when rotorcraft take off and land over surfaces covered with loose sediment. Rotors with four different blade tips were tested: 1. A baseline rectangular tip, 2. A simple 20° swept tip, 3. A BERP-like tip, and 4. A slotted tip. Flow visualization was performed using a high-repetition rate Nd:YLF laser that illuminated appropriately seeded flows in radial planes, with imaging performed using a high-speed CMOS camera. PIV measurements were performed in regions near the blades and at the ground plane by using a Nd:YAG laser with a CCD camera. Measurements as functions of wake age were obtained to examine the morphology of the vortical rotor wake during its interaction with the ground. The results showed that the wake was subjected to powerful curvature and straining effects as it interacted with the ground plane and was deflected into a radially outward direction

along the plane. Reintensification of the tip vortices during the interaction caused them to remain very distinct features in the flow near the ground to as old as six or more rotor revolutions. The unsteady outward flow over the ground plane was shown to have similarities to a classical turbulent wall jet, especially further away from the rotor. Flow measurements were obtained deep into the boundary layer region at the ground, and in some cases into the laminar sublayer. The results showed certain common flow features between the four blade tips, but also differences in the flows that may ultimately affect the problem of brownout. The slotted-tip was shown to be particularly effective in diffusing the tip vortices and reducing the overall intensity of the fluctuating aspects of the flow at the ground.

THE EFFECT OF BLADE TIP SHAPES ON ROTOR IN-GROUND-EFFECT AERODYNAMICS

by

Joseph Ignazio Milluzzo III

Thesis submitted to the Faculty of the Graduate School of the
University of Maryland, College Park in partial fulfillment
of the requirements for the degree of
Master of Science
2012

Advisory Committee:
Professor J. Gordon Leishman, Chair/Advisor
Associate Professor James Baeder
Assistant Professor Anya R. Jones

Acknowledgments

First and foremost I'd like to thank my advisor and thesis committee chair, Professor J. Gordon Leishman, for giving me the opportunity to work under his tutelage on this interesting and challenging project. I have learned a lot from Dr. Leishman through the years first as a Teaching Assistant moonlighting as a Research Assistant and then as a full blown Graduate Research Assistant.

I would like to thank Associate Professor James Baeder and Assistant Professor Anya R. Jones for their contributions as members of my thesis committee.

Special thanks to Anish Sydney and Juergen Rauleder for assisting in all of the experiments, trouble shooting all the problems, and all the late nights. Additional thanks to David Mayo, Joseph Ramsey and Bradley Johnson for their continued support and guidance.

I would additionally like to thank the U.S. Air Force Office of Scientific Research, who supported this work under a Multi-Disciplinary University Research Initiative, Grant No. FA9550-08-1-0406..

I want to thank all of the guys in the lab, Ben Hance, Ajay Baharani, Bharath Govindarajan, and Jamie Reel, for making it fun to come to work everyday.

My deepest appreciation to: my parents, Joseph and Karen, my sister, Kalena and my beautiful girlfriend Brianna for their unrelenting support and love. Their unconditional love enabled me to accomplish all that I have.

Table of Contents

List of Figures

Nomenclature

A	Rotor disk area, πR^2 , m^2
C_T	Rotor thrust coefficient, $T/\rho A\Omega^2 R^2$
c	Rotor blade chord, m or ft
M	image magnification
N_b	Number of blades
P	Measured rotor power, hp
r	Radial distance, m or ft
r_c	Vortex core radius, m or ft
r_o	Initial core radius, m or ft
$\bar{r}$	Non-dimensional radial distance, r/r_c
R	Radius of blade, m or ft
Re_v	Vortex Reynolds number, Γ_v/ν
Ri	Richardson number
T	Rotor thrust , lb
u, v	Velocities in r and z directions, respectively, ms^{-1}
V_{tip}	Rotor tip speed, ms^{-1}
V_θ	Swirl velocity, ms^{-1}
v_h	Hover induced velocity, $\sqrt{T/2\rho A}$, ms^{-1}
z	Downstream distance, m or ft

Greek Symbols

Γ_v	Circulation or vortex strength, m^2/s
Δt	pulse separation time, s
Δx, Δy	grid spacing, m
μ	Dynamic viscosity, kg/m s^{-1}
ν	Kinematic viscosity, $m^2 s^{-1}$
ρ	Flow density, kg/m^3
σ	Rotor solidity, $N_b c/\pi R$
σ_e	Thrust-weighted solidity, $3\int_0^1 \sigma r^2 \, dr$
ψ	Blade azimuth angle, deg
Ω	Rotational speed of the rotor, rad s^{-1}
$\bar{\omega}$	Vorticity, $m^2 s^{-1}$
ζ	Wake age, deg

Abbreviations

CCD	Charge Coupled Device
CFD	Computational Fluid Dynamics
CMOS	Complementary Metal Oxide Semiconductor
DARPA	Defense Advanced Research Projects Agency
DAQ	Data Acquisition
FFT	Fast Fourier Transform
fps	Frames-Per-Second
FV	Flow Visualization
PIV	Particle Image Velocimetry
PR-PIV	Phase-Resolved Particle Image Velocimetry
Re	Reynolds Number
TR-FV	Time-Resolved Flow Visualization

Chapter 1

Introduction

1.1 Background to the Problem of Brownout

The phenomenon of "brownout" is characterized by the rapid onset of an intense dust cloud when a rotorcraft takes off or lands over unprepared ground surfaces covered with loose, dry sediment, such as sand. The fluid dynamic interactions of the energetic rotor wake with the ground can cause the sediment particles to be mobilized, uplifted, and then suspended around the rotorcraft. An example of a helicopter encountering brownout conditions during a landing in the desert is shown in Fig. 1.1. As the size and density of the brownout cloud increases, the suspended particles rapidly begin to reduce the pilot's ability to distinguish visual references on the ground, as well as creating visual anomalies and vection illusions (i.e., perceived motion when there is none). Because pilots rely almost exclusively on visual cues when flying near the ground, the sudden loss of these cues makes the onset of brownout a serious safety of flight issue. In fact, it has been reported that up to 60% of human-factor related mishaps during military operations are because of pilot disorientation during encounters with brownout conditions [1]. Brownout can also affect civil rotorcraft operations [2], especially those performing search and rescue operations from unprepared surfaces.

Other important consequences of brownout occurrences with rotorcraft are that the uplifted and suspended dust particles create a harsh working environment for ground per-

Figure 1.1: Helicopter landing and encountering brownout conditions.

sonnel, abrade the rotor blades, and increase wear on other flight-critical mechanical components. The operational life of the rotor blades, engine components, and other rotating components etc., can all be greatly reduced because of the abrasion caused by the sediment particles. Rotor blades, in particular, can suffer from blade erosion to the point that it may affect structural integrity and need to be replaced within only tens of flight hours compared to the tens of thousands of hours for which they were otherwise designed. Engines also can suffer from serious wear after ingesting dust, opening up clearances and reducing power output. In general, the premature replacement of the mechanical components of rotorcraft operating in arid climates can significantly increase operating costs.

Recently, efforts have been undertaken in an attempt to reduce the safety of flight risks that are associated with flying helicopters under brownout conditions. The majority of this work has been on the development of advanced sensors and cockpit displays,

with the goal of increasing the pilot's situational awareness by allowing the pilot to "see" through the brownout cloud. Examples include DARPA's Sandblaster, Lockheed Martin's Pathfinder, and PhLASH by the U.S. Air Force Research Laboratory [3–5]. In addition to such efforts, pilots have progressively developed landing and take off techniques (e.g., using aspects of flight path management) to minimize continuous operations in brownout conditions. These techniques can include flying close to the ground (within two rotor diameters) at speeds high enough to outpace the developing dust cloud, combined with an increased rate of descent as the landing zone is approached. However, the use of these techniques can be dangerous and usually require the pilot to perform a "hard" landing to get the aircraft on the ground before visibility is lost in the rapidly evolving dust cloud. While the use of advanced avionics and appropriate piloting techniques should not be underestimated, they obviously do not eliminate the problem of brownout at its source.

1.2 Fluid Mechanics of Brownout

Ultimately, a more permanent solution to brownout may be required through the reduction of the overall severity of the brownout cloud. Such a solution could emerge through vehicle design from a better understanding of the underlying fluid dynamic mechanisms in the rotor wake that are responsible for the generation of brownout clouds. In this regard, anecdotal evidence at least seems to indicate that some particular helicopters are more susceptible to generating intense brownout dust clouds, while others produce somewhat less severe brownout signatures. On one hand, the helicopter in Fig. 1.2 can be seen to produce a toroidal shaped brownout cloud. In this case, the cloud is blown further

Figure 1.2: Helicopter producing a toroidal brownout cloud. (Courtesy of AWI.)

away from the landing area leaving regions of reasonably good downward and forward visibility for the pilot. On the other hand, the helicopter shown in Fig. 1.3 has a much more severe brownout signature, in which the helicopter has become completely engulfed and visibility for the pilot is seriously compromised.

As of yet, however, the reasons for such drastically different brownout signatures is still unknown, but it is highly likely that many of the effects can be correlated to the fluid dynamics in the rotor wake. In this regard, the structure and strength of the wake is known to be affected by parameters such as rotor disk loading, blade loading coefficient, number of rotor blades, number and placement of rotors, blade twist, blade tip shape, fuselage shape, etc., as well as the rotor height off the ground. Except for the limited data contained in Refs. 4–6, however, there is still a dearth of useful quantitative measurements for actual rotorcraft encountering actual brownout conditions, and such limited data cannot be used to understand the underlying physical mechanisms that may be responsible for brownout.

In an attempt to begin to understand why some rotorcraft produce worse brownout

Figure 1.3: Helicopter generating an intense brownout cloud. (Courtesy of the USMC.)

signatures than others, Milluzzo and Leishman [7] have characterized brownout severity for different rotorcraft based on the geometric characteristics and gross aerodynamic operating conditions of the main rotor(s). For example, Fig. 1.4 shows the relationship between the average downwash induced by the rotor (from momentum theory) as a function of a measure of its total wake strength (from vortex theory). Figure 1.4 also identifies three regions of brownout severity, these being based on subjective assessments of photographs and videography of rotorcraft encountering brownout conditions. While the boundaries identified by these three regions are not absolute, the results imply that the unique characteristics of each vehicle can significantly affect the severity of a brownout cloud. The first region is typical of a dust cloud that is relatively benign in nature and does not significantly attenuate required visual cues for landing (e.g., see Fig. 1.2). The next two regions are progressively worse brownout conditions that may become severe

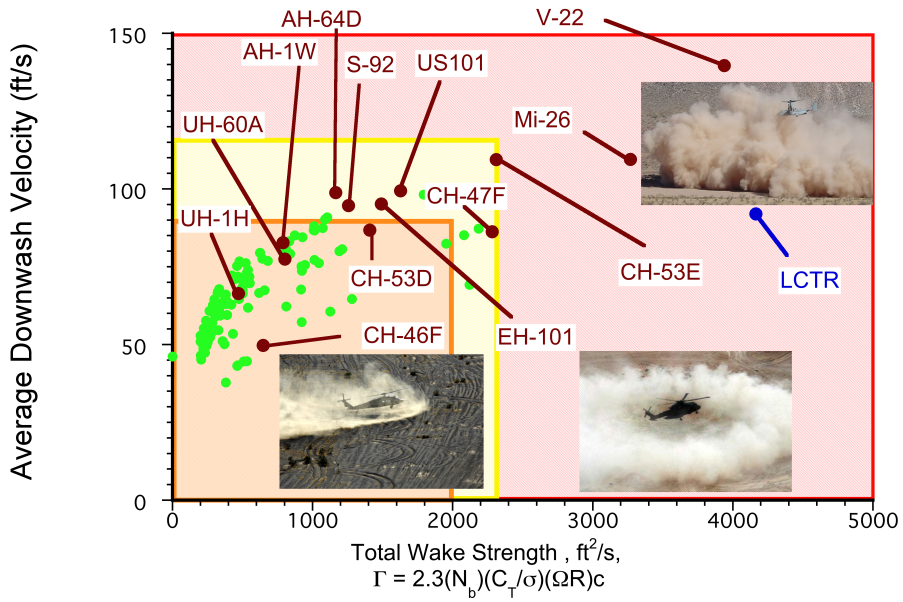

Figure 1.4: A measure of brownout severity as a function of downwash velocity and total wake strength. (From Milluzzo and Leishman [7].)

enough to affect safety of flight (e.g., see Fig. 1.3). While the "total wake strength" used in this particular correlation includes the effect of the number of blades, blade loading coefficient, rotational tip speed, rotor radius and blade chord, the significance of the characteristics of rotor wake to the problem of brownout cannot be underestimated. To this end, the goal of the present research work was to better quantify the detailed fluid dynamics of the rotor wake as it interacted with a ground plane in a laboratory context and, in particular, to examine the effects of blade tip shape on the resulting flow field at the ground.

The overall fluid dynamic complexity of brownout stems from other factors involved in the development of the dust clouds. While these factors include the nature of the flow structures generated by a rotor operating in-ground-effect (e.g., the rotor down-

wash, strength and proximity of coherent vortical flows such as the tip vortices, not to mention turbulence), the sediment characteristics (e.g., particle size, mineralogy, moisture content, compactness, etc.) also play an important role. The fluid dynamic complexity of vortical wake interactions with a solid surface cannot be underestimated, and when mobile sediment becomes part of the problem then the resulting combined flow field is of considerable complexity.

A schematic of the fluid dynamic mechanisms and the aeolian (or sedimentology) processes involved in brownout is summarized in Fig. 1.5. Fundamentally, brownout is a highly unsteady, three-dimensional fluid dynamics problem comprising two fluid phases: 1. The carrier phase (i.e., the three dimensional, unsteady flow in the rotor wake) and 2. The dispersed phase (i.e., the sediment particles that are mobilized by the rotor flow). The two fluid phases may interact with one another (e.g., momentum coupling, particle collisions, etc.), further increasing the complexity of the overall problem. Clearly, the logical approach to understanding brownout is to obtain a fundamental understanding of the underlying fluid dynamics of the rotor wake as it interacts with the ground, even in the absence of sediment.

Ultimately, the mobilization of sediment particles are influenced by the characteristics of the boundary layer flow that develops along the sediment bed (which produces shear stresses), and also by the induced effects of the discrete tip vortices that were generated by the rotor as they subsequently convect downward below the rotor and approach the bed. Once the forces and moments induced by the resulting flow on the sediment particles exceed those caused by gravity and interparticle cohesive forces, the particles will become mobilized. In this regard, it is already known that the local action of the

rotor blade tip vortices plays a particularly important role in the mobilization and uplift of sediment [8, 9]. If the particles are then subsequently uplifted into the flow, they experience additional aerodynamic and inertial forces. The particles also acquire energy from the surrounding flow as they are convected in the three-dimensional rotor wake, and can group together creating dense plumes of dust. The more severe brownout problems, however, seem to occur when the rotor reingests suspended dust particles, bombarding them back onto the sediment bed at high velocity and so ejecting more particles into suspension [10]. This type of reingestion bombardment process can rapidly intensify size and density of the developing brownout cloud. Milluzzo and Leishman [7] also characterized brownout severity in terms of the rapidity at which the cloud is produced, which can be correlated to the rotational frequency of the rotor and to the number of rotor blades.

The fluid dynamic complexity of brownout and the difficulties in the measurement of the resulting dual-phase flows has resulted in a number of computational efforts to simulate the problem. Simulations of the dust clouds have been made using a variety of methods (e.g., vortex methods, CFD in the form of a Eulerian method or Reynolds averaged Navier-Stokes methods) in an attempt to gain a better understanding of the processes involved in the development of brownout conditions. Although significant headway has been made in modeling the various elements of the problem [11–18], the overall complexity of the dual-phase nature of the flow means that the details of the flow are extremely difficult to predict. While published dust cloud simulations have produced very realistic looking results, such simulations must still be regarded as tentative. Ultimately, such simulations cannot substitute for experiments because all such simulations require validation. In particular, validation of the resulting dust clouds using meaningful optical metrics has

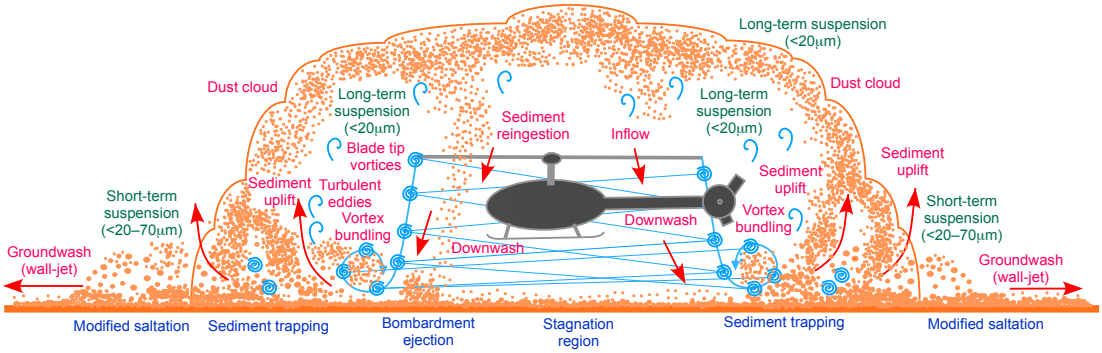

Figure 1.5: Schematic showing the modes of sediment particle motion and the resulting dust cloud generated by the rotor wake from a helicopter hovering over a ground plane.

yet to be accomplished (brownout after all is an optical transmissibility problem). Furthermore, given the overall difficulties in predicting the strengths and structure of rotor tip vortices, and in predicting the dual-phase fluid dynamics associated with the action of the vortices and a mobile sediment bed, means that quantitative predictions of brownout may still be some time away. To this end, a necessary prerequisite in fully understanding the brownout problem is to better understand the single-phase fluid dynamics of the rotor wake as it interacts with the ground, this goal being a primary focus of the present research using an experimental approach.

1.3 Rotor Wake Dynamics Near the Ground

It has been well documented that rotors operating near the ground see significant increases in performance. This outcome arises because the wake undergoes a substantial distortion from the presence of the ground (discussed next), and the consequence is a change in the inflow and angles of attack at the blades. Most experiments that have been undertaken on rotors operating in-ground-effect have documented rotor perfor-

mance [19–24], generally exploring the advantages of a rotor in-ground-effect in terms of overall vehicle performance benefits. Far fewer studies have focused on the fluid dynamics of the problem [25–32], and there have been very few measurements of the flow field in the near wall region on the ground below the rotor. There are even fewer measurements available for the case when the wake also interacts with a mobile sediment bed. However, because of the action of the rotor wake is fundamental to the mobilization and uplift of loose sediment, a prerequisite in understanding the problem of brownout is a better understanding of the evolution of the blade tip vortices as they come in proximity to the ground. In this regard, it is necessary to appreciate the differences in the wake structures that are generated by rotors operating out-of-ground-effect (OGE) to what would be obtained when the same rotor is operated in-ground-effect (IGE).

Figure 1.6a shows a smoke flow visualization of the wake of a small-scale laboratory rotor operating OGE, with the blade tip vortices, turbulent vortex sheets, and slipstream boundary being rendered visible. This image shows a radial plane through the wake, which was seeded with smoke and illuminated with a thin laser sheet. The slipstream boundary separates the high velocity flow inside the rotor wake from the quiescent flow outside the rotor wake, which gains velocity and can be seen to contract initially below the rotor as a consequence of thrust generation on the rotor. The helicoidal type vortices trailed from each blade tip convect along the slipstream boundary and persist for two to three rotor revolutions before undergoing significant diffusion. Diffusion of the tip vortices ultimately results in a far wake that slowly expands, eventually becoming a turbulent jet-like flow.

In the corresponding IGE case, as shown in Fig. 1.6b, the slipstream boundary

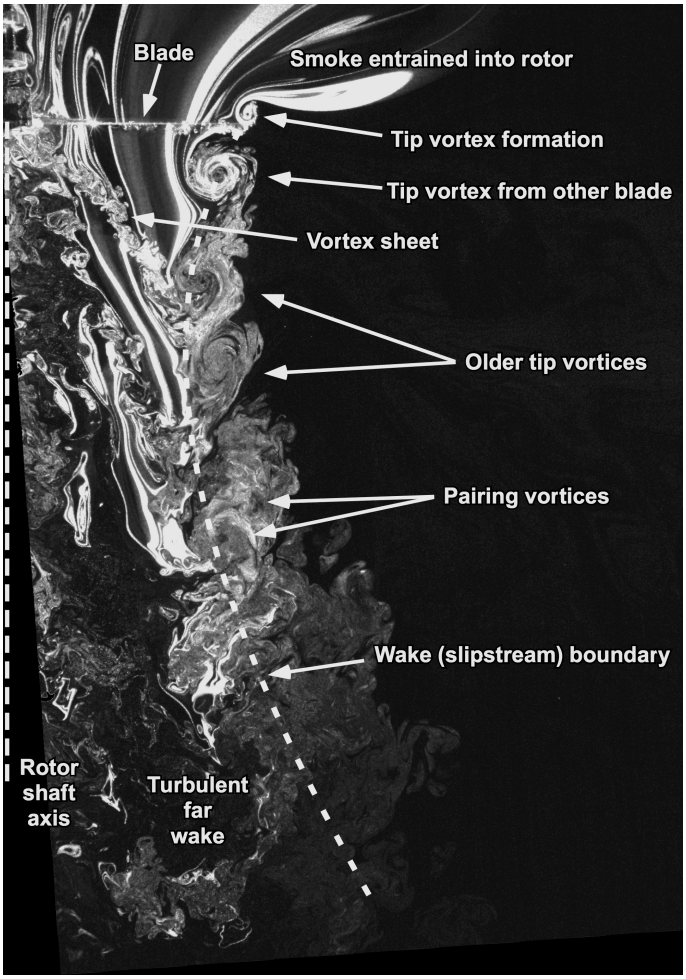

(a) Out-Of-Ground-Effect

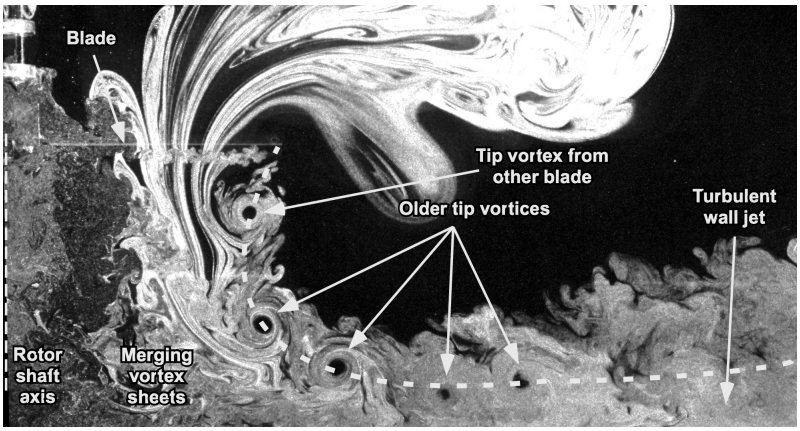

(b) In-Ground-Effect

Figure 1.6: Representative flow visualization of a 2-bladed rotor wake for a rotor operating [29]: (a) OGE; (b) IGE.

contracts below the rotor initially, but because the ground plane must be a streamline of the flow, the wake begins to turn until the flow is converted from a primarily axial (downward) flow to a primarily radial (outward) flow that expands along the ground. The tip vortices in this case can be seen to persist significantly longer (six to eight rotor revolutions) compared to the OGE case (two to three rotor revolutions). In the IGE case, the vortex filaments are also stretched as the wake flow develops along the ground plane, in the process reintensifying their vorticity [33, 34]. Ramasamy and Leishman [33] have previously examined the affects of filament stretching, and have developed a more general model for vortex growth in a velocity gradient. More recently, as the problem of brownout has become a more important research topic, there has been a greater a focus on better understanding the fluid dynamics at the ground [8, 9, 29–32]. In particular, Lee et al. [29] showed that the as rotor wake impinges on the it ground generates a complex series of unsteady shearing stresses, vortical structures, and turbulence, all of which can result in transient flow excursions. However, there is still a lot of work to do to fully understand the flow there.

The overall persistence of the tip vortices inside a rotor wake is an important issue influencing the IGE flow field below the rotor. It is already well known that the tip vortices strongly influence the induced velocities near the rotor, and can be responsible for a number of adverse affects on rotor loads and vehicle performance. Such effects include unsteady airloads and noise generated by the interaction of the rotor blades with the tip vortices (i.e., blade vortex interaction or BVI) [35, 36]. The tip vortices are also responsible for a number of rotor-airframe interaction phenomena; see Refs. [37–39]. To this end, the majority of the research previously performed on rotors has examined the wake as to

how it affects the flow field closer to the rotor (e.g., Refs. 40–52). Much of the research has been rightfully focused on better understanding the detailed structure of the blade tip vortices, which are the dominant features of the rotor wake (e.g., Refs. 53–59). While all of this work has provided a better understanding of the rotor wake and the development of the tip vortices, it has focused primarily on the flow in the near field of the rotor (up to 2 or 3 rotor revolutions old). However, as already alluded to, for the problem of brownout the understanding of the structure of the rotor wake at significantly older wake ages (4 to 6 rotor revolutions old) is much more important.

The tip vortices are known to persist in the rotor wake to relatively old wake ages, in part, because the vortex core remains mostly laminar. In particular, the high swirl velocities near the vortex core can relaminarize eddies and turbulence that are entrained from the wake [60–63], which can maintain the vortices to relatively long times even in the absence of a strain field. This relaminarization process has been discussed by Cotel and Breidenthal [60], Cotel [61], and Ramasamy & Leishman [62] in terms of the rotational stratification effect using a form of the Richardson number. In this context, the Richardson number can be viewed as a measure of the ratio of turbulence produced or consumed inside the vortex to the turbulence produced by shear. At higher Reynolds numbers and early wake ages the Richardson number (in the vortex core) is too high to allow turbulence to form, thus the core remains more laminar. In the case of a rotor operating over a surface, the general persistence of the vortices until they reach the surface (and beyond) is obviously a significant factor in understanding the effects of the rotor wake dynamics there.

1.4 Implications of the Rotor Wake Dynamics on Sediment Transport

Obviously, to make definitive conclusions about the action of the rotor wake on sediment entrainment and transport it is necessary to perform dual-phase flow studies. This was not part of the present effort. However, in light of the foregoing discussion, it is clear that necessary prerequisite in the better understanding brownout is to examine the detailed nature of the rotor wake near the ground (i.e., the single phase problem), which is the focus of the present research. Such research may lead to a better understanding of the fluid dynamic mechanisms that are ultimately responsible for mobilizing and uplifting dust particles into the rotor flow. The mechanisms responsible for sediment mobility and entrainment have already been well established for wind-driven sands and riverine flows [64–66]. However, recent studies have begun to examine how these mechanisms may differ in the dual-phase flow environment produced by a rotor [8, 9]. To this end, Johnson et al. [8] and Sydney et al. [9] have shown that the intensity of the particles uplifted and suspended near the ground is defined mostly by the action of the tip vortices rather than turbulence or other flow structures that might dominate in a nature (wind blown) environment. The vortices are responsible for increasing the shear stresses and the upwash velocities near the sediment bed, and can both mobilize and uplift particles [8,9].

As previously described, the wake below a hovering rotor is very complex, with trailed vortex filaments, turbulent vortical wake sheets, and smaller scale turbulent interactions defining the more general nature of the fluid dynamics. However, it is the trailed tip vortices that mostly characterize the developing rotor wake, so it makes sense to focus research into the tip vortices themselves. The tip region of the blade profoundly affects

the aerodynamic loading there, and defines the roll-up and initial structure of the tip vortices [67, 68]. While the roll up of the tip vortices and initial convection of the vortices is now fairly well understood, the main question that must be answered is:

1. Does tip shape also affect the vortices and the resulting flow near the ground after the wake is several revolutions old and has encountered a complex, three-dimensional, unsteady flow environment?

2. Another question that arises is: If the vortices are responsible for creating the flow environment at the ground that is ultimately responsible for brownout, then is there something that can be done to alter the structure of the tip vortices and hence reduce the severity of brownout?

Because it is known that the high swirl velocities produced by the convecting tip vortices play a significant role in the problem of brownout, spreading the vorticity and/or dissipating the vortices in some way before they reach the ground may limit the quantity of sediment particles that are uplifted.

To this end, two main methods have been previously considered in an attempt to diffuse the tight core of the tip vortex; passive and active. No method has been completely successful, and most approaches incur a rotor performance penalty. Passive methods consist of modifying the blade tip in such a way as to modify the roll up process of the tip vortex (e.g., BERP tip [69], the sub-wing tip [70, 71], slotted-tip [72–74], etc.). Active methods consist of modifying the blade geometry or controlling the flow using actuators (or another active control device) [75–77]. In the present work, the vortical flow produced by the slotted tip blade was examined, the goal being to examine the flow all

the way from the rotor to the ground plane to see if the resulting environment there may produce different fluid dynamic forces that may be less conducive to the mobilization and uplift of sediment.

1.5 Objectives of the Present Work

The main goal of the present study was to examine the fluid dynamics of a rotor wake as it interacted with a ground plane. Specifically, the work examined the structure and dynamics of the rotor wake using single blades that had four different tip shapes, namely a rectangular tip, a simple swept tip, a BERP-like tip [69], and a slotted-tip [72–74]. A series of flow experiments using particle image velocimetry (PIV) were performed with a sub-scale, one-bladed rotor system, that was operating at one rotor radius above a ground plane. The advantages of a using a one-bladed rotor are discussed later in this thesis. The flow was examined in the near field of the rotor, as well as intermediate positions as it convected below the rotor toward the ground. Another objective of the work was to assess and develop the experimental techniques using PIV to accurately measure the unsteady, near-wall flows below a rotor operating over a ground plane.

1.6 Organization of Thesis

The present chapter has discussed the problem of brownout and the general nature of the flow field generated by a rotor when the wake interactions with a ground plane. Additionally, the potential importance of the tip vortices to the problem of brownout, and possible methods of vortex modification have been given. Chapter 2 gives a comprehen-

sive description of the experimental techniques that were utilized to characterize the flow fields (high-speed flow visualization and phase-resolved particle image velocimetry) and perform rotor performance measurements. The fundamental principles, equipment used, and challenges unique to each experimental technique are explained. Chapter 3 discusses results obtained in terms of flow field characterization, velocity measurements, and performance measurements. Finally, Chapter 4 states the conclusions from the present study, and suggests additional research that could be conducted toward the better understanding of the effects of blade tip shape on problem of brownout.

Chapter 2

Description of the Experiments

2.1 Introduction

To obtain a better understanding of the complex flow below a rotor in-ground-effect operations, detailed flow visualization and particle image velocimetry (PIV) experiments were performed. This chapter provides a description of the experimental setup and the equipment used, descriptions of the experimental techniques and processes, and the challenges associated with performing these types of experiments.

2.2 Rotor System

The measurements were conducted using one-bladed rotors of radius 16 inches (0.408 m) and root chord of 1.752 inches (44.5 mm), with the blades differing only in their tip design. The blades used a NACA 2415 airfoil throughout and were untwisted. The rotor was powered by a 3-phase electric motor. An integrated thrust and torque balance was used to make rotor performance measurements, i.e., thrust and power. Flow measurements were taken with the rotor operating in the hovering state at a rotational frequency of 31 Hz (1,860 rpm) at a blade pitch angle of 4.5° (from the chord line) at one rotor radius off the ground. The rotor tip speed was 78.85 ms^{-1} (258.7 fts^{-1}), producing a nominal tip Mach number and chord Reynolds number of 0.24 and 250,000, respectively.

The use of a single-bladed rotor provided several advantages over two-, three-, and four-bladed rotor systems [78, 79]. For example, removing the influence/interaction of vortices generated by additional blades significantly reduced the levels of aperiodicity that usually occur in rotor flows. This reduction in aperiodicity greatly increased both the spatial and temporal stability of the vortex filament, which allowed aperiodicity correction techniques to the flow velocities to be applied to significantly older wake ages [78, 79], which was important for the current investigations.

In all of the present experiments, the rotor was operated in-ground-effect, one rotor radius above a circular ground plane. For these experiments, the rotor was mounted horizontally with a laser light sheet oriented perpendicular to the ground plane. A digital camera was aligned so that its viewing axis was orthogonal to the laser light sheet. The camera was uniformly focused to the desired regions of interest (ROI), as shown in Fig. 2.8. The current setup was used for both flow visualization and particle image velocimetry (PIV). The PIV technique is discussed in further detail in Section 2.6.

2.3 Performance Measurements

Performance measurements were conducted with the rotor to determine the thrust generated and power required. Mounting the rotor horizontally increased the extraneous load on the combine load/torque cell, therefore, a load cell that could withstand the large loads and still provide good accuracy and precision was selected. To this end, a load cell that could measure up to 500 lb of thrust and 500 in-lb of torque was used. The output voltage from the load cell was passed through a 32 bit analogue-to-digital (A/D)

converter that converted the signal into a discretely sampled digital representation. The A/D converter was very sensitive to changes in the output voltage from the cell, allowing it read small output signals with limited amplification or signal conditioning, eliminating the potential of introducing additional electrical interference and noise. A low-pass filter, however, was used to remove any high frequency signal components (noise).

Calibrations were performed by using known weights to determine the relationship between output voltage and applied load. Thrust and torque tares were performed without the rotor blades at rotational frequencies between 30–50 Hz. Tares were taken and then subtracted from the measured values.

2.4 Ground Plane

The measurements were performed with a rotor operating above a circular ground plane that had a diameter equal to two times the diameter of the rotor; see Fig. 2.2. To allow the ground plane to be positioned at any desired distance or orientation from the rotor, the system was mounted on a gantry with four swivelling wheels. In the present work, however, the ground plane was positioned at exactly one rotor radius from the rotor and parallel to the rotor tip path plane. Honeycomb flow conditioning screens were located upstream of the rotor, which reduced the incoming turbulence levels to less than 0.5% of the tip speed. The volume of the test cell surrounding the rotor and the ground plane was approximately 48 m^3 (1,600 ft^3).

To limit flow recirculation, it was necessary to control the nature of the rotor wake as it left the ground plane. This goal was achieved though the use of flow diverters that were

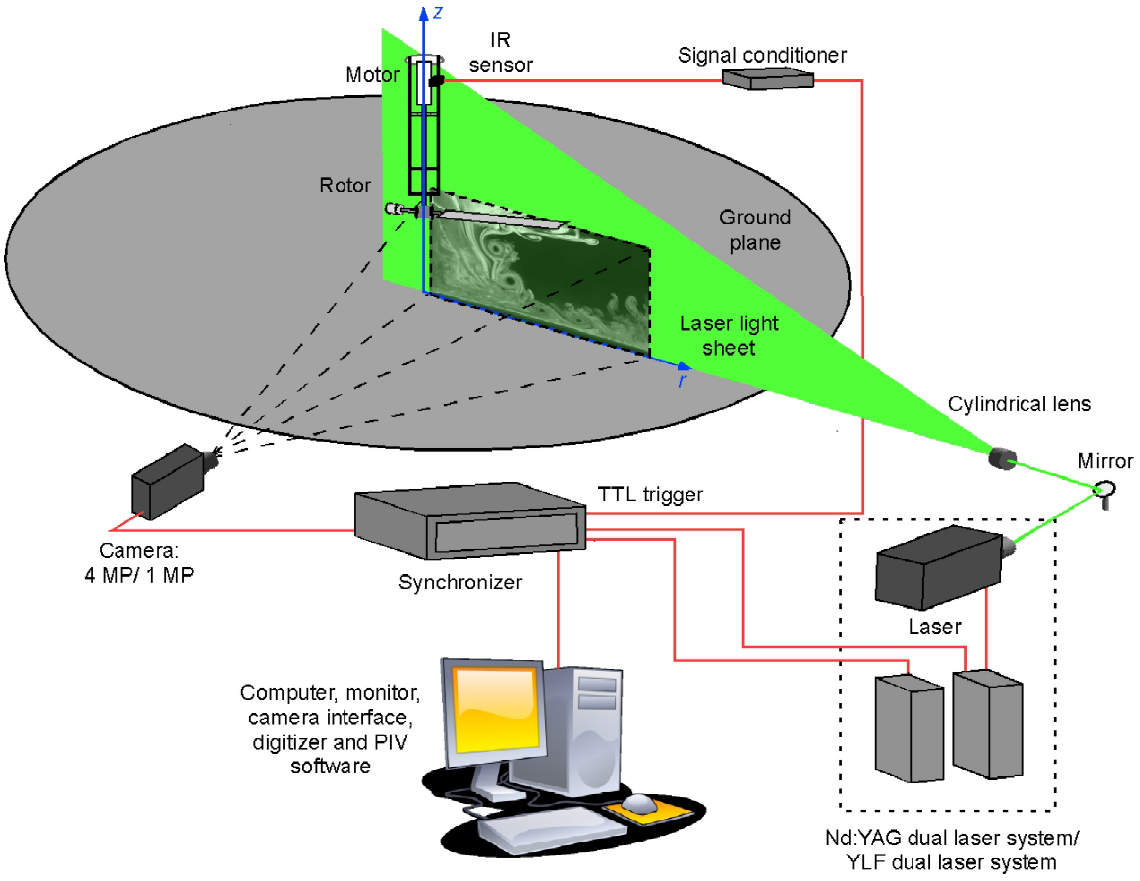

Figure 2.1: Schematic of the experimental setup showing the single-bladed rotor and the circular ground plane.

placed around the perimeter of the ground plane. The ability to obtain flow measurements close to the ground plane required that surface reflections be significantly reduced or eliminated. This objective was achieved by painting the surface with an ultra-flat-black paint, as well as using judicious laser alignment. These issues are discussed detailed in Section 2.6.7.

2.5 Blade Tips

Four different blade tip shapes were used in the experiments; see Fig. 2.4. The rectangular tip was used as the baseline case. A sheared/swept tip with a 20° sweep angle was tested because such tip designs are representative of those used on some production helicopters. The blades with the rectangular, swept, and slotted-tips had thrust-weighted solidities (i.e., $\sigma_e = 3\int_0^1 \sigma r^2 \, dr$) of 0.0347. The BERP-like blade had a slightly different thrust-weighted solidity, as will be discussed.

The slotted-tip blade tip [72–74] requires some further discussion. This blade tip comprised four internal slots that connected the leading edge of the blade to its side edge; see Fig. 2.5. The slotted-tip is a passive system that is designed to eject small-scale vorticity and turbulence directly into the tip vortex core, thereby producing higher levels of turbulence in the core thus, diffusing and substantially lowing swirl velocities in the resulting downstream wake [72–74]. Measurements of hover performance have shown that the slotted-tip blade produces only a small ($< 2\%$) profile power penalty [73].

The fourth blade tip had a BERP-like planform shape [69] with a linear reduction in blade thickness to 8% thickness-to-chord ratio over the outer 5% of its span. The

thrust-weighted solidity of this blade was 0.0348, which was slightly higher than the other blades. This blade was selected because of its unique planform (large variations in chord, highly swept and tapered tip) that may effect the roll up of the tip vortex, thereby altering the corresponding rotor wake.

2.6 Particle Image Velocimetry (PIV)

Flow visualization and particle image velocimetry (PIV) were both used in the current experiments. Each technique required different equipment (lasers, cameras, etc.), however, the basic set up was the same. To obtain a thin light sheet in the desired region of interest, the laser was fired off a mirror (rated for the high intensity beam produced by the laser) though a spherical and convex lens. A spherical lens converted the laser beam into sheet form and a convex lens thinned the sheet to ≈ 1 mm [29, 80]. The axis of the camera was oriented orthogonal to the light sheet, focused to the desired regions in the rotor wake, and then synchronized with the pulsing of the laser. The process of synchronizing the laser and camera is discussed further in Section 2.6.5.

The non-intrusive measurement technique of particle image velocimetry (PIV) was used because it provides a significant advantage over other flow field measurement techniques (e.g. LDV). The main advantage of PIV is the ability to measure the velocity in a plane at an instant in time. The flow is seeded with sub-micron tracer particles that are illuminated twice consecutively over a short time interval (Δt), which is on the order of microseconds. A pair of images (image pair) is generated when the Mie scattering from the tracer particles is recorded. The resulting image pair is then sub-divided into thou-

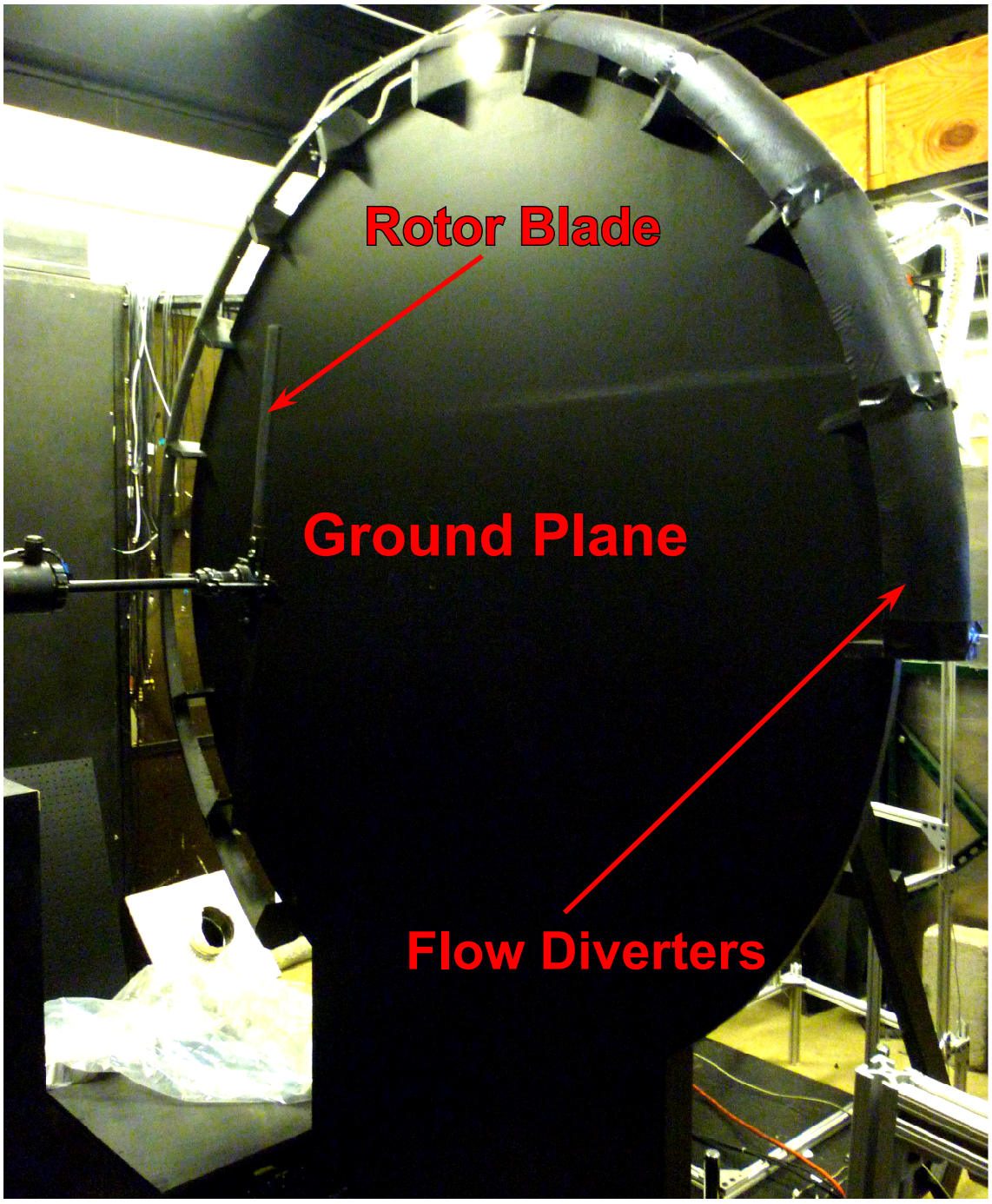

Figure 2.2: Photograph of the rotor and ground plane used for flow measurements of a rotor operating in-ground-effect.

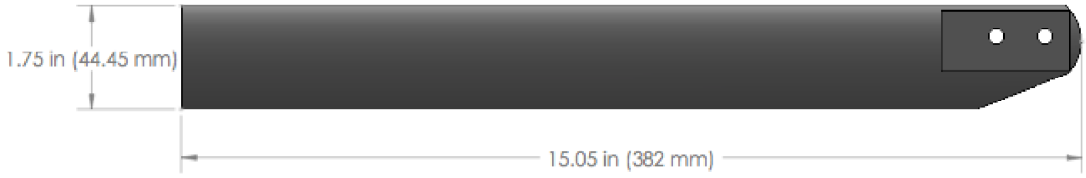

Figure 2.3: Rectangular rotor blade with representative chord and radius dimensions.

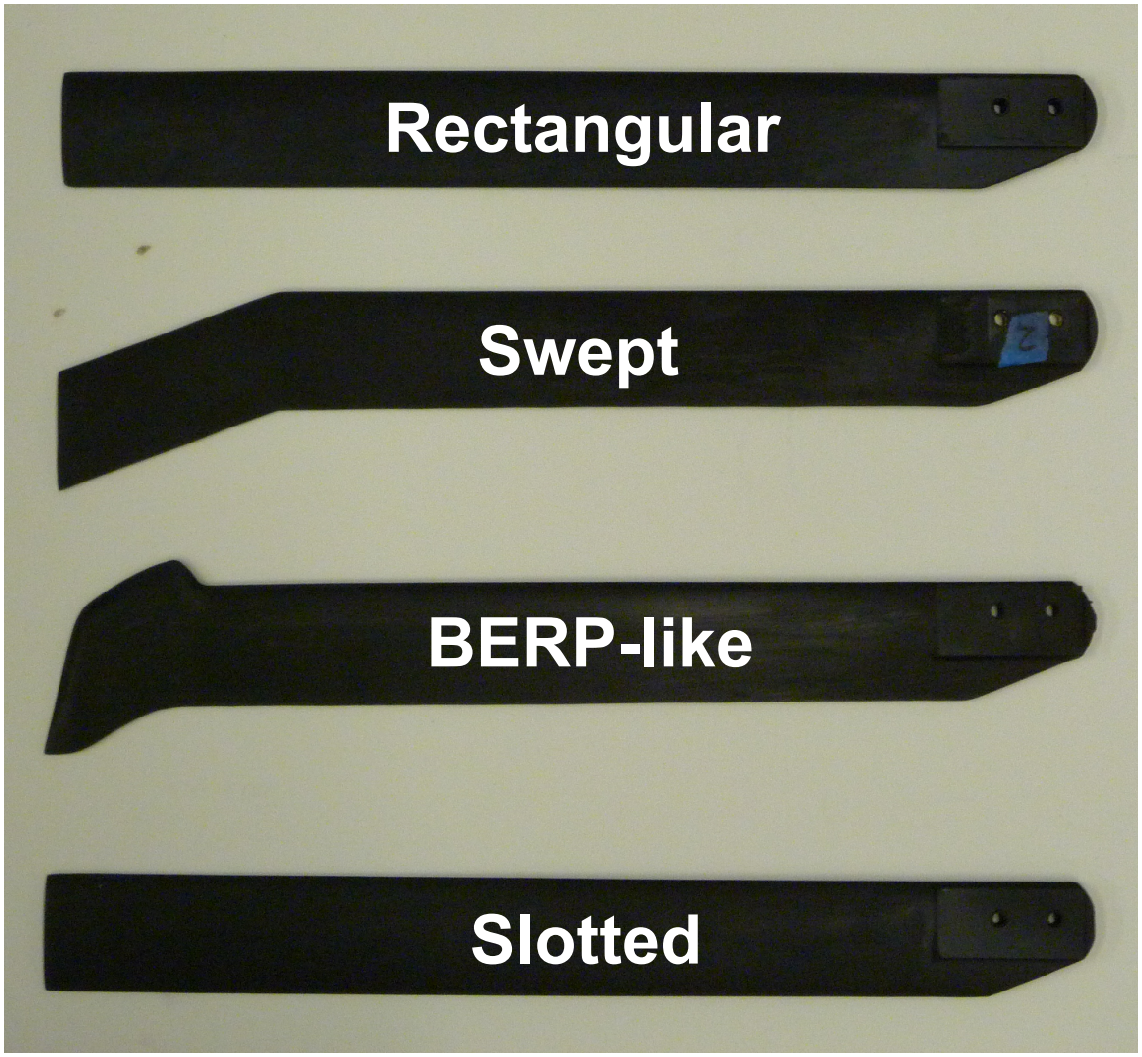

Figure 2.4: Photograph of the blades that were tested (bottom to top): Slotted-tip blade, BERP-like blade, 20° swept tip blade, and the reference rectangular blade.

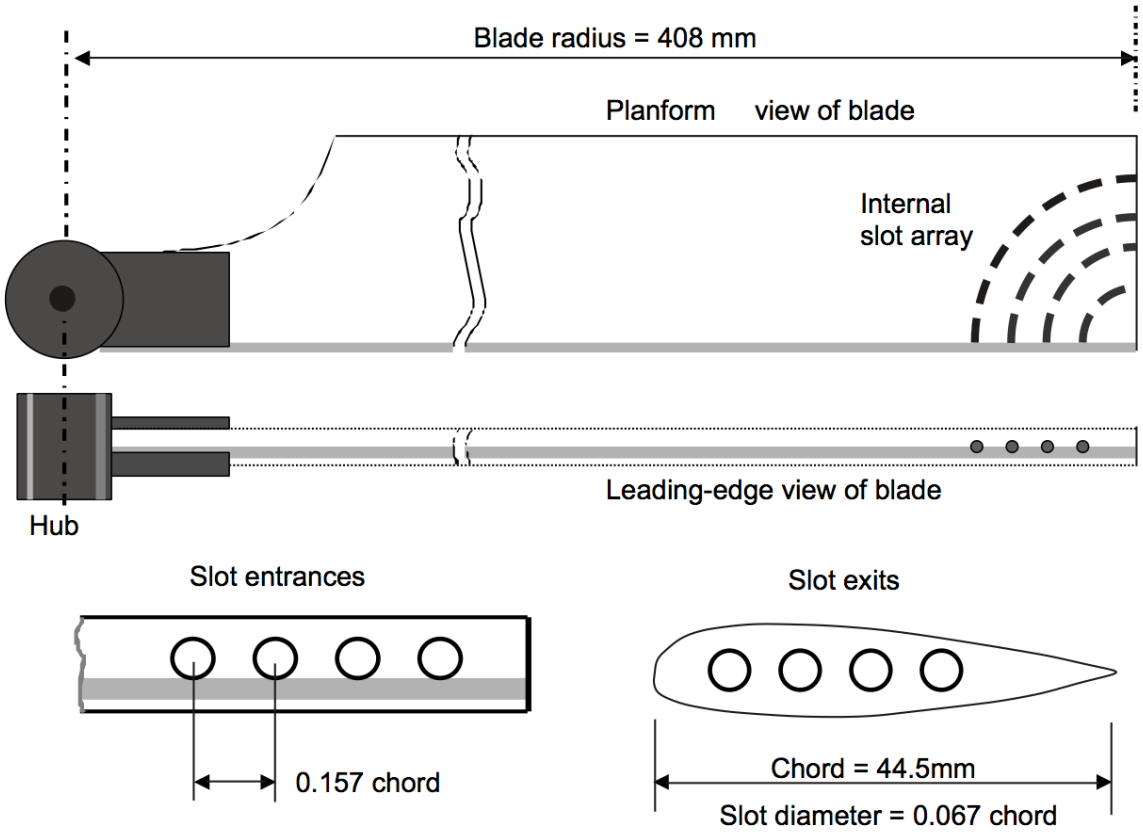

Figure 2.5: Details of the blade with the slotted-tip, the four slots passing from the leading edge to the side edge of the blade.

sands of smaller interrogation areas having base-2 dimensions (i.e., 16x16, 32x32, 64x64 pixels) [81]. A cross-correlation algorithm was used to calculate the pixel displacements (between the two images) of the seed particles in the x and y direction (Δx, Δy) to sub-pixel accuracy for each interrogation area. The displacements are calculated assuming the particles in each interrogation area are displaced an equal amount between the two images, yielding a single velocity vector for each interrogation area.

A Fast Fourier Transform (FFT) algorithm was used to perform the cross-correlation in the frequency domain before converting back to the spatial domain [82, 83]. The correlated pixel displacement (Δx, Δy) in an interrogation area is then used to calculate the local velocity vectors by using the equation

$$(U,V) = \frac{(\Delta x, \Delta y)}{M\Delta t} \tag{2.1}$$

where M is the image magnification calculated by imaging an object of known dimensions (e.g., a scale) and determining the corresponding number of pixels in the image. This procedure is repeated for all the interrogation areas focused by the camera, as shown for a typical vortex flow in Fig. 2.6.

2.6.1 Seeding

Seed particles were produced by combining mineral oil and pressurized nitrogen, and heating them until the mixture vaporized. As the vaporized mixture interacted with the ambient air, it cooled rapidly and condensed into a dense white fog. From previous calibration, 95% of the seed particles were determined to be 0.2 μm in diameter. Seed particles of 0.2 μm have been shown to minimize particle tracking errors for velocity

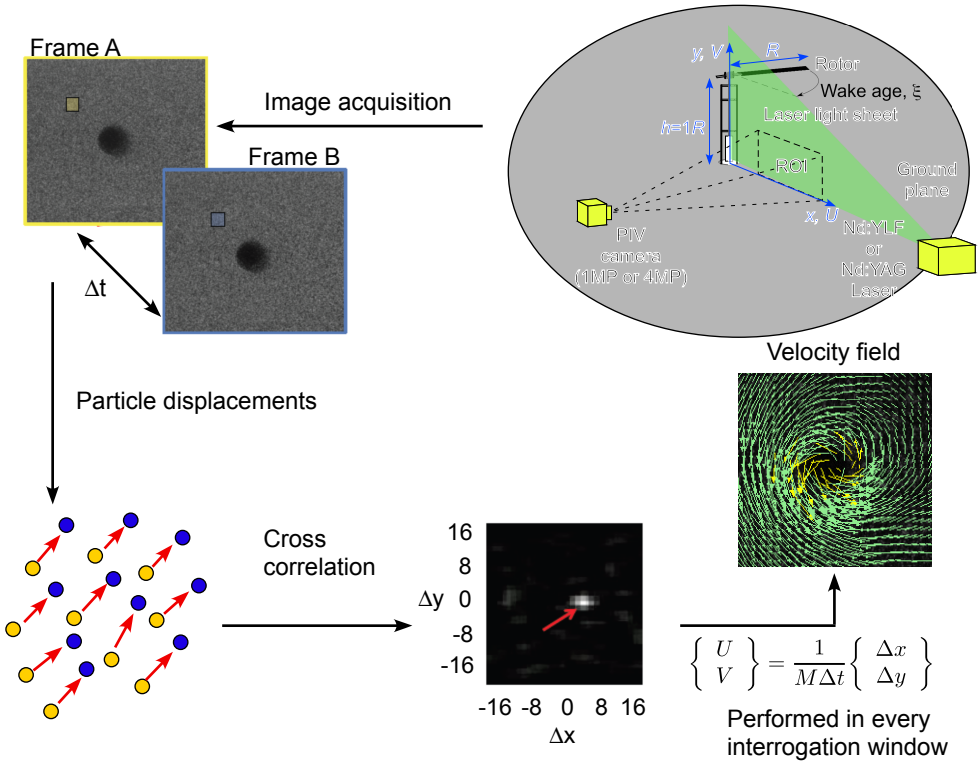

Figure 2.6: Schematic of PIV methodology.

fields common in these types of experiments [84].

For the flow visualization the seed was introduced strategically into the flow field through a series of ducts, which produced concentrated bands of seed particles into the flow, increasing the amount of seed entrained into the desired flow structures. When compared to PIV, this process better highlighted the tip vortices and the other important flow structures. However, the seeding required for PIV experiments was different from the seeding used for flow visualization, in that a minimum amount of uniformly dispersed seed was required. Dispersing the seed uniformly allowed individual particles to be more easily distinguished in the PIV images.

2.6.2 Time-Resolved Flow Visualization Equipment

A dual Nd:YLF laser was used for the time-resolved measurements, which emitted 527 nm light with 20 mJ/pulse when fired at 1,500 Hz. The CMOS high-speed camera had the ability to capture 1,024-by-1,024 pixel resolution images at up to 3,000 frames per second (fps), and was fitted with a 85 mm lens set to an f-stop of 1.8. In the present experiments, the camera was set to capture at 1,500 fps because this frame rate gave a minimal penalty on intensity transference. In the present experiments, 500 image pairs were acquired per run.

2.6.3 Phase-Resolved PIV Equipment

The phase-resolved measurements used a 4 mega-pixel (MP) CCD camera that could capture 15 fps at its full 2,048-by-2,048 pixel resolution. In this case a Nd:YAG PIV

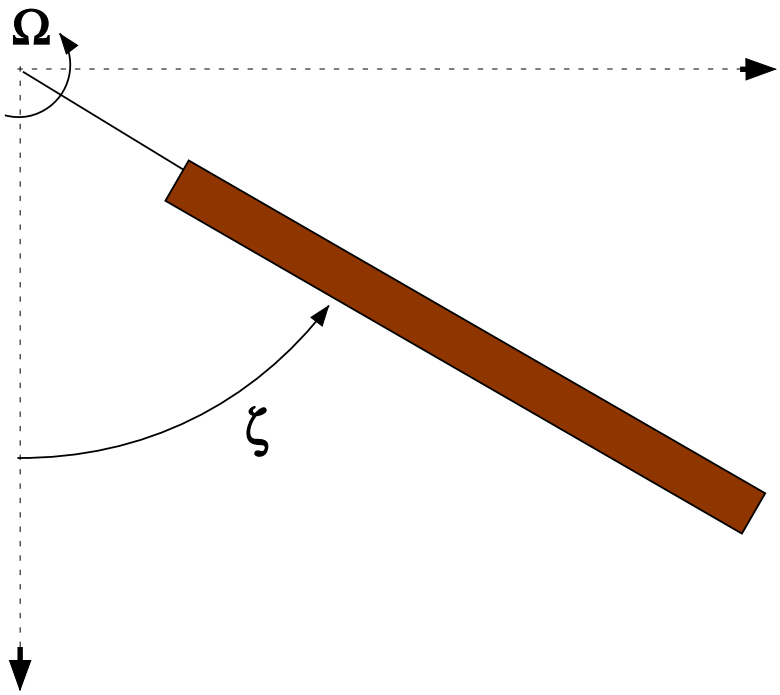

Figure 2.7: Wake age schematic.

laser was used, which emitted 532 nm light with 200 mJ/pulse when fired at 15 Hz. Because the rotor rotational frequency (31 Hz) was greater than the maximum imaging rate of the system (15 Hz), electronics and software were used to synchronize the rotor and imaging system. An infra-red (IR) sensor was used to measure the rotational frequency of the rotor. The one-per-rev output signal was converted into a square wave pulse before being read into a timing hub, which converted the square wave into a TTL signal that pulsed approximately every second rotor revolution. The timing hub could modify the TTL signal with a phase delay that allowed any desired blade azimuthal position, ψ, to be imaged, thus permitting the experiments to be conducted as a function of wake age, ζ. Wake age is a measure of the time since the vortex was generated, in terms of the angular displacement (degrees of rotor rotation) of the corresponding blade; see Fig. 2.7.

2.6.4 Time-Resolved Flow Visualization

As discussed previously, two types of experiments were conducted: flow visualization and PIV. Detailed flow visualization experiments in the rotor wake were performed using a time-resolved measurement system with a high-speed digital camera and a Nd:YLF laser that could fire at a high repetition rate. The objective in this case was to examine carefully the temporal evolution of the wake generated by each of the rotor blades, and to track the individual vortical flow structures and eddies downstream as they were convected toward the ground plane.

For larger field of views, the low resolution and intensity available with the high-speed camera (1,024-by-1,024 pixels) and YLF laser (20mJ/pulse) significantly limited the ability to resolve the high velocity gradients in the tip vortices and near the ground, reducing the maximum field of view. For this reason, more detailed PIV measurements were performed using the phase-resolved system, i.e., the Nd:YAG laser and a 4 MP camera.

2.6.5 Phase-Resolved PIV (PR-PIV)

Given the same region of interest and interrogation window size, the phase-resolved system produced images that had four times the spatial resolution compared to those that could be obtained with the time-resolved system. This capability better resolved the swirl velocities in the tip vortices and the velocity gradients in the boundary layer region at the ground plane. When using this system, the eddies and turbulent flow structures near the ground could be resolved to a distance of $0.2\%R$ from the surface when using a 105 mm

lens, and as close as 0.1%R(i.e. 0.9%c) from the surface when using a 210 mm lens.

The disadvantage of the phase-resolved system is that it could only acquire data at a sub-multiple of the rotor frequency, so the individual flow structures could not be continuously tracked in time throughout the flow. However, the time-resolved flow visualization results were used to target the location of the flow structures, and to determine the regions and wake ages that required more detailed studies when using the PR-PIV system.

2.6.6 Regions of Interest (ROI)

PIV was performed in the regions of interest (ROI) that are indicated in Fig. 2.8. The dual lasers were fired with a pulse separation time of 10 μs in ROIs 1, 2, 3 and 6, and at 20 μs in ROIs 4 and 5. Separate interrogation regions were needed to track the wake down to the ground plane while still retaining the necessary spatial resolution in the measurements. In ROIs 1–5, a 105 mm lens set to an f-stop of 2.8 was used, and in ROI 6 a 210 mm lens with a f-stop of 5.6 was used.

In ROI 1–5, 100 PIV image pairs were taken at wake age increments of 30° and sometimes finer. A sample size of 100 image pairs has been shown to provide enough statistical data to ensure convergence of the vortex characteristics [31]. For ROI 1–3 the necessary spatial resolution, to resolve the flow structures, was achieved using an interrogation window of 16-by-16 pixels throughout, yielding a minimum of 6–8 measurement points inside the vortex cores.

The cross-correlation processing was performed using an image deformation method with a 50% overlap [85]. This method iterated from an interrogation window size of

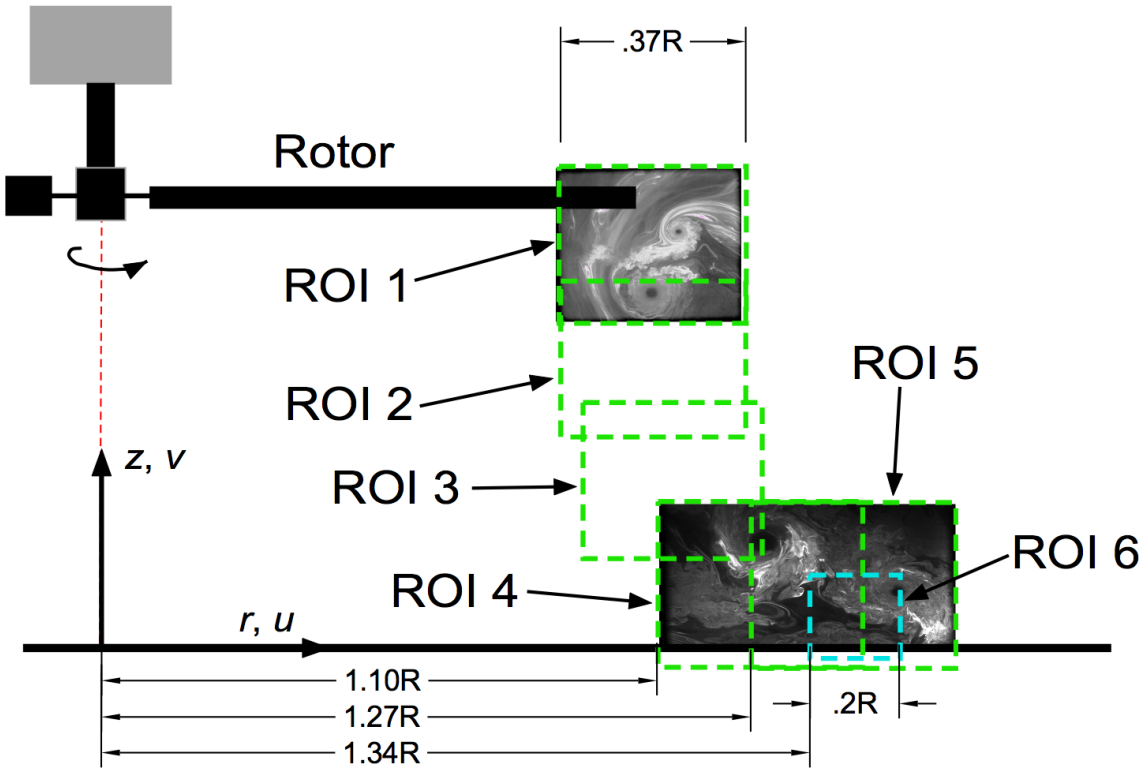

Figure 2.8: Regions of interest (ROI) in the present work, which encompassed ROIs at the blades and at the ground plane.

48-by-48 pixel to a 16-by-16-pixel interrogation window size. The validation of the vectors was performed using a two step process. A local vector validation used the 3-by-3 neighboring vectors with a universal median test, which output into a vector conditioning program that again used the 3-by-3 neighboring vectors but with the local mean instead of the universal median. Spurious vectors were determined using a Gaussian peak with a stringent signal-to-noise ratio of 1.5. Images containing more than 5% spurious vectors were removed. Less than 2% of the total acquired vectors were rejected in the present experiments.

2.6.7 Challenges in Near Wall PIV Measurements

There are several significant challenges associated with performing PIV measurements near solid boundaries, with surface reflections from the incident laser light being on of the most important. When the laser light reflects off a solid surface, the resulting intensity can be significantly higher than the Mie scattering from the seed particles, making it difficult to obtain good cross-correlations for example, see Fig. 2.9a.

Several techniques were implemented to remove these reflections such as paint selection, judicious alignment of the laser with the ground plane, and periodic cleaning of the ground plane to remove any oil from the condensed seed particles; see Fig. 2.9b. Several paint types were tested to determine the one that was most effective in reducing reflections, the best being an ultra-flat black paint. The alignment of the laser was particularly important for reducing the reflections. To this end, the laser optics were positioned such that the ground plane bisected the light sheet. This approach resulted in the

light waves propagating more parallel to the ground plane surface, significantly reducing interactions and the reflections that would otherwise result.

The correlation technique used in ROIs 4 and 5 was significantly more complicated [86] because these regions contained both vortical and radial (wall-jet) type flows. To fully resolve both types of flow features, these ROIs were each divided into two regions. A cut was first made approximately 5 mm (1.2%R or 11%c) above the ground plane. Above this cut was the more vortical part of the flow, and this region was analyzed in the same manner as in ROI 1–3 except that a 24-by-24-pixel interrogation window was used. Below this region, the downwash from the rotor had turned (or was beginning to turn) to form a radially expanding turbulent flow along the wall. To measure the resulting high velocity gradients in the wall-normal direction, the interrogation window was modified into rectangular shapes of 8-by-24 pixels. This approach permitted measurements with excellent spatial resolution near the ground, and also allowed the small-scale fluctuations from turbulence to be resolved within the boundary layer region of the flow.

The cross-correlation method for the near-wall region used a recursive Nyquist grid with a 50% overlap that was varied from 8-by-48 to 8-by-24 pixels using the same FFT correlator, Gaussian peak, and signal-to-noise ratio requirement that was used for ROI 1–3. In these near-wall regions, the laser pulse separation time was set to 20μs, which gave acceptable levels of maximum particle displacement for the interrogation window size. Because the flow here had lower average velocities and smaller velocity gradients than for the younger wake ages, a larger pulse separation time could be used.

ROI 6 used a 10μs pulse separation time. The recursive grid for this boundary layer flow region was changed to 8-by-16 pixels and the vortical region of the flow was

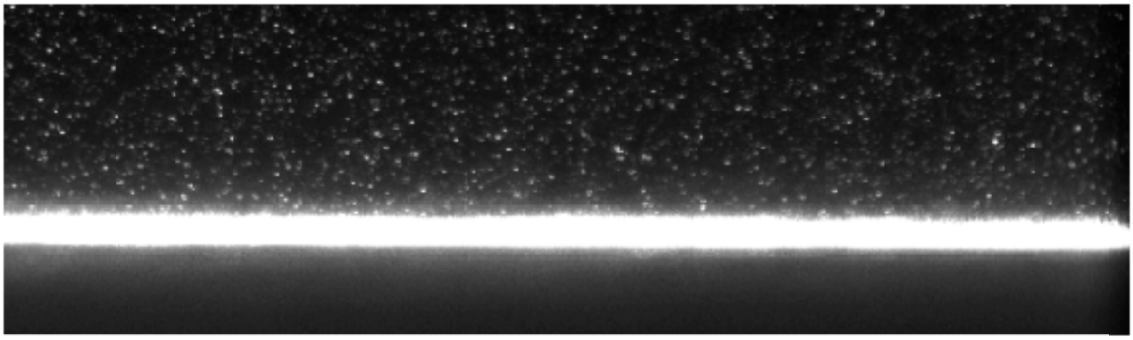

(a) Before

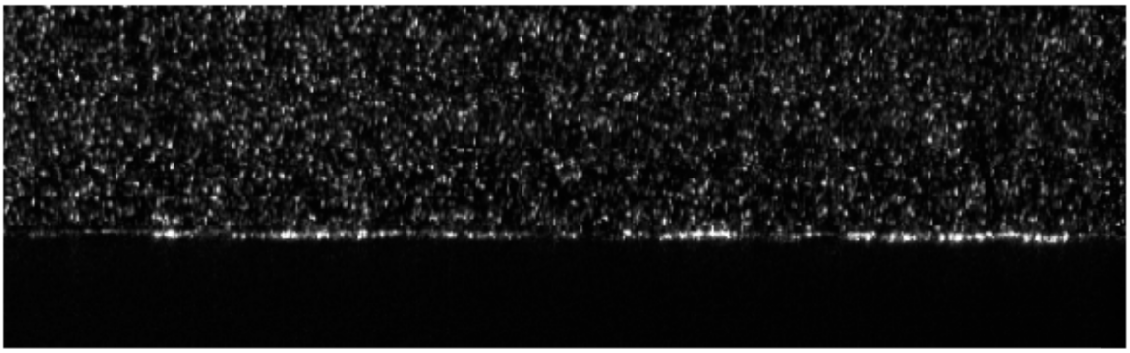

(b) After

Figure 2.9: High-intensity reflections off the ground plane (a) before and (b) after the implementation of reflections reduction techniques.

analyzed using a 16-by-16 grid. In this region, the flows were studied in 60° increments of wake age.

2.7 Uncertainties in the PIV Measurements

Sources of uncertainty in the flow measurements using PIV include tracking errors of the tracer particles, background noise, interrogation window size, pulse separation time, laser light reflections. Tracer particle errors arise because the seed particles do not perfectly follow the flow. However, this source of error is generally very small with the size of seed particle that was used in the present work. Background noise is a result of noise in the camera signal manifests as artificial intensities in the raw image that can result in inaccurate correlations. To limit such errors, a stringent signal-to-noise ratio was used to assess the validity of each vector. The interrogation window size and pulse separation time were chosen such that there was minimal flow curvature or shearing within each window. However, in a flow with significant vorticity there must always be at least some deviation of the flow (from a linear path) in each interrogation window. The image deformation method was implemented to help alleviate this source of error. Laser light reflections, which manifest in a manner similar to background noise, obscure the tracer particles in the raw image resulting in a complete loss of signal or erroneous vectors. For the present work, the estimated uncertainty in the pixel displacements used to measure the velocity fields was 4.7%. Using the uncertainties in the values of the pulse separation time, Δt (0.005%), and magnification factor, M (0.95%), with the estimated uncertainty in pixel displacement, the total propagated uncertainty in the flow velocity measurements

was estimated to be 4.9% using the equation

$$\Delta U = \sqrt{\left(\Delta\varepsilon_{\Delta x}\frac{\partial U}{\partial \Delta x}\right)^2 + \left(\Delta\varepsilon_{\Delta t}\frac{\partial U}{\partial \Delta t}\right)^2 + \left(\Delta\varepsilon_{M}\frac{\partial U}{\partial M}\right)^2} \tag{2.2}$$

where $\varepsilon_{\Delta x}$,$\varepsilon_{\Delta t}$, ε_M correspond to the uncertainties in the pixel displacement, pulse separation time and magnification factor.

2.8 Summary

This chapter discussed the experimental setup and methodologies used to obtain measurements below a single-bladed rotor (with varying blade tip shape) operating in-ground-effect. The tip shapes examined were a baseline rectangular, a simple swept, a BERP-like, and slotted-tip blade. Measurements of the rotor performance were also made at a constant blade collective pitch and varying rotational frequency. The technical challenges involved in data acquisition have been described. Estimates of the various sources of errors in the measurements were also discussed.

Chapter 3

Results and Discussion

3.1 Introduction

As discussed in Chapter 1, the wake generated by a hovering rotor can be affected by the shape of the blade tip [67, 87, 88]. Specifically, the blade tip affects the strength (i.e., $\Gamma_v = \oint \vec{V} \cdot d\vec{s}$) and flow structure of the trailed vortices. The subsequent velocity field induced at the ground may also be affected by blade tip shape, and so may potentially affect the brownout signature generated the rotor. However, the question that must be answered first is whether tip shape significantly affects the flow near the ground after the wake has aged several revolutions in the flow and encountered significant amounts of turbulence, and has potentially undergone complex interactions with other turbulent flow structures. To this end, the present study has measured the flow fields generated by four single bladed rotors that had different tip shapes, as described in Chapter 2.

3.2 Performance Measurements

Rotor performance measurements were taken using a combination load and torque cell, as discussed in detail in Section 2.3. Figure 3.1 shows the measured power polars for the four different blade tip shapes. In this case, the tests were performed at a constant blade pitch while varying the rotational frequency. Table 3.1 documents the rotor per-

	Rectangular	Swept	BERP-like	Slotted
Thrust, lb	1.60	1.81	2.04	1.27
Disk loading, lb/ft^2	0.27	0.32	0.37	0.23
Hover induced velocity, v_h, ft/s	7.77	8.26	8.76	6.92
Thrust coefficient, C_T	0.0018	0.0020	0.0023	0.0014
% Difference in thrust from baseline	0.0	+12.3	+24.2	-23.0

Table 3.1: Rotor performance for the rectangular, swept, BERP-like, and slotted blade tips at the operating conditions of 31 Hz rotational frequency and 4.5° collective pitch.

formance at these operating conditions. Because at a constant blade pitch the operating thrust varied somewhat for each of the blades, most of the results shown in this thesis were normalized by the hover induced velocity (i.e., $v_h = \sqrt{T/2\rho A}$) as obtained from the momentum theory of rotors [89]. This simple normalization approach provided a consistent basis with which to compare the differences in the flows that were generated by rotors when they were operated at slightly different thrusts. With the current rotor design, it was not possible to conduct tests at exactly the same rotor thrust. More recently, the rotor rig has been configured with variable collective pitch capability so that future tests can be conducted at exactly the same thrust and/or blade loading.

3.3 Flow at the Blades

To fully understand the resulting flow on the ground plane it is necessary to first analyze the wake structures generated in the near field of the rotor. To this end, time-resolved flow visualization and phase-resolved PIV were conducted in the region directly

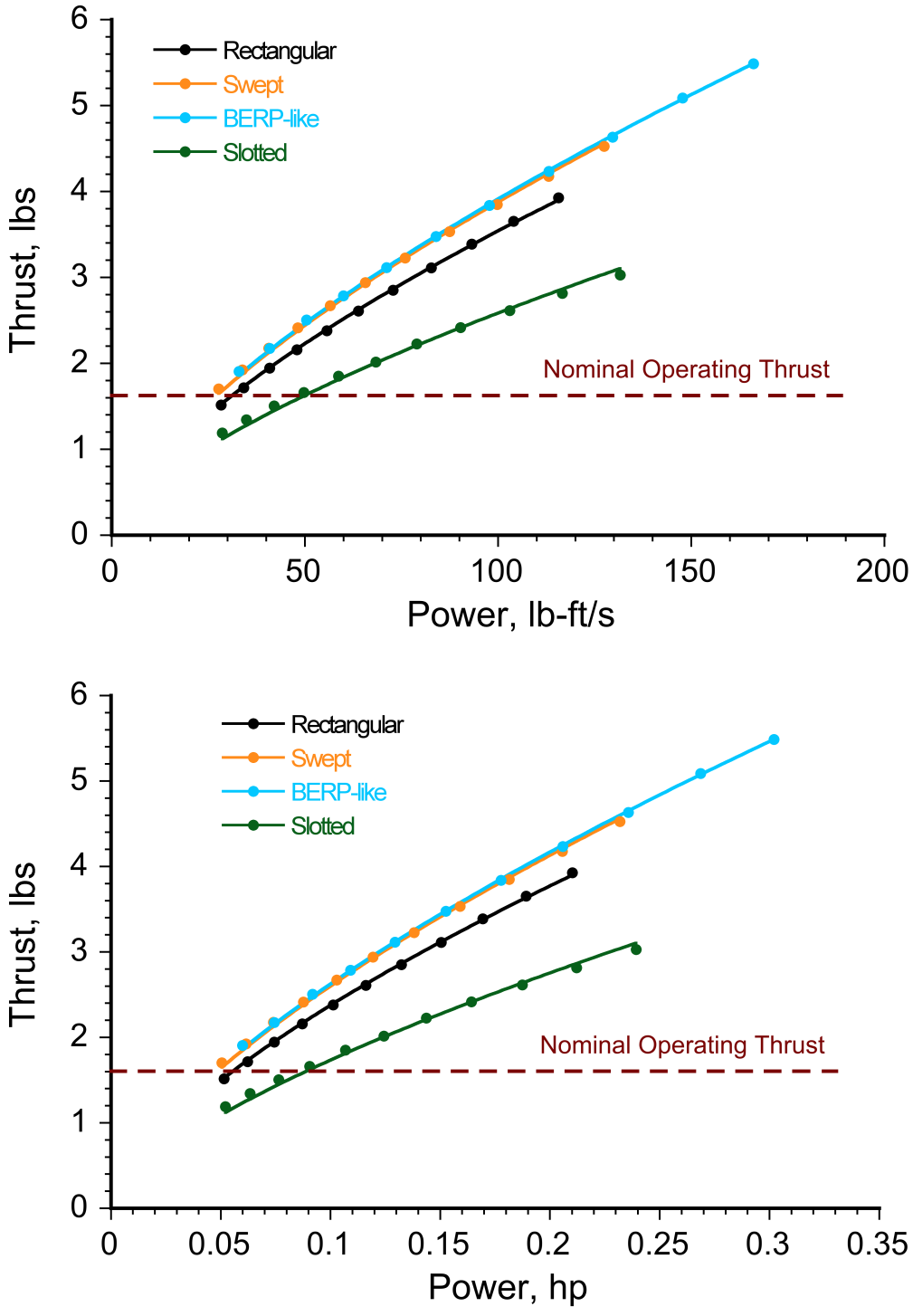

Figure 3.1: Plot of thrust versus power for a constant pitch and varying rotational frequencies (30–50 Hz).

below the blades (in ROI 1), as shown in Figs. 3.2 and 3.3. It is important to note that the field of view for the flow visualization images is slightly larger than the that of the PIV images. Also, to limit image congestion, only every 3rd measured vector is plotted in these plots over contours of instantaneous total velocity.

Figure 3.2 shows examples of flow visualization that were taken at a blade azimuth angle of approximately 30°. Each blade trails off a single helicoidal tip vortex which intersects the light sheet at an interval of $360^\circ/N_b$ (recall that these were 1-bladed rotors). Therefore, in the present case, the rotor that was employed produced a vortex filament that intersected the light sheet at wake ages of 30°, 390° and 750°.

From an examination of the results in Fig. 3.2, it is evident that the rectangular, swept, and BERP-like tips produce qualitatively similar flow structures, i.e., a single tip vortex and a turbulent vortical wake sheet trailed from the inner part of the blade. The tip vortices can be distinguished by the presence of a dark seed "void," which forms because of the small but finite centrifugal and Coriolis accelerations acting on seed particles at the center of the vortex flow. Notice that because seeding distributions can vary between images, any apparent differences in the size of the seed voids do not necessarily reflect any variations in the strength and/or structure of the tip vortices. Although seed voids are apparent in the flow visualization, it is still possible to adequately seed these regions to make successful PIV measurements.

For the swept and rectangular blade tips, the flow visualization showed that the tip vortices formed in the downstream wake almost directly behind the tip after about 10° of blade rotation. However, the BERP-like blade produced an initial vortex that was somewhat more diffused and, therefore, did not fully roll up into a coherent vortex until

somewhat later wake ages. A vortical sheet (usually referred to as a wake sheet) was observed in the wake all of the blades, and was distinguished by a relatively thin, turbulent shear layer. This sheet is generated by the merging of the boundary layers from the upper and lower surface of the blade. While the rectangular, swept and BERP-like blades produced very similar wakes in the near field, the slotted tip blade produced a more diffused tip vortex with significantly more turbulence and eddies in the downstream wake; see Figs. 3.2 and 3.3.

As previously discussed in Chapter 1, apparent laminar flow observed in the region surrounding the vortex core (for the rectangular, swept and BERP-like blades (Figs. 3.2a, 3.2b and 3.2c) is one major reason for the persistence of the tip vortices to relatively older wake ages. The laminar vortex core region indicates that vorticity is being diffused only through the very slow mechanism of shear on the molecular level, rather than the greater levels of diffusion obtained by the action of turbulence. In the present experiments, the tip vortices were found to persist to wake ages that were four to five revolutions old, which was sufficient to allow strong interactions of the developing flow with the boundary layer on the ground plane.

The PIV results in Fig. 3.3 showed that the peak values of velocity near the vortex cores reached about 30% of the blade tip speed, which was an expected result given prior tests with this and other rotors systems [90]. The inner wake sheet can also be seen in the PIV results that are shown in Fig. 3.3. The wake sheet actually consists of small pairs of counter-rotating vortices (i.e., so-called Taylor-Görtler vortex pairs), which show up as alternating direction velocity vectors directly inboard of the tip vortex [91]. The high frame rate capabilities of the laser and camera (1,500 fps equivalent to intervals of about

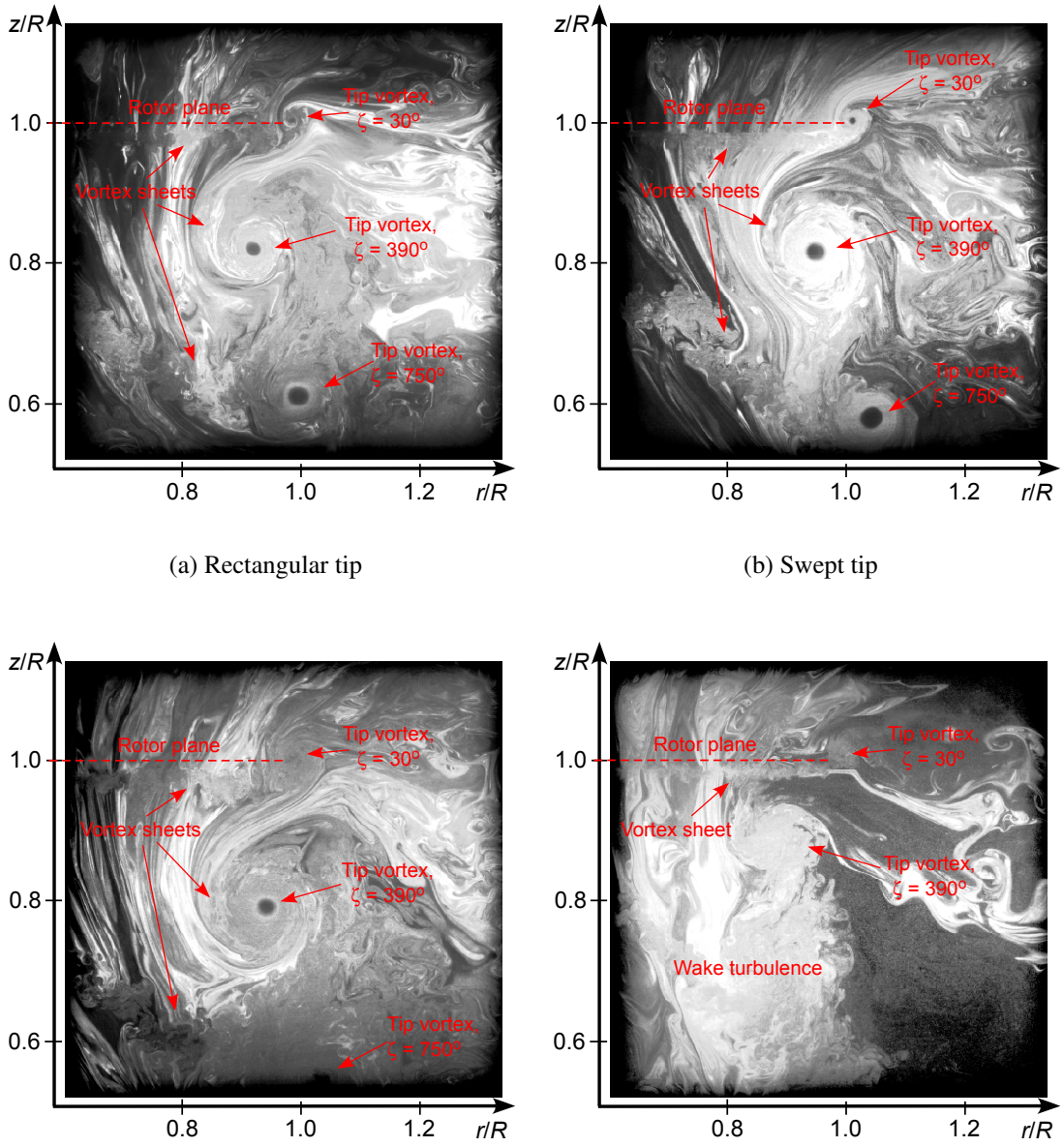

(a) Rectangular tip

(b) Swept tip

(c) BERP-like tip

(d) Slotted tip

Figure 3.2: Flow visualization of the rotor wake near the blade tip region for each of the four blades at a blade azimuth angle of 30°: (a) Rectangular tip; (b) Swept tip; (c) BERP-like tip; (d) Slotted tip.

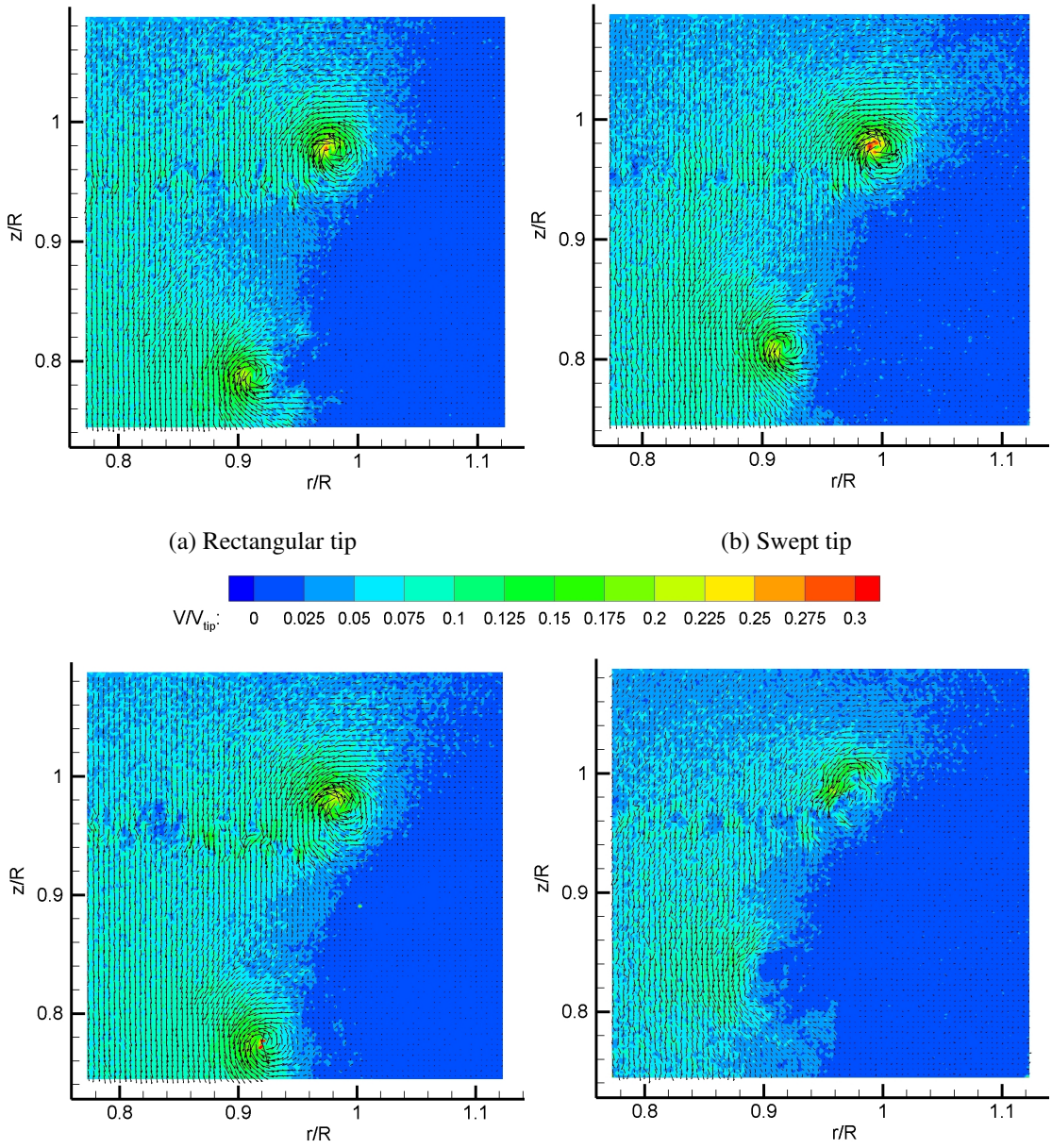

(a) Rectangular tip

(b) Swept tip

(c) BERP-like tip

(d) Slotted tip

Figure 3.3: PIV results of the rotor wake near the tip region of the four blades at a blade azimuth angle of 30°: (a) Rectangular tip; (b) Swept tip; (c) BERP-like tip; (d) Slotted tip. Flow vectors are plotted over contours of instantaneous total velocity.

7.5° in wake age) presented a unique opportunity to study the interactions between the vortical sheet and the newly formed tip vortex as they both convected in the rotor wake.

While the vortex sheet can be seen to interact with the newly formed tip vortex, ultimately the sheet convects axially downstream of the rotor at a faster rate than the tip vortex causing the sheet to catch up and interact with a tip vortex that is a full rotor revolution older, i.e., at $\zeta \geq 360°$. As the vortical sheet interacted with the vortices produced by the rectangular, swept and BERP-like tips, the high rotational accelerations in the core region acted to relaminarize the turbulent eddies in the vortical sheet, as shown in Fig. 3.2. Prior research has shown that the high streamline curvature of the flow found near tip vortices can suppress the creation of turbulence, and/or can even lead to rotational stratification of existing turbulence near the core [60, 61, 63], as also discussed in Chapter 1 of this thesis. In fact, the relaminarization process in vortex flows has been discussed by Cotel and Breidenthal [60], Cotel [61] and Ramasamy & Leishman [62] in terms of the rotational stratification effect that can be quantified using the Richardson number, which is a measure of the ratio of turbulence produced or consumed inside the vortex to the turbulence produced by shear. In this context, the Richardson number is given by

$$Ri = \frac{\dfrac{2V_\theta}{r^2}\dfrac{\partial\left(V_\theta r\right)}{\partial r}}{\left(r\dfrac{\partial\left(V_\theta/r\right)}{\partial r}\right)^2} \tag{3.1}$$

where r is the distance from the vortex center and V_θ is the local swirl velocity in the flow. At higher vortex Reynolds numbers and early wake ages, the Richardson number in the vortex core is too high (i.e., the values are greater than a threshold value to allow turbulence production, this threshold value being approximately $Re_v^{1/4}$), so the core remains mostly laminar. For example, Fig. 3.4 shows the variation in the local Richardson number

across the vortex flow as produced by the rectangular and slotted-tip blades, with the rectangular blade also being representative of the flow produced by the swept and BERP-like tips. One one hand, it is clear that the vortices produced by the rectangular blade exceed the threshold necessary to maintain laminar flow with the core region, and perhaps high enough even to relaminarize entrained turbulence originating from the vortex sheet. This outcomes explains the persistence of the vortices in the flow to relatively old wake ages even at low vortex Reynolds numbers, particularly when then are stretched in the wake when the rotor is in ground effect operation. On the other hand, the vortices produced by the slotted-tip blade have significantly lower values of the local Richardson number, specifically in the region of the vortex core, as shown Fig. 3.4a. As is evident from the results in Fig. 3.4b, almost the entire core of the vortex trailed by the slotted blade had values of the Richardson number that were below the stratification threshold. The implication in this case is that the vortices trailed by the slotted blades have a flow structure that is not conducive their persistence in the rotor wake, even in the presence of stretching effects. The vortices produced by the rectangular blade, however, had a larger region of the core with Richardson numbers above the stratification threshold, as so tended to persist in the flow for several rotor revolutions, as was confirmed using the flow visualization in this case.

A more detailed flow visualization time-history sequence is shown in Fig. 3.5. The portion of the tip vortex shown in this case was trailed from the rectangular blade and is about 163° of wake age. The process of stretching and elongation of the turbulent eddies is the one of the main reasons the core of the tip vortex remains small and tight to relatively old wake ages.

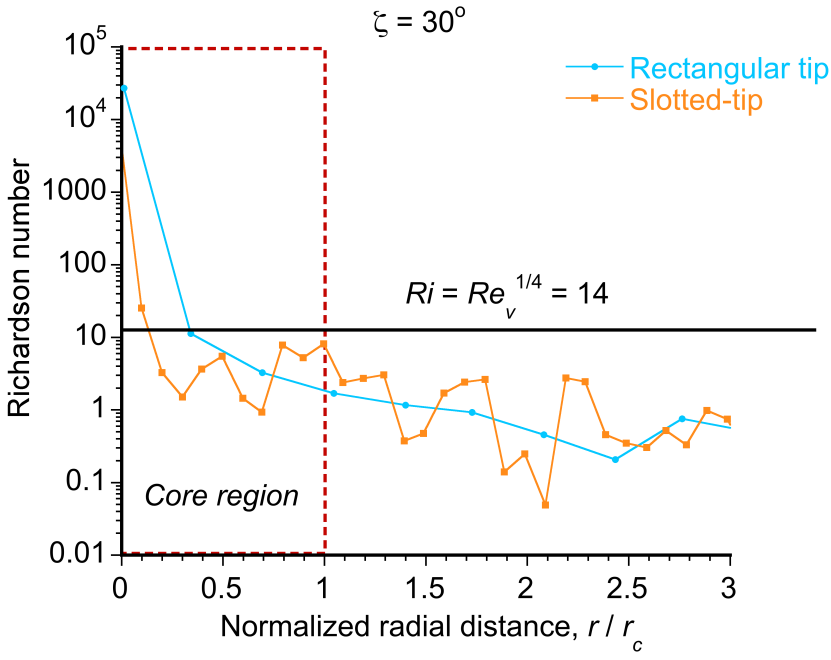

(a) $\zeta = 30°$

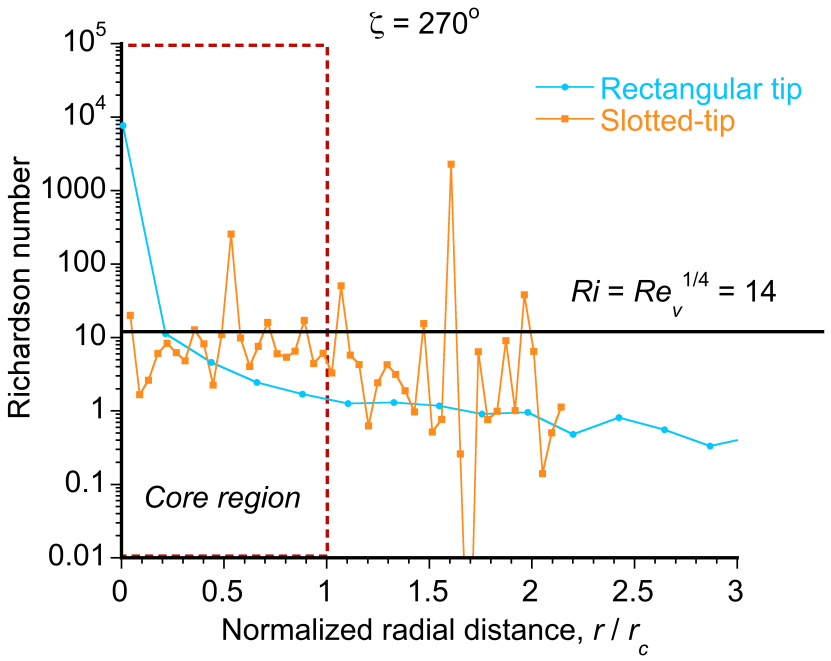

(b) $\zeta = 270°$

Figure 3.4: Variations in local Richardson number with radial coordinates located at the vortex center

Figures 3.2d and 3.3d show that the vortices trailed from the slotted tip blade were significantly more diffused at earlier wake ages, in part because there is a clear lack of a seed void. The increased diffusion produced by the slotted tip occurs because the slots in the blade tip eject turbulence and vorticity directly into what would otherwise be a laminar vortex core, thereby diffusing the concentrated vorticity in the inner core region [72–74] and producing lower swirl velocities. It should be appreciated that the lack of a distinct seed void with the slotted tip indicates much lower swirl velocities rather than deficiencies in seeding. Therefore, as the vortical sheet is entrained into the vortex core, the additional turbulence and vorticity contained in the sheet acts to sustain and enhance the radial diffusion of previously concentrated vorticity away from the vortex core.

The unique planform of the BERP-like blade was seen to produce some differences in the wake structure compared to the other blade tips. The BERP-like blade has a rapid increase in chord (outboard of about $0.87R$) from $1c$ to $1.24c$; see Fig. 2.4. However, the thrust weighted solidity, $\sigma_e = 3\int_0^1 \sigma r^2 \, \mathrm{d}r$, for the BERP-like blade is nominally the same as the other blades because of the decrease in the chord outboard of $0.95\%R$. Under certain conditions, especially high angles of attack a "notch vortex" is also known to form further inboard on this blade [92]. In the current experiments, however no substantial notch vortex could be distinguished, most likely because the blade pitch was too low. Nevertheless, the flow visualization and PIV made in the downstream wake for the BERP-like tip showed higher levels of vorticity and turbulence in the inboard wake sheet. The PIV results in Figs. 3.6, 3.7 and 3.8 also showed that the BERP-like tip produced a vortex with lower values of velocity near the core, suggesting that this blade planform certainly affects the roll-up and structure of the tip vortex.

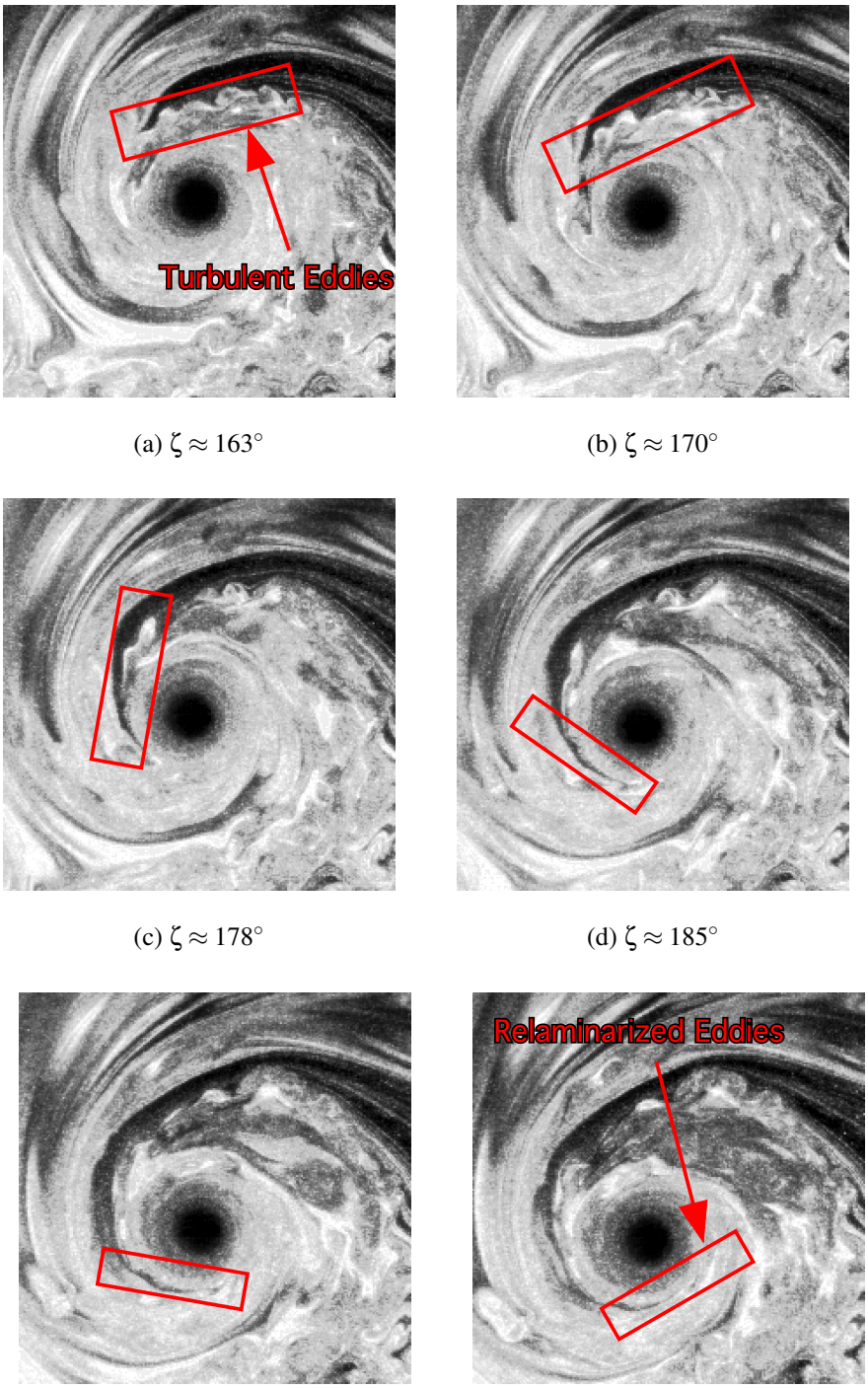

(a) $\zeta \approx 163^\circ$ (b) $\zeta \approx 170^\circ$

(c) $\zeta \approx 178^\circ$ (d) $\zeta \approx 185^\circ$

(e) $\zeta \approx 193^\circ$ (f) $\zeta \approx 200^\circ$

Figure 3.5: Flow visualization time-history of a tip vortex trailed by the rectangular blade for wake ages of about 163° to 200° showing the relaminarization of turbulent eddies that had their origin in the vortical sheet.

Figure 3.6 shows more detailed PIV measurements (with full vector resolution) of the tip vortices at early wake ages ($\zeta \approx 30^{\circ}$). The spatial resolutions achieved in the current experiments a provided a good number of measurement points to be obtained across the vortex core (this being typically between 8 to 16 points), which is a region of the flow that contains the steepest velocity gradients. The contours plotted are the instantaneous axial velocities (i.e., the v velocity). Notice that the rectangular blade tip (see Fig. 3.6a) and the swept blade tip (see Fig. 3.6b) produced essentially the same velocity fields. The BERP-like blade, however, produced a more diffused core region with weaker velocity gradients, and the slotted-tip in particular produced a much more diffused vortex with relatively shallow velocity gradients.

To fully understand the differences seen in the flow near the ground plane, it is necessary to further assess the flow in the near field of the rotor (primarily the characteristics of the tip vortices). The velocities induced by the vortices were examined using both instantaneous and phase-averaged velocity measurements. The flow field below the rotor will always contain some amount of aperiodicity that causes the spatial location of the vortex centers to change in successive PIV realizations of the flow. This effect must be accounted for prior to phase averaging, or it will act to effectively smear the velocity gradients in the tip vortex, yielding artificially lower swirl velocities and larger core sizes.

To correct for this aperiodicity in the flow, the measured vortex centers were aligned and set as the origin for each image [93, 94]. This correction procedure ensures that the velocities at a point in the flow are calculated based on their spatial location with respect to a defined location in the flow (i.e., the tip vortex center) rather than with respect to the image boundaries. The two-dimensional Q-criterion method was chosen to identify the

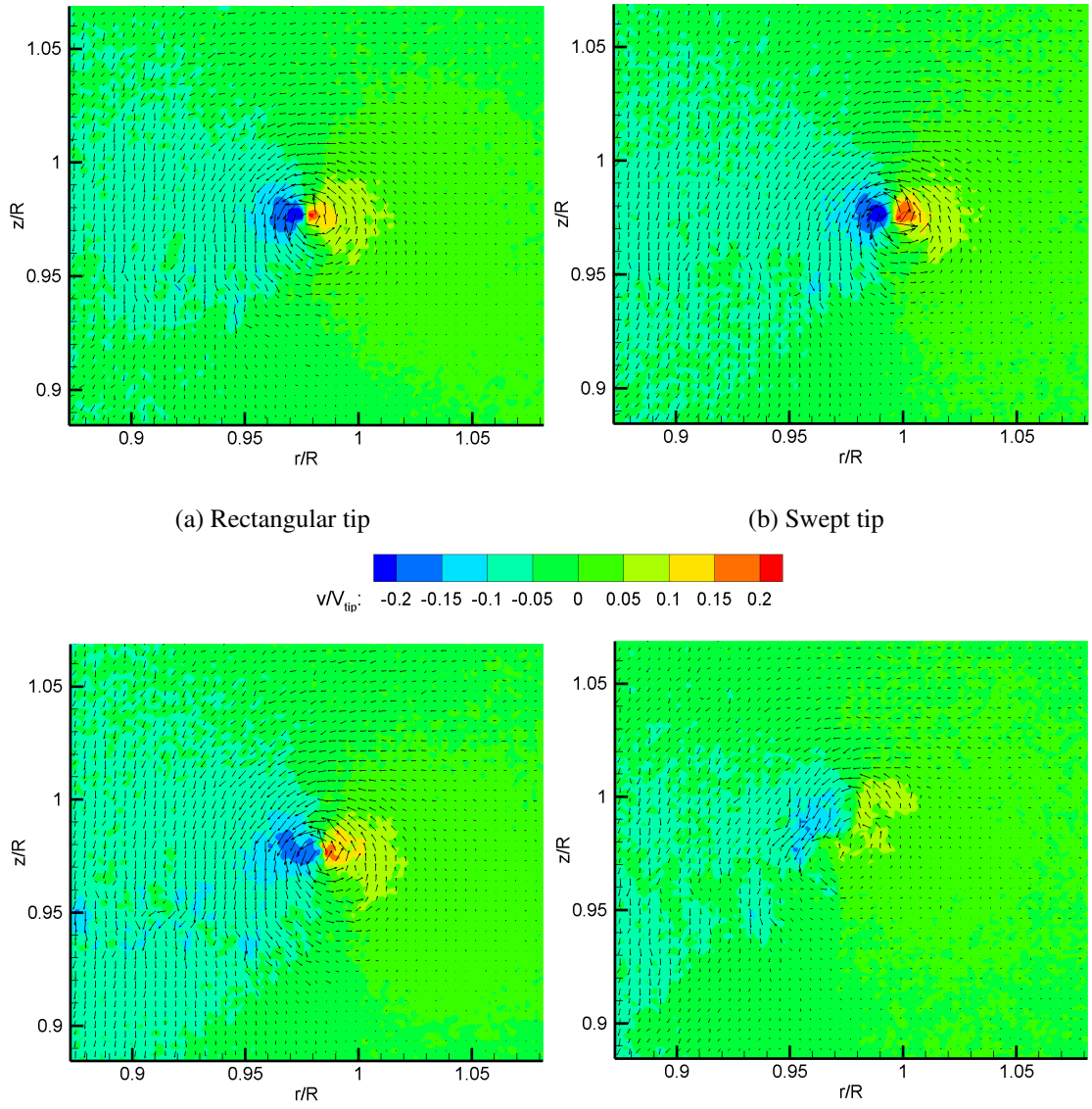

(a) Rectangular tip

(b) Swept tip

(c) BERP-like tip

(d) Slotted tip

Figure 3.6: Detailed PIV measurements of the tip vortex flow (background contour in terms of the instantaneous vertical component of velocity) for each of the four blades at a wake age of 30°: (a) Rectangular tip; (b) Swept tip; (c) BERP-like tip; (d) Slotted tip.

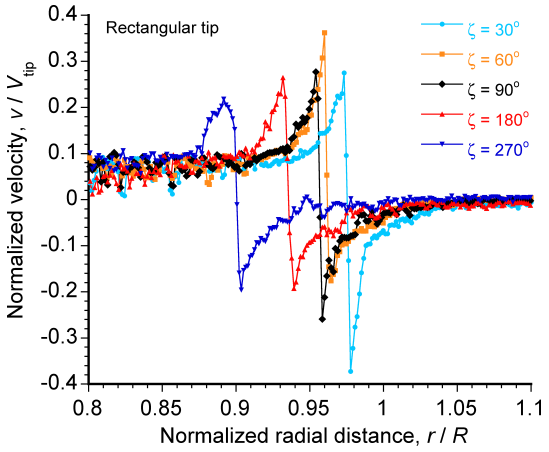

(a) Rectangular tip

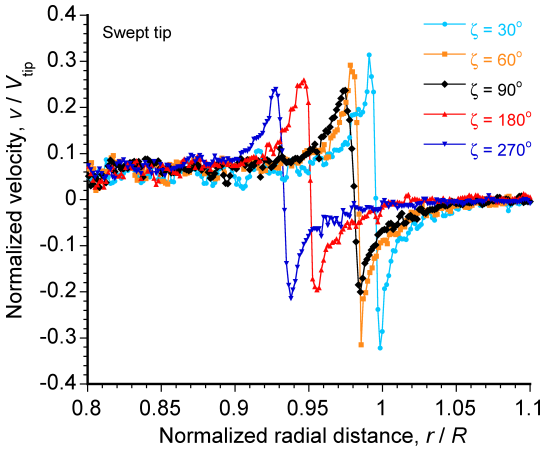

(b) Swept tip

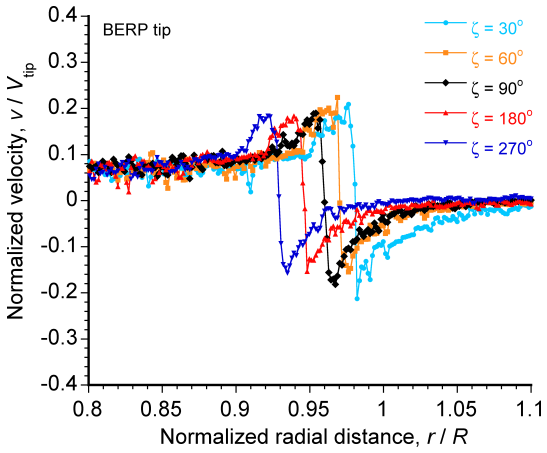

(c) BERP-like tip

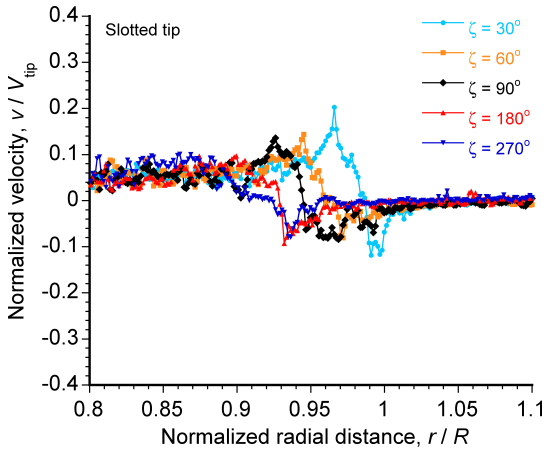

(d) Slotted tip

Figure 3.7: Instantaneous velocity signatures of the tip vortex at early wake ages for each of the four blades in a cutting axis parallel to the rotor plane: (a) Rectangular tip; (b) Swept tip; (c) BERP-like tip; (d) Slotted tip.

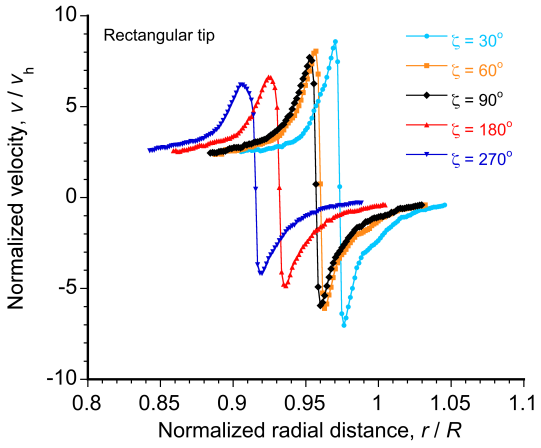

(a) Rectangular tip

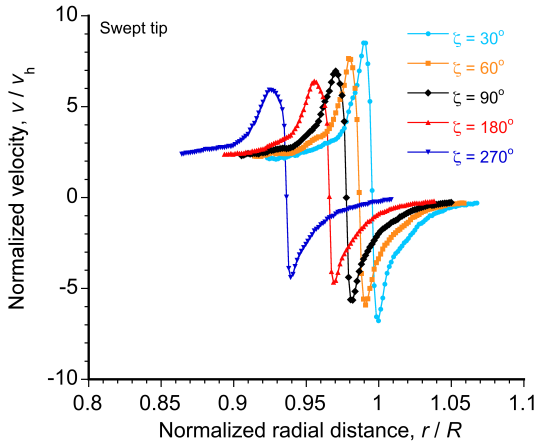

(b) Swept tip

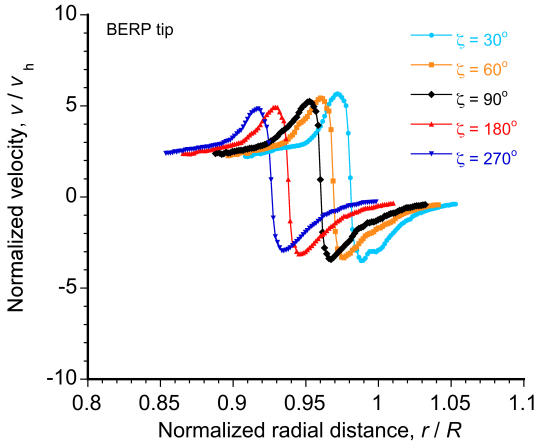

(c) BERP-like tip

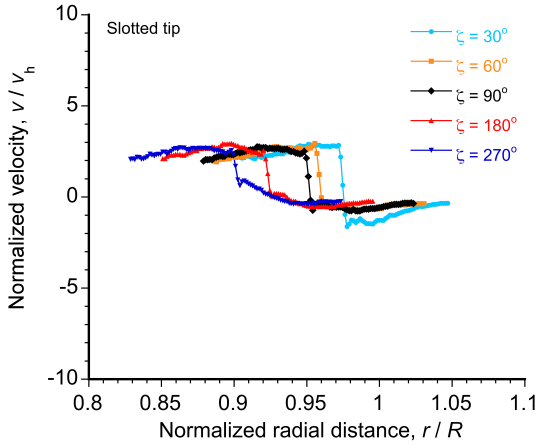

(d) Slotted tip

Figure 3.8: Phase-averaged velocity signatures of the tip vortex at early wake ages for each of the four blades in a cutting axis parallel to the rotor plane: (a) Rectangular tip; (b) Swept tip; (c) BERP-like tip; (d) Slotted tip.

vortex center because it accurately predicted the vortex center, while requiring a minimum number of images to converge to a fixed location [93]. The Q-criterion method is discussed further in Appendix A.

Figures 3.7, and 3.8 show the instantaneous and phase-averaged velocity profiles in a cutting axis parallel to the rotor plane. The phase-averaged results have been corrected for aperiodicity using the collocation technique based on the Q-criterion. The corrected average used 100 separate PIV image pairs, whereas the instantaneous measurements corresponded to a single PIV image pair. The instantaneous image selected for each blade showed the largest local excursions in velocities. The measurements are plotted in terms of their radial distance (r) normalized by the rotor radius (R) from the axis of rotation.

In the fixed reference frame, the vortices appear as asymmetric velocity profiles in the horizontal cutting planes that intersect the axis. Because the cutting planes pass within one PIV interrogation point of the vortex axis, the velocity components can be considered equivalent to the swirl velocities. The rectangular, swept, and BERP-like tips (see Figs. 3.7a, 3.7b and 3.7c) all showed that the peak swirl velocities diminished as the tip vortices aged in the flow, which is a result of the radial diffusion of vorticity away from the vortex core. As the vortices aged, they also convected radially inward from the blade tip region, with the wake contraction reaching about $0.9R$ at a wake age of 270°. The induced velocity fields produced by the rectangular and swept blade tips were found to have essentially the same magnitude, however, there were some differences in the spatial positions of the respective tip vortices in the downstream wake.

Comparing the tip vortex produced by the BERP-like tip to that of the baseline rectangular and the swept tips, it was apparent that the BERP-like tip produced vortices

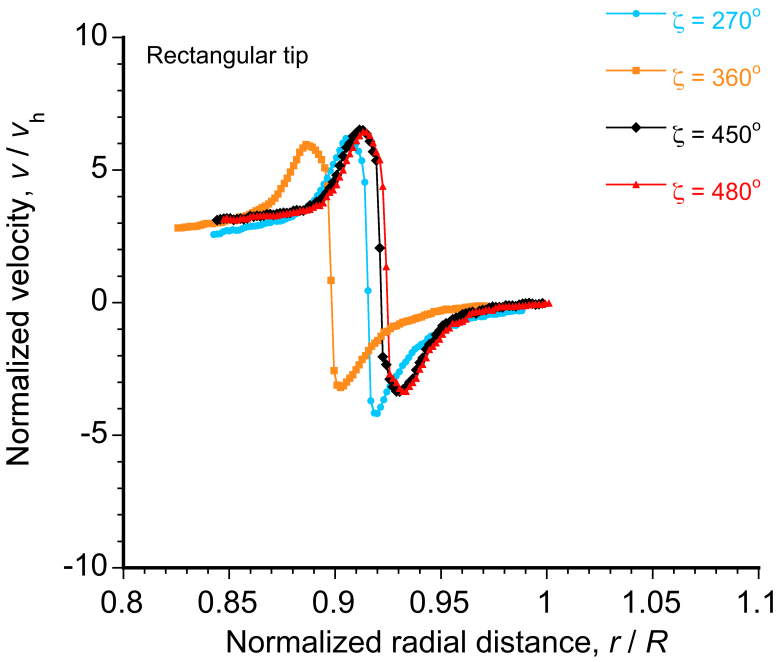

(a) Rectangular tip, $\zeta = 360^\circ - 480^\circ$

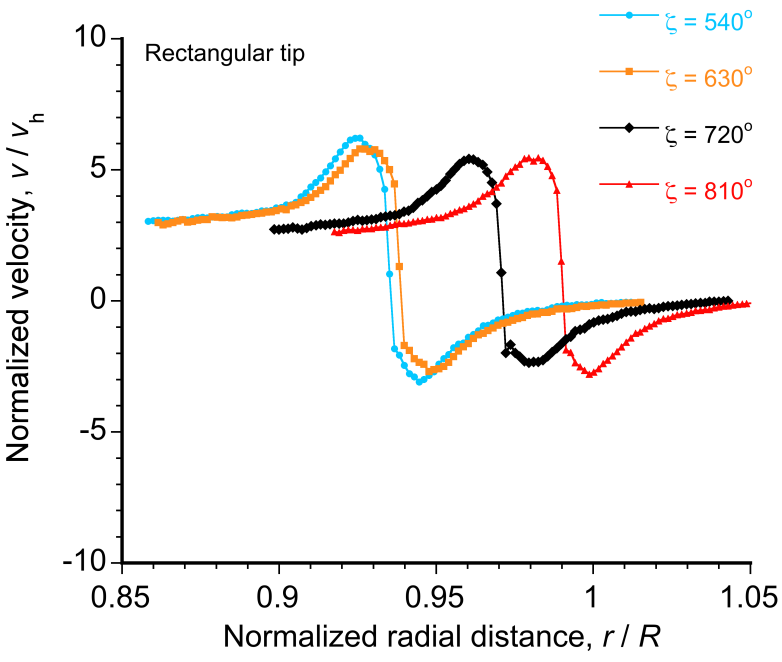

(b) Rectangular tip, $\zeta = 540^\circ - 810^\circ$

Figure 3.9: Phase-averaged velocity signatures of the tip vortex from the rectangular blade at older wake ages in a cutting axis parallel to the rotor plane.

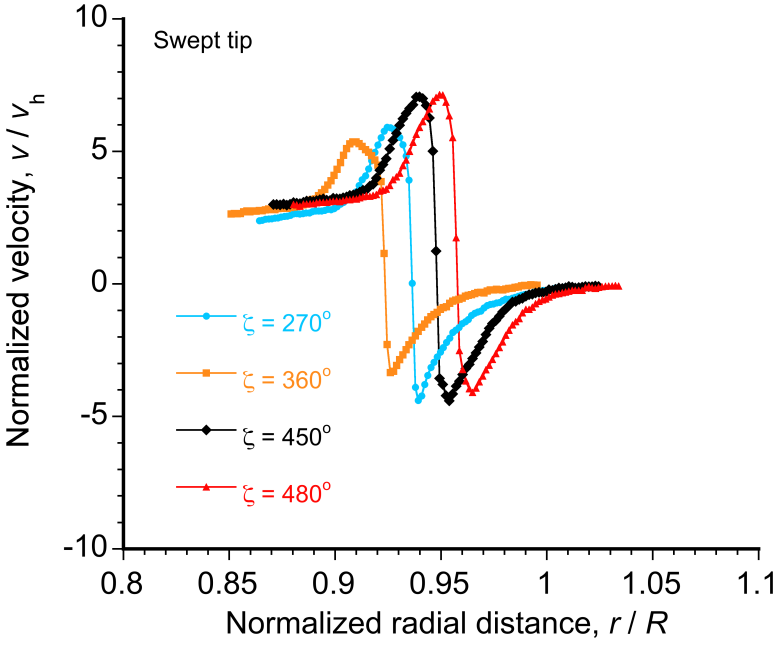

(a) Swept tip, $\zeta = 360^\circ - 480^\circ$

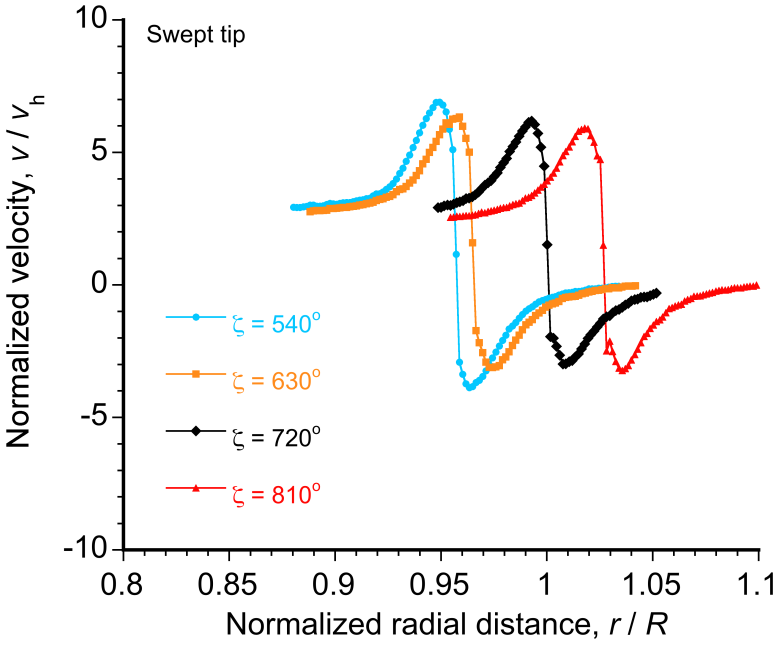

(b) Swept tip, $\zeta = 540^\circ - 810^\circ$

Figure 3.10: Phase-averaged velocity signatures of the tip vortex from the swept blade at older wake ages in a cutting axis parallel to the rotor plane.

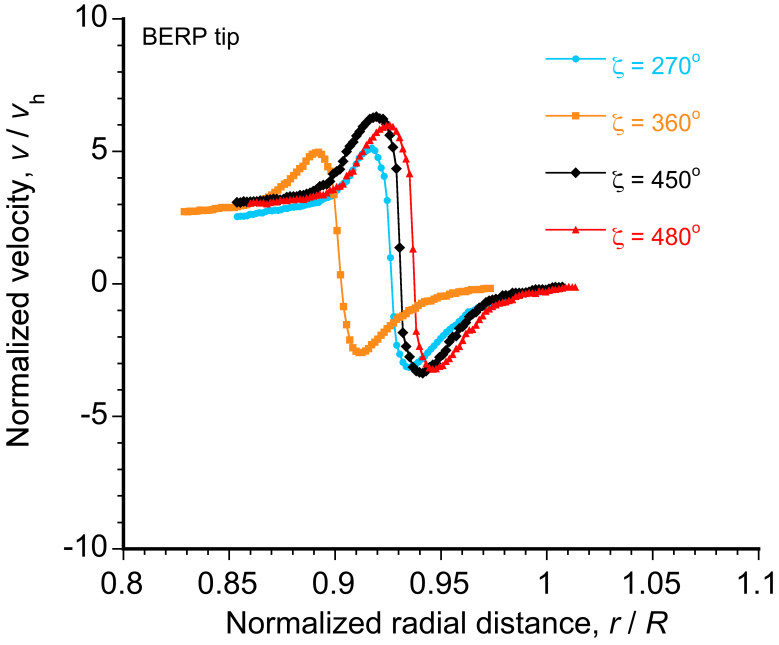

(a) BERP-like tip, $\zeta = 360° - 480°$

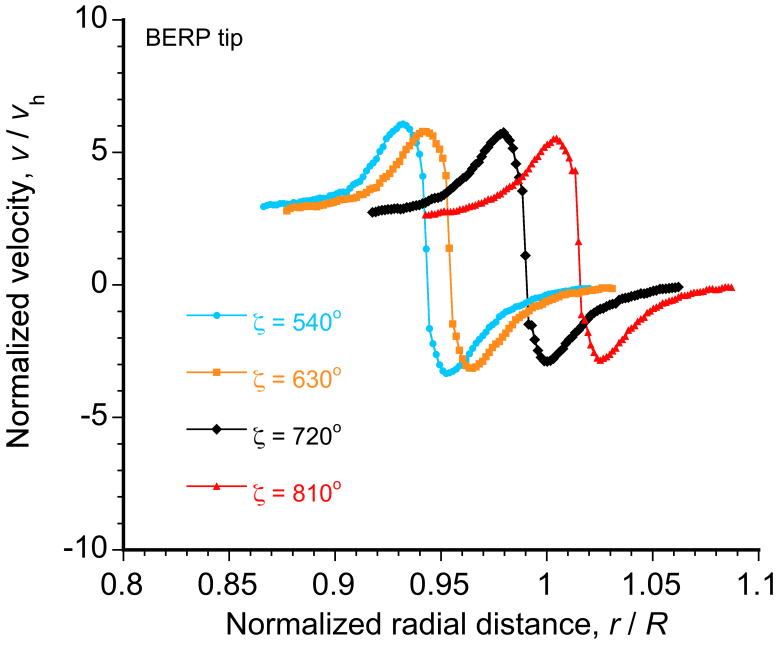

(b) BERP-like tip, $\zeta = 540° - 810°$

Figure 3.11: Phase-averaged velocity signatures of the tip vortex from the BERP-like blade at older wake ages in a cutting axis parallel to the rotor plane.

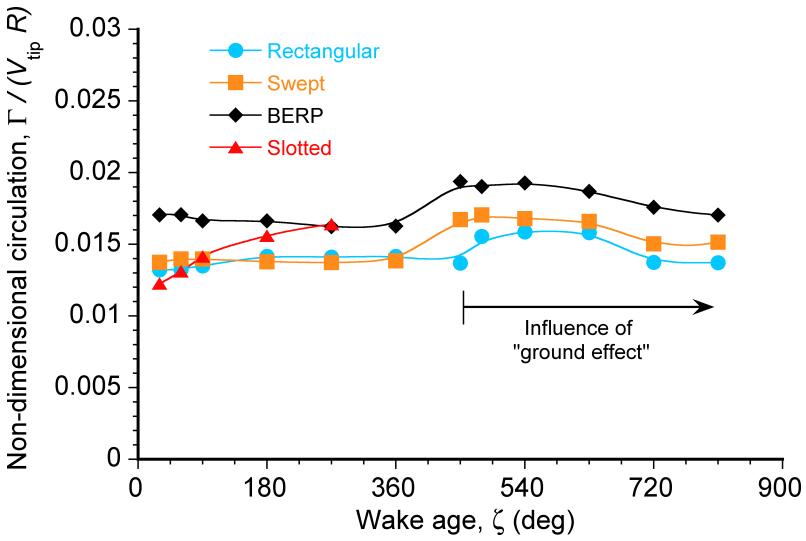

Figure 3.12: Time-history of the tip vortex circulation as a function of wake age for the rectangular, swept, and BERP-like blades.

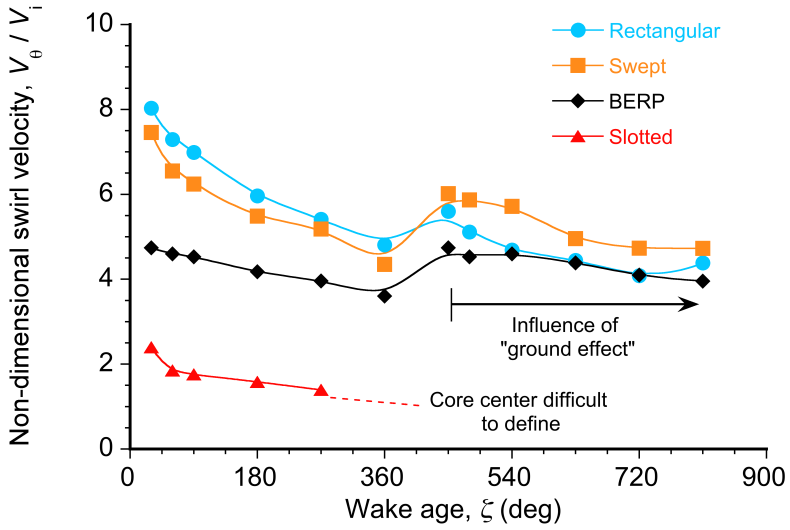

Figure 3.13: Time-history of the tip vortex peak swirl velocity as a function of wake age for the rectangular, swept, and BERP-like blades.

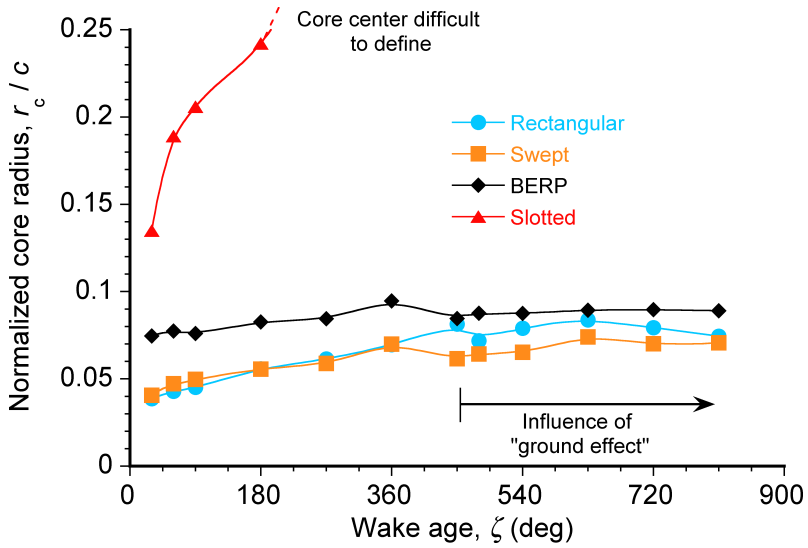

Figure 3.14: Time-history of the tip vortex core radius as a function of wake age for the rectangular, swept, and BERP-like blades.

with somewhat lower peak swirl velocities and larger core sizes. (Note that the vortex core radius was assumed to be equal to half the distance between the peaks in the velocity profiles.) In the current experiments, the core radii at early wake ages were found (in general) to be 0.5–2% of the rotor radius or 5–20% of the blade chord. The differences seen with the BERP-like blade are, most likely, a result of the different roll-up process along the highly swept edge of the blade. However, in the present work the actual roll-up process was not studied in detail. Small differences in the strength and location of the vortical sheet as it is convected downstream of the blade may also play some role in the observed differences. Clearly, the slotted-tip blade produces much lower swirl velocities and also significantly larger core sizes [72–74].

Because the results shown in Fig. 3.7 are instantaneous flow measurements, the velocity fluctuations resulting from turbulence are pronounced. Outside the wake boundary

the flow is essentially quiescent, with relatively low fluctuations from turbulence and a nearly zero flow velocity. However, inside the wake boundary the turbulent fluctuations are more significant (between 2% and 5% of the tip speed) and the velocity is non-zero. The results for the slotted-tip showed higher levels of turbulence in the tip vortex and the rotor wake; see Fig. 3.7d. In general, the higher levels of turbulence seen in the PIV measurements correlated well with the observations made in the flow visualization; see Fig. 3.2d.

To better understand the development of the rotor wake (namely the tip vortices) in the region between the near field and the ground, further measurements were performed to examine the vortex characteristics at wake ages between one and three rotor revolutions old. To this end, Figs. 3.9, 3.10 and 3.11 show the phase-averaged swirl velocity profiles the rectangular, swept, and BERP-like tips for wake ages between 360° and 1080°. Again, the Q-criterion (discussed in Appendix A) was applied to determine the vortex centers, about which the respective images were collocated before they were phase-averaged. Phase-averaged velocity profiles could not be obtained in the case of the slotted tip because the vortices at these wake ages were just too diffused to consistently identify the center of the vortex flow.

In ROI 2 and 3 the rotor wake begins to interact with the ground. Because a solid surfaces must be a streamline of the flow, the wake begins to turn until the flow is converted from a primarily axial (downward) flow to a primarily radial (outward) flow. As the wake begins to turn, the tip vortex filaments begin to stretch, causing the normal diffusive trend of the vortices to be reduced or reversed, with the swirl velocities increasing and the core sizes decreasing [62]; see Fig. 3.15. Stretching can maintain or intensify the

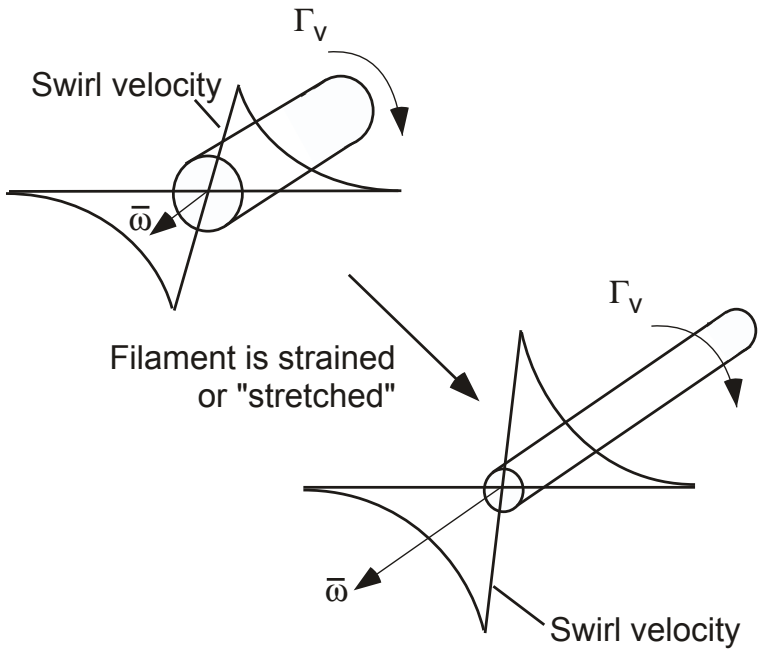

Figure 3.15: Schematic of vortex filament stretching.

vorticity, and occurs because of volume conservation in the fluid elements. As the vortex filament lengthens, conservation of mass requires the core diameter to decrease, which reduces the radial length over which the associated vorticity is distributed [33].

The trends shown for the three blades were found to be very similar. As the vortices approached the ground plane (ROI 4) the swirl velocities and the core size attained a nominally constant value (essentially an equilibrium point where the effects of diffusion and stretching are in balance), which was also confirmed through examination of the peak-to-peak values of the induced velocity profiles, as shown in Figs. 3.9b, 3.10b and 3.11b.

The vortex characteristics (i.e., swirl velocity, core size, and circulation) were further analyzed using a least squares fit of the model determined by Vatistas et al. [95] to

the measured swirl velocity profiles [89]. This model defines the tangential velocity,V_θ, in the vortex flow as

$$V_\theta(\bar{r}) = \left(\frac{\Gamma_v}{2\pi r_c}\right) \frac{\bar{r}}{(1+\bar{r}^{2n})^{\frac{1}{n}}} \tag{3.2}$$

where Γ_v is the circulation contained in the vortex, r_c is the radius of the vortex core, $\bar{r}$ is the distance from the vortex core non-dimensionalized by the vortex core radius, and n is an integer value. To insure the best fit with the measured velocity profiles two values of n were examined, namely $n = 1$ and $n = 2$. Ultimately, the $n = 1$ model was selected over the $n = 2$ model because for the present measurements it better predicted the shallower peaks in the velocity gradients near the vortex core.

From the velocity fields surrounding the tip vortices, their circulation Γ_v, (i.e., their strengths) can be evaluated. This result was obtained by calculating the line integral $\oint \vec{V} \cdot d\vec{s}$ around a path enclosing the vorticity field, where $\vec{V}$ is the velocity field obtained using PIV and $d\vec{s}$ is the directed line segment; see Fig. 3.16a. A rectangular path was assumed for convenience because it coincides with the PIV grid points.

Representative results are shown in Fig. 3.16b are at a wake age of 180°, and show the circulation around the tip vortex as a function of the size of the contour of integration. The values asymptote as the enclosed area increases to a sufficient size to include all of the vorticity associated with the vortex flow, such results being typical for all wake ages. In the case of the rectangular, swept, and BERP-like tips the vortex strengths were found to be nominally similar, the BERP-like blade producing a slightly higher strength because it was operated at a somewhat higher thrust (see table 3.1). Circulation values obtained from the line integral method were used to validate the results acquired from the least

squares fit. The results obtained from the least squares fit was found to correlate well with the values obtained from the line integral method. Based on the measured values of circulation, the vortex Reynolds number of the tip vortices, Re_v, was approximately 35,000.

The characteristics of the tip vortices trailed by the rectangular, swept, BERP-like, and slotted-tip blades are summarized in Figs. 3.12, 3.13 and 3.14 in terms of their circulation strengths, peak swirl velocities and core size, as a function of wake age. The results in Fig. 3.12 showed that the circulation began to approach a constant value for an integration contour box larger than $0.04R$ ($0.36c$). These differences can be tied at least in part to the dynamic interaction of the tip vortices with their inboard wake sheet, which contained different amounts and distributions of circulation as well as turbulence, and also to differences in the operating thrust of the rotor.

The circulation contained in the wake sheets also interacted with the tip vortices at varying wake ages. As the vortices began to interact with the ground the values of their circulation changed slightly, but ultimately they remained nominally constant as they were entrained into the developing flow at the wall. Because of the highly diffused tip vortex produced by the slotted-tip blade, the circulation contained in the flow in this case was difficult to define at wake ages older than about 270°.

Figure 3.13 shows the peak swirl velocity, which is very sensitive to small changes in the structure of the vortex filament. At early wake ages the swirl velocities produced by the rectangular and swept tip blades were nominally the same. However, variations in the peak velocities began to manifest as the vortices interacted with the ground. The vortices produced by the BERP-like tip were noted to be more affected by the stretching

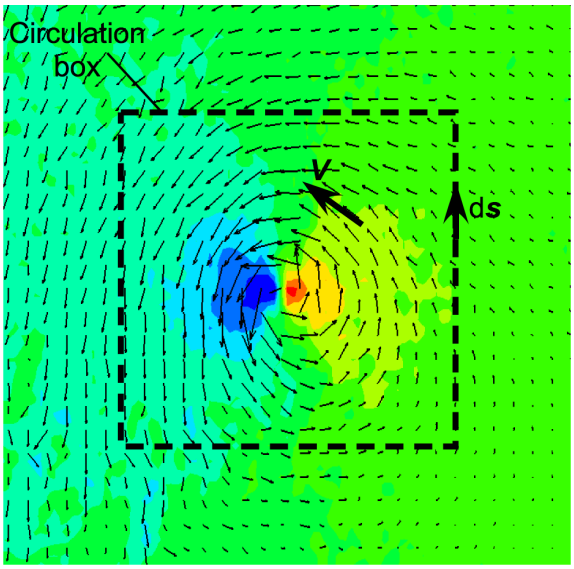

(a) Grid used for circulation measurement

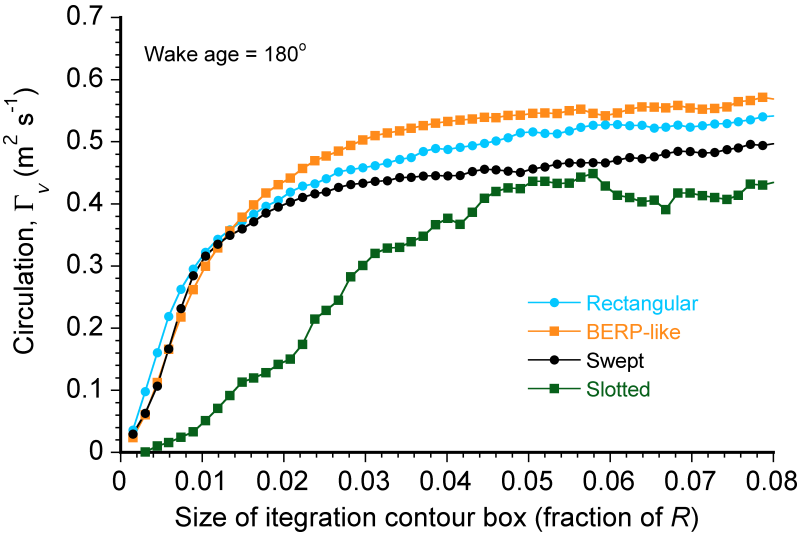

(b) Circulation

Figure 3.16: Tip vortex circulations for each of the four blade tips at a wake age of 180°.

effects that occurred under the influence of the ground.

The effect of filament stretching on the vortices produced by the BERP-like tip can be seen by comparing the swirl velocities at early wake ages to the swirl velocities at later wake ages. At early wake ages the swirl velocities were seen to be significantly lower than the rectangular and the swept tips (on the order of 40%) even though the BERP-like rotor was actually operating at a slightly higher thrust in these experiments. However, as the vortex begins to interact with the ground the swirl velocities are reintensified significantly to values that are much higher than the rectangular tip. Conversely, the slotted-tip produced swirl velocities that were significantly lower than for the other three blades.

The variation of vortex core radius as a function of wake age is shown in Fig. 3.14 for each of the four blades. It is clear, that the slotted-tip blade produced a vortex with significantly larger values of core radius and that the vortex continued to rapidly diffuse as it convected in the rotor wake. The BERP-like blade showed a larger core radius than the rectangular and swept tip blades. Initially the rectangular, swept and BERP-like blades produced vortices that grew logarithmically with wake age, however, as the vortices began to interact with the ground the vortex filament was stretched, causing the growth of the core size to be reversed. As found with the circulation and swirl velocities, the core radius of the tip vortices changed very little as they approached the ground, which is mainly a result of diffusion and reintensification being in equilibrium here, as previously discussed.

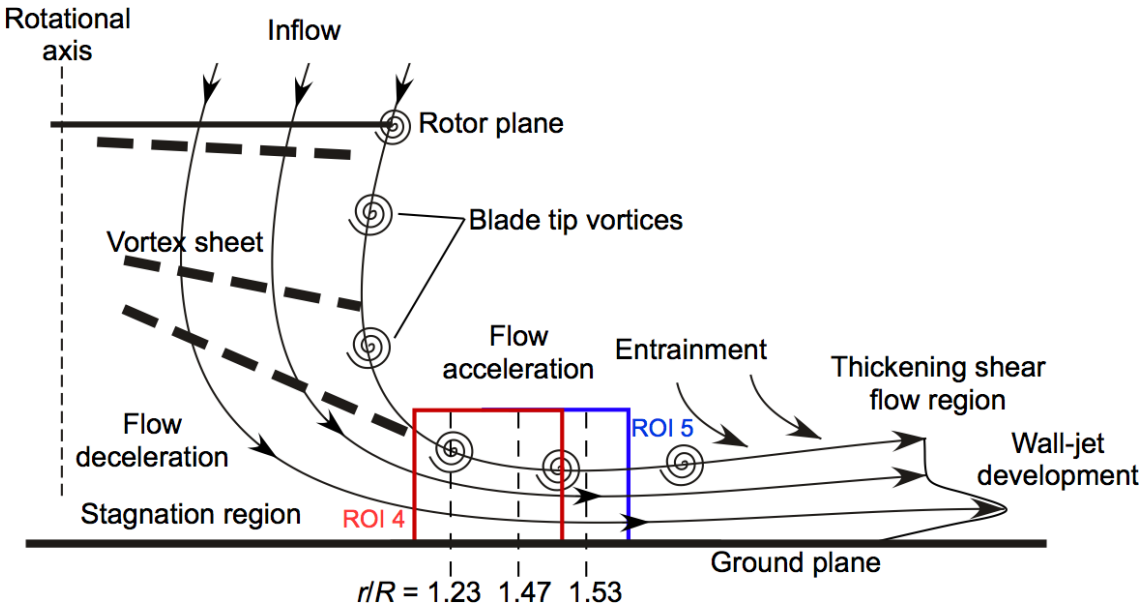

Figure 3.17: Schematic of the flow as it develops on the ground and showing the regions of interest in measurement positions used to determine the wall parallel velocity profiles.

3.4 Flow at the Ground Plane

Figure 3.17 shows a schematic of the general flow field that was observed as the rotor wake convected toward the ground plane. As shown previously in Fig. 3.15, the interaction of the rotor wake and the ground causes the wake to turn rapidly, also stretching and intensifying the vorticity of the vortex filaments. As the flow convects radially along the ground plane it begins to develop into a turbulent wall-jet type of flow. Viewing the wall jet as a boundary layer region that is supplied with momentum from the rotor, the maximum velocities in the wall-jet locally exceeded the average velocities in the upstream flow; see also [96, 97]. However, in this case the wall-jet flow contains significant amounts of vorticity.

Figure 3.17 shows the ROIs where flow visualization and PIV were performed, as

well as the positions where detailed velocity profiles were obtained. Figure 3.18 shows the flow visualization results for the regions near the ground plane (i.e., ROI 4 and 5). From the flow visualization, it was observed that the convecting tip vortices persist and interact with the developing flow at the ground, the exception being the slotted-tip blade.

It has been shown previously in this chapter that as the blade tip vortices initially convect below the rotor they have the tendency to diffuse and spin down under the action of viscosity and turbulence. However, as the wake expands along the ground plane (entering the imaging zone shown in Fig. 3.18) the core vorticity reintensifies and the tip vortices were observed to persist in this case for 5 to 7 revolutions. The reintensification of vorticity allowed the tip vortices to remain coherent long enough to penetrate the boundary layer and strongly influence the developing flow on the ground plane. Recall from Chapter 1 that more recent experiments with rotors hovering over loose sediment beds [8, 9] indicate that sediment is uplifted by the velocities induced by the convecting tip vortices near the ground, and is a fundamental mechanism affecting brownout.

Flow visualization results obtained for the rectangular blade tip is shown in Fig. 3.19 in the form of a time-history. As the tip vortices approach the ground, adjacent helicoidal vortex filaments can be seen to pair (e.g., the pair marked as blue and green in Fig. 3.19), which is a fundamental characteristic of rotor wakes as they interact with ground planes [8, 9]. As the downstream vortex moves up (out of the developing radial flow) its rate of convection slows significantly, allowing the upstream vortex to convect close enough to it to cause the two vortices to pair and roll up around each other. This behavior tends to force the younger vortex closer to the ground plane, inducing large velocity gradients on the surface.

Qualitatively at least, the behavior of the wake near the ground appeared to be generally similar for the rectangular, swept and BERP-like blade tips. the exception was, the flow field produced by the slotted-tip, which contained significantly less concentrated vorticity. Although, the flow field produced by the slotted tip had less concentrated vorticity, there were substantial levels of turbulence seen in this case. Compared to the upstream flow, higher levels of turbulence were observed for all blade tips at the ground. As a consequence, the aperiodicity in the flow at the ground was also significantly increased. The increased turbulence was a result of the entrainment of the converting vortical wake sheets into the developing wall jet and the more unstable nature of helicoidal filaments at older wake ages [67, 78, 79]. Because of the relatively large amounts of aperiodicity in the flow near the ground, the images used were selected at approximately the same spatial locations (i.e., they were spatially correlated in terms of the vortex positions).

The PIV results confirmed the qualitative conclusions that were made when using the flow visualization. Figures 3.21, 3.22, 3.23 and 3.24 show six mosaics of the PIV measurements at the ground in ROI 4 and 5 for each of the four blade tips. In this case the flow vectors are superimposed on a background contour of the total instantaneous velocity. It is important to notice the grid change near the wall which was used to increase the spatial resolution of the measurements in the boundary layer region near the ground (see Section 2.6.7. As with the flow in the near field of the rotor, the tip vortices continued to convect along the edge of the slipstream boundary. Unlike the flow in the near field of the rotor (ROI 1), where the BERP-like tip produced notably lower induced velocities, the magnitude of flow velocities at the ground were found to be essentially the same for each of the rectangular, swept, and BERP-like tips. However, the slotted-tip blade produced a

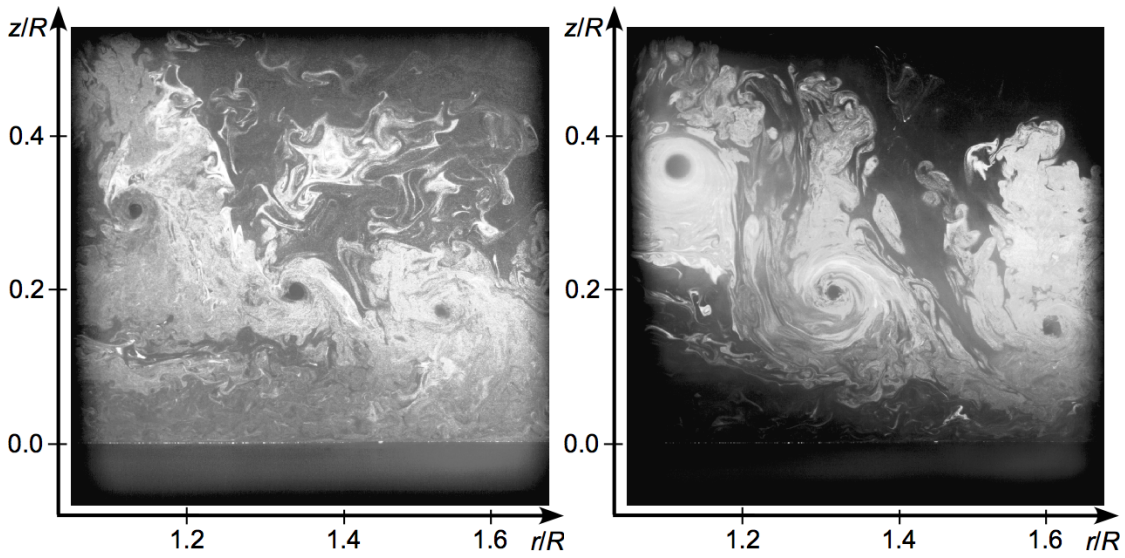

(a) Rectangular tip

(b) Swept tip

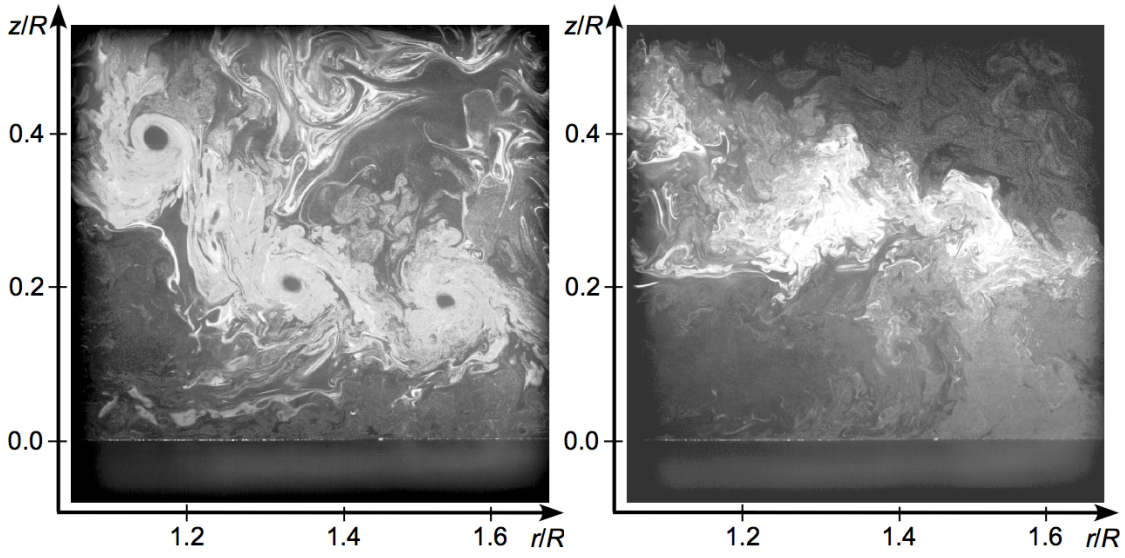

(c) BERP-like tip

(d) Slotted tip

Figure 3.18: Flow visualization images of the rotor wake for each of the four blades as it reaches the ground. In this case the youngest vortex (top left in the images) is about 1080° old. (a) Rectangular tip; (b) Swept tip; (c) BERP-like tip; (d) Slotted tip.

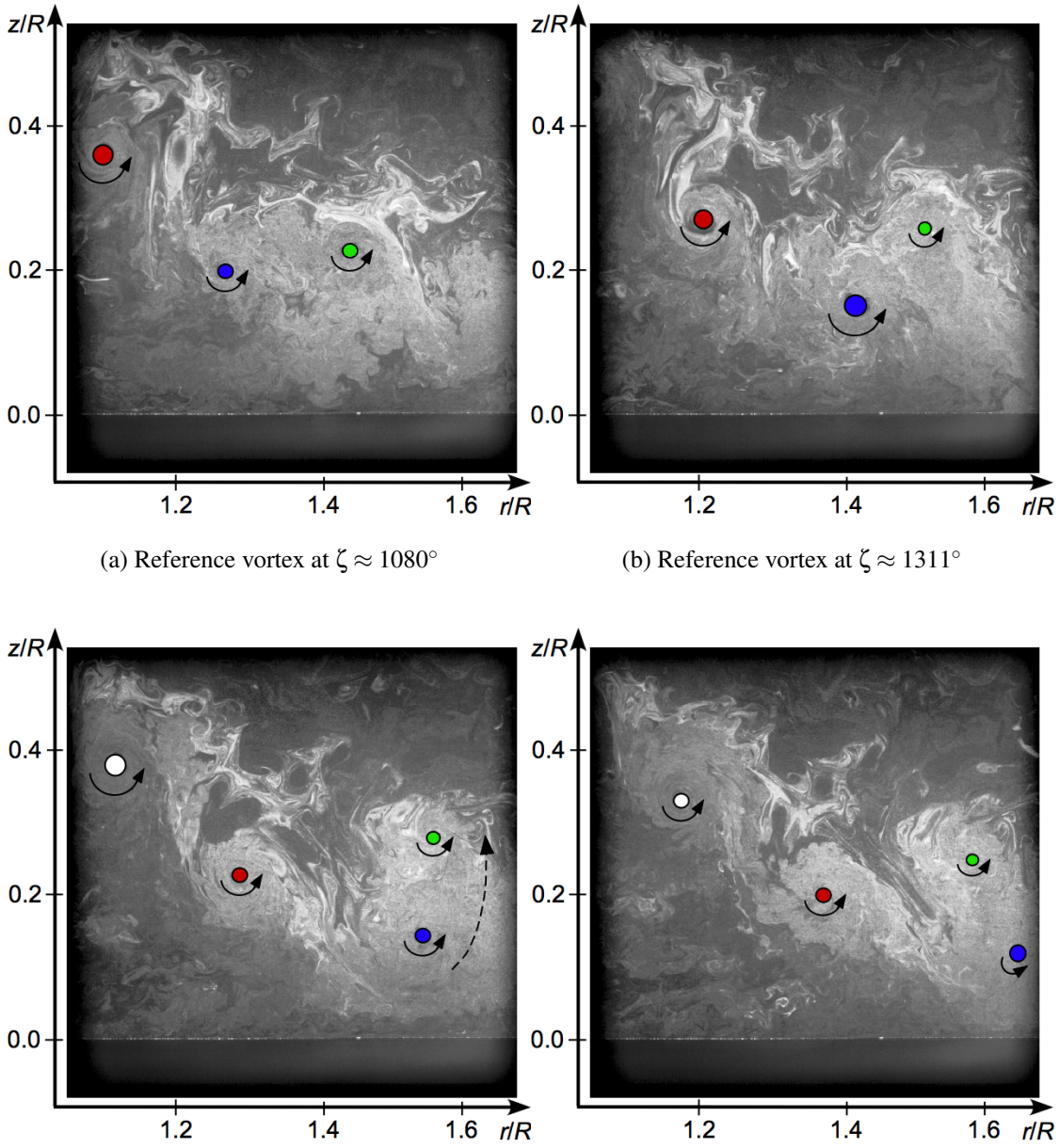

(a) Reference vortex at $\zeta \approx 1080°$

(b) Reference vortex at $\zeta \approx 1311°$

(c) Reference vortex at $\zeta \approx 1482°$

(d) Reference vortex at $\zeta \approx 1615°$

Figure 3.19: Flow visualization time-history at the ground for the blade with the rectangular tip showing pairing of adjacent turns of the vortex filament (reference vortex marked in red): (a) Reference vortex at $\zeta \approx 1,080°$; (b) Reference vortex at $\zeta \approx 1,311°$; (c) Reference vortex at $\zeta \approx 1,482°$; (d) Reference vortex at $\zeta \approx 1,615°$.

flow field that had significantly lower velocity excursions; see Fig. 3.24.

Figures 3.20a and 3.20b shows a comparison of a representative velocity profile at the ground plane that was generated by a rotor of smaller scale, as used by Sydney et al. [9] and Johnson et al. [8], with a corresponding velocity profile measured in the current experiments. Comparing the dimensional results shown in Fig. 3.20a, the flow fields obviously appear very different. However, by normalizing by the hover induced velocity v_h and rotor radius R, the results can be seen to collapse to generally the same velocity profile shape, boundary layer thickness, and overall magnitude of the velocities; see Fig. 3.20b. The similarities between the results obtained in this case lends confidence in the ability to perform rotor in ground effect measurements on a smaller rotor where the effects on sediment motion can also be studied simultaneously. (Note that the present rotor system is too large to permit 2-phase flow measurements.)

Figure 3.25 also shows instantaneous velocity field images for the rectangular, swept, BERP-like and slotted-tip blades. Localized regions of large upwash velocity have been shown to be an important mechanism in the development of a brownout cloud [8,9]. Dual-phase experiments performed Johnson et al. [8] and by Sydney et al. [9] showed that as sediment is entrained in the developing flow along the ground plane, it is convected radially outward away from the rotational axis of the rotor, and will tend to saltate and bombard the surface injecting additional sediment particles into the developing flow at the ground. As the tip vortices interact with the sediment entrained in the developing flow, the large regions of upwash will tend to lift these sediment particles to even higher heights. The "trapping" phenomenon, initially identified by Johnson et al. [8] describes this type of uplift mechanism in greater detail. Therefore in the present work, it was nec-

essary to examine in detail the upwash fields produced by the four blade tips near the ground.

A further analysis was performed to extract the average and instantaneous velocity profiles near the ground plane in the wall-parallel direction. In this case, the magnitude of the average flow along the ground was found to be closely correlated to the magnitude of the average downwash below the rotor. The operating thrust of the rotors produced an average inflow ratio $\lambda_h = (v_h/\Omega R)$ of approximately 0.035, which yielded an average velocity at the wall that varied between 4–8% of the rotor tip speed; see Fig. 3.27.

Figure 3.27 shows the phase-averaged measurements of the radial flow velocity parallel to the wall for each of the four blade tips at several downstream distances (see Fig. 3.17). Phase-averaging the velocity profiles removed the stochastic aspects of the flow field (localized turbulence and coherent tip vortices) producing a good estimate of the average velocities near the ground. The velocity gradient $\partial u/\partial z$ near the ground is directly proportional to the shear stresses experienced on the surface of the ground plane, i.e., $\tau_v = \mu(\partial u/\partial z)$; see Fig. 3.26. It is, therefore, important to note that in this case the velocity gradients near the wall are quite steep, which results in large values of shear stress on the ground.

As the measurement plane is moved further downstream, the shear layer moved closer to the ground and the resulting flow begins to develop into what resembles a wall jet; see Fig. 3.28. The shear layer thickness is decreased initially because as the flow increases in velocity along the ground plane, conservation of mass dictates the associated area of the flow must be reduced. It is interesting to note that the flows with all four blade tips approached the same maximum flow velocity at $r/R = 1.6$, which was about 2.25

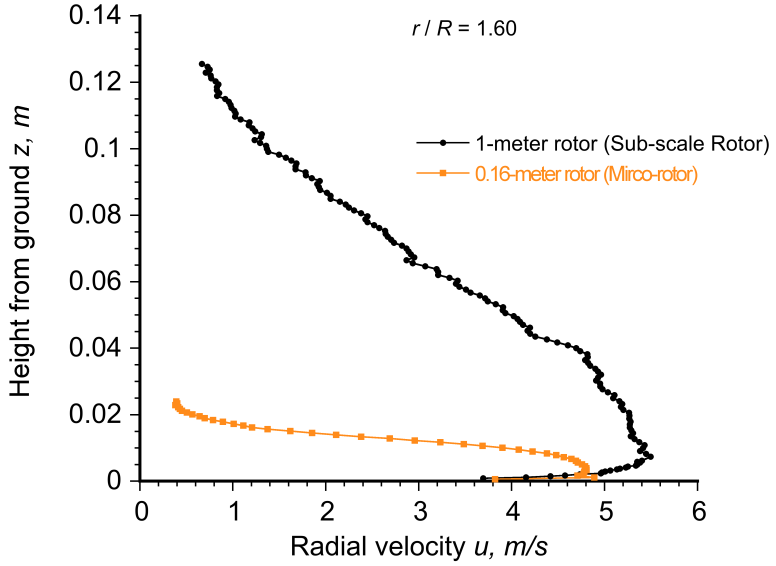

(a) Dimensional

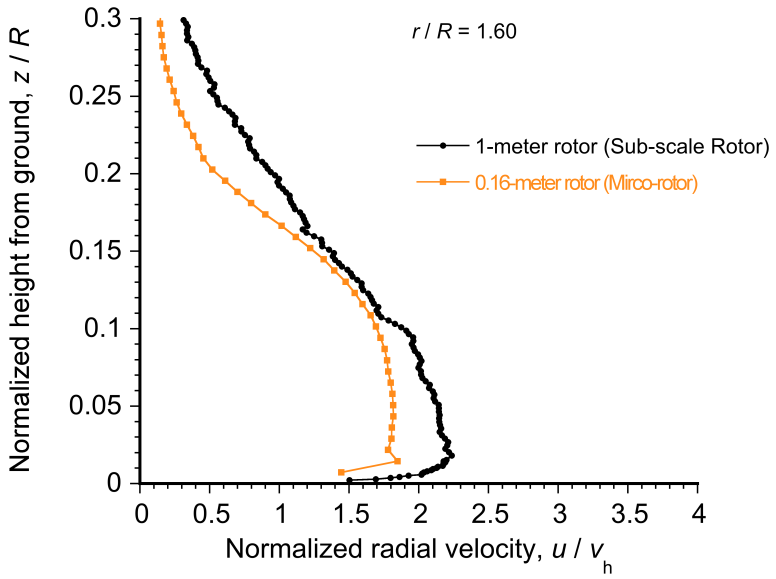

(b) Non-dimensional

Figure 3.20: Comparison of wall parallel velocity profiles for a small scale ($R = 0.08$ m) and larger scale ($R = .405$ m) rotor: (a) Dimensional; (b) Non-dimensional.

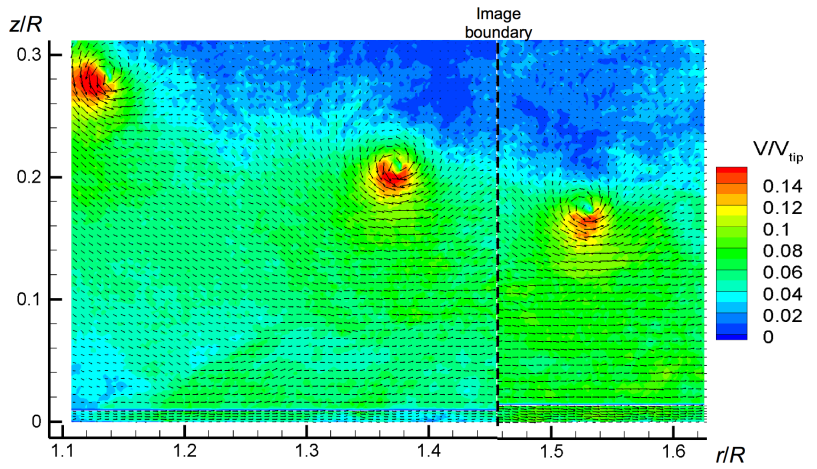

Figure 3.21: PIV results for the flow at the ground: Rectangular tip. Background contours based on the instantaneous total velocity.

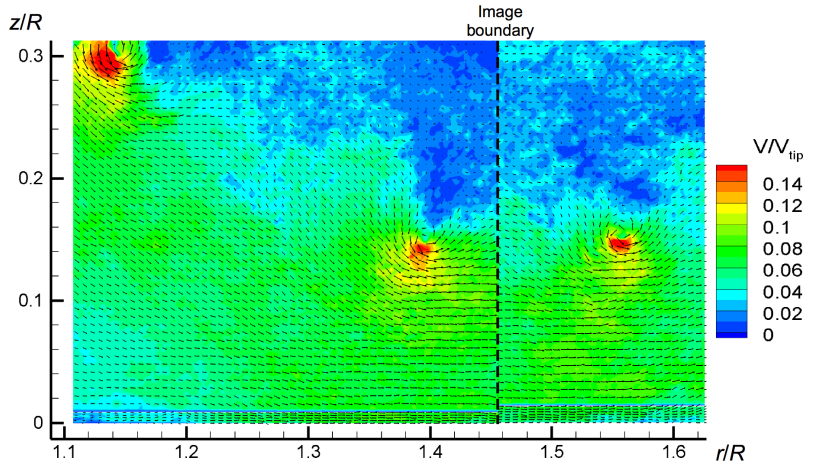

Figure 3.22: PIV results for the flow at the ground: Swept tip. Background contours based on the instantaneous total velocity.

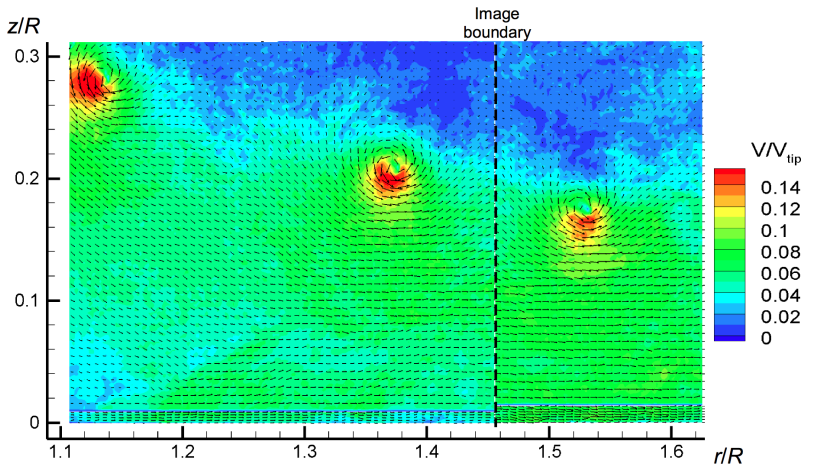

Figure 3.23: PIV results for the flow at the ground: BERP-like tip. Background contours based on the instantaneous total velocity.

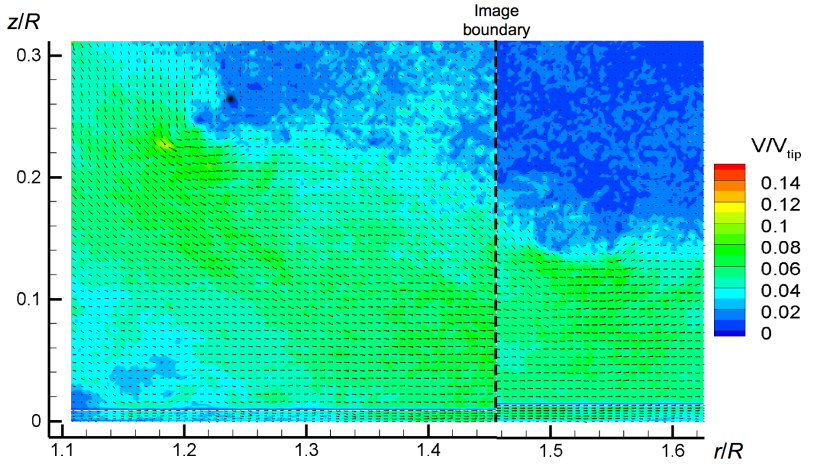

Figure 3.24: PIV results for the flow at the ground: Slotted tip. Background contours based on the instantaneous total velocity.

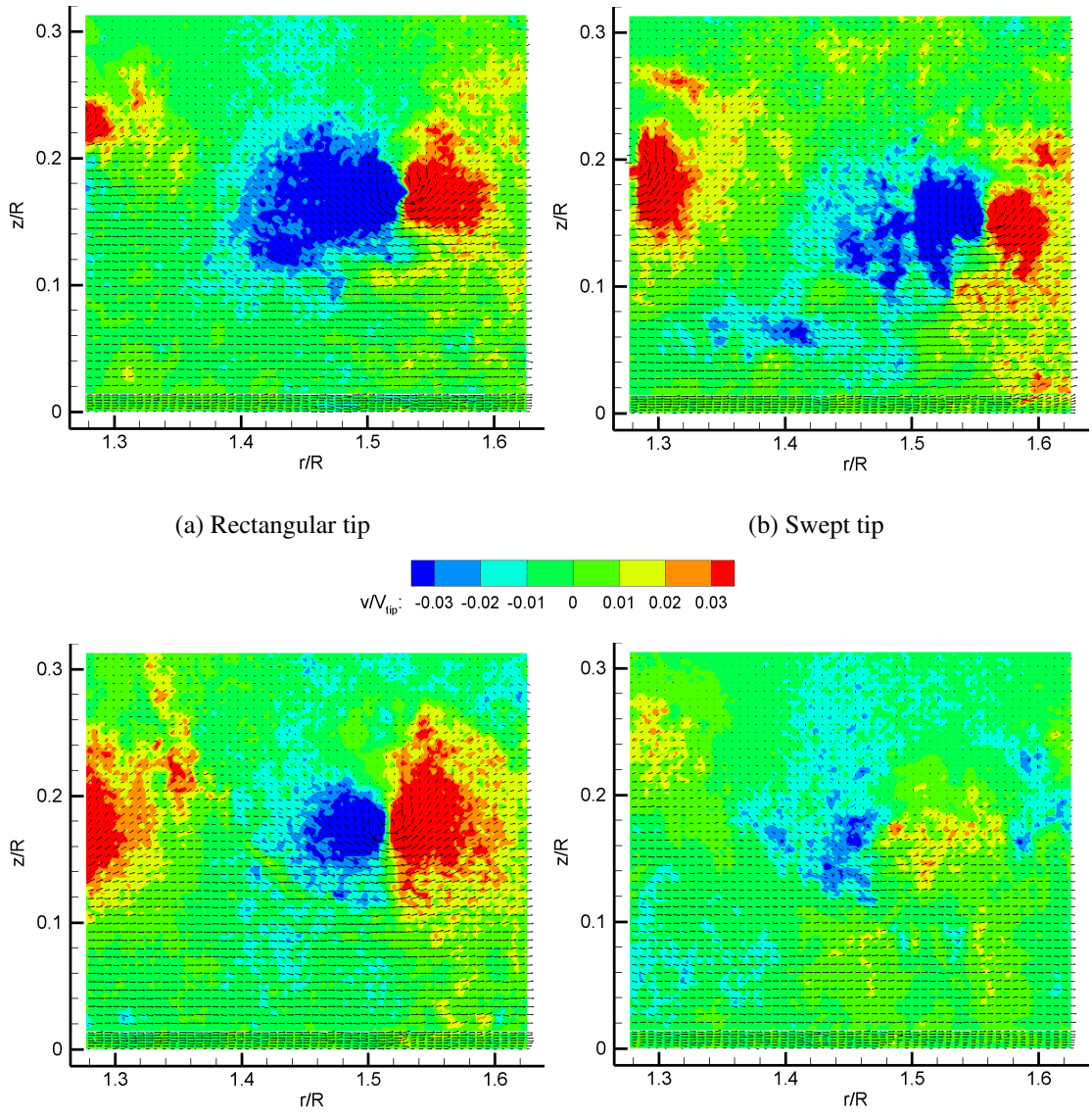

(a) Rectangular tip

(b) Swept tip

(c) BERP-like tip

(d) Slotted tip

Figure 3.25: PIV measurements of the rotor wake at the ground for each of the four blades: (a) Rectangular tip; (b) Swept tip; (c) BERP-like tip; (d) Slotted tip. Background contours are based on the instantaneous wall normal velocity.

times the average induced velocity below the rotor; see Fig. 3.28e.

Figure 3.29a shows representative velocity measurements made close to the ground. Generally, the velocity profile follows a logarithmic profile that is characteristic of a turbulent boundary layer. The velocity profiles shown in Fig. 3.29a were also converted into wall units [98] using the equations

$$z^+ = \frac{z u_\star}{\nu} \tag{3.3}$$

and

$$u^+ = \frac{u}{u_\star} \tag{3.4}$$

where z is the distance off the ground, ν is the kinematic viscosity, and the friction velocity $u_\star$ is given by

$$u_\star = \sqrt{\frac{\tau_w}{\rho}} \tag{3.5}$$

with

$$\tau_w = \mu \left(\frac{\partial u}{\partial z} \right)_{z \to 0} \tag{3.6}$$

It is interesting to note that at relatively far downstream distances the velocity profile resembles that of a classical wall jet with a viscous sublayer, and a transitional and logarithmic region [98]; see Fig. 3.29b. However, as the cutting plane is moved radially inward the velocity profiles no longer resemble a wall-jet profile because the wall bounded flow is not yet fully developed, which is shown in Fig. 3.17.

Figure 3.30 shows the corresponding instantaneous velocity profiles for the wall parallel velocity. For each blade, the instantaneous image containing the largest velocity excursions was selected. The magnitude of the flow fluctuations were found to be very

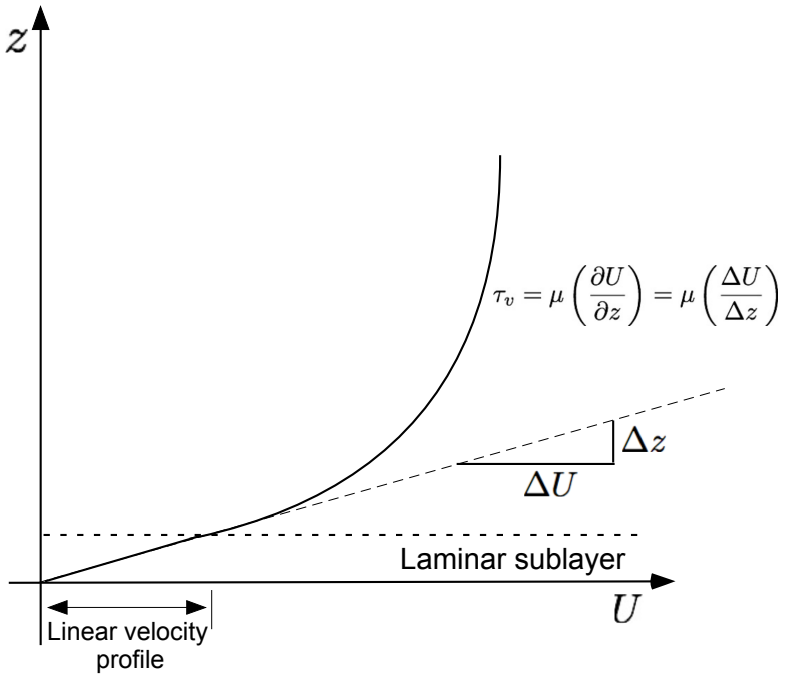

Figure 3.26: Schematic of the velocity profile and velocity gradient at the ground.

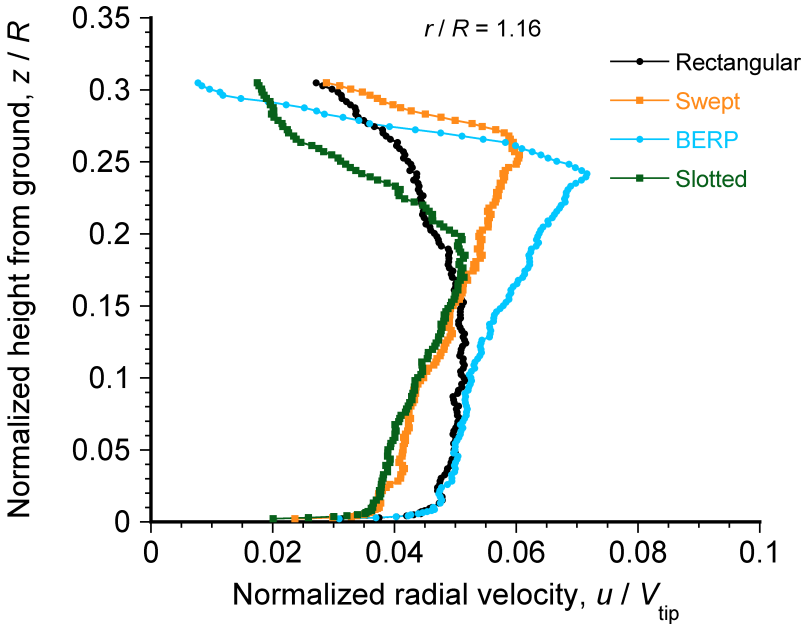

(a) $r/R = 1.16$

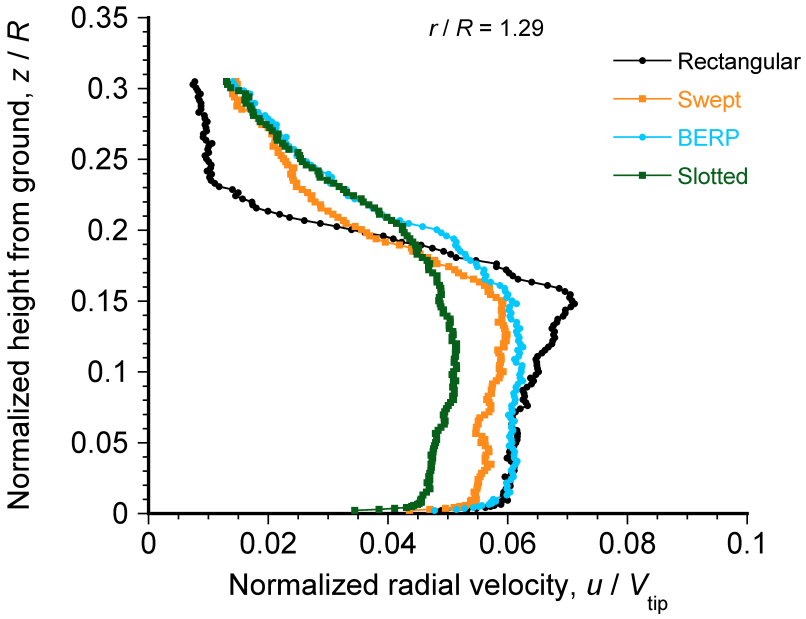

(b) $r/R = 1.29$

Figure 3.27: Phase-averaged measurements of the radial flow velocity parallel to the wall for each blade tip at several downstream distances, in this case for a blade azimuth angle of 0°: (a) $r/R = 1.16$; (b) $r/R = 1.29$; (c) $r/R = 1.40$; (d) $r/R = 1.53$; (e) $r/R = 1.60$.

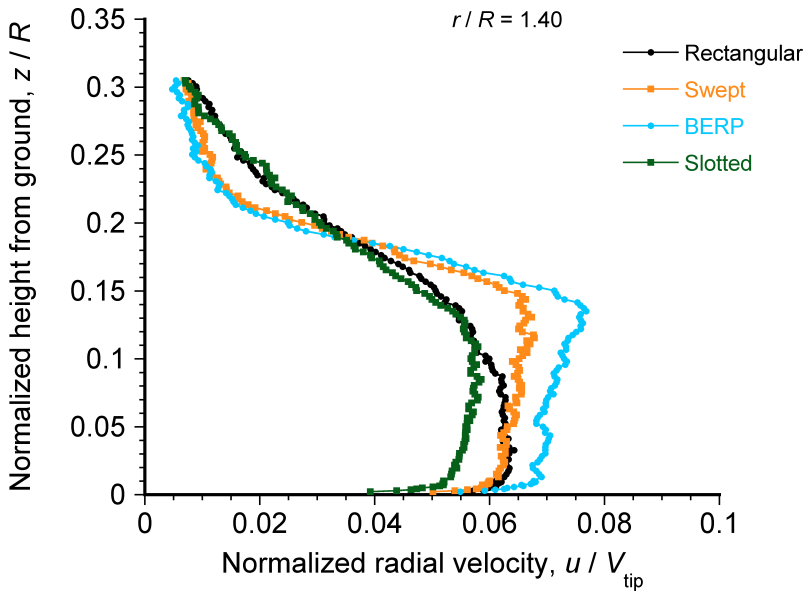

(c) $r/R = 1.40$

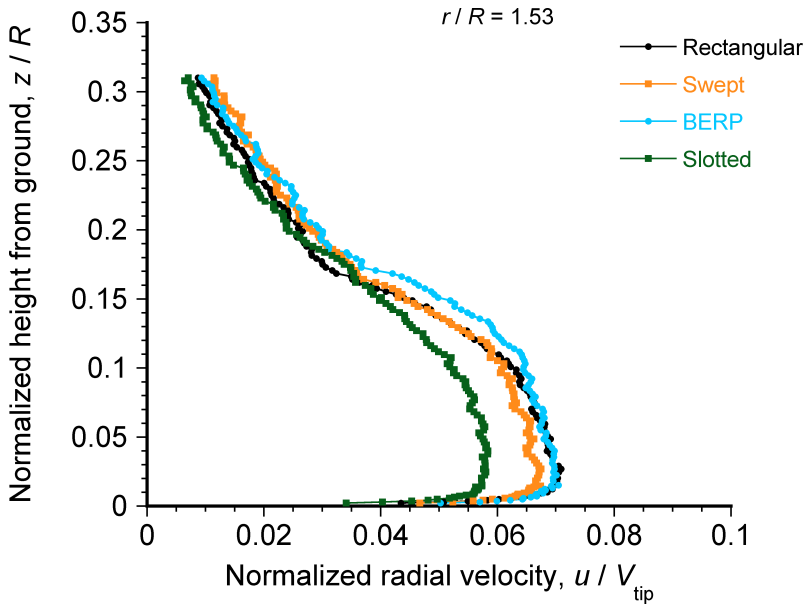

(d) $r/R = 1.53$

Figure 3.27: Phase-averaged measurements of the radial flow velocity parallel to the wall for each blade tip at several downstream distances, in this case for a blade azimuth angle of 0°: (a) $r/R = 1.16$; (b) $r/R = 1.29$; (c) $r/R = 1.40$; (d) $r/R = 1.53$; (e) $r/R = 1.60$.

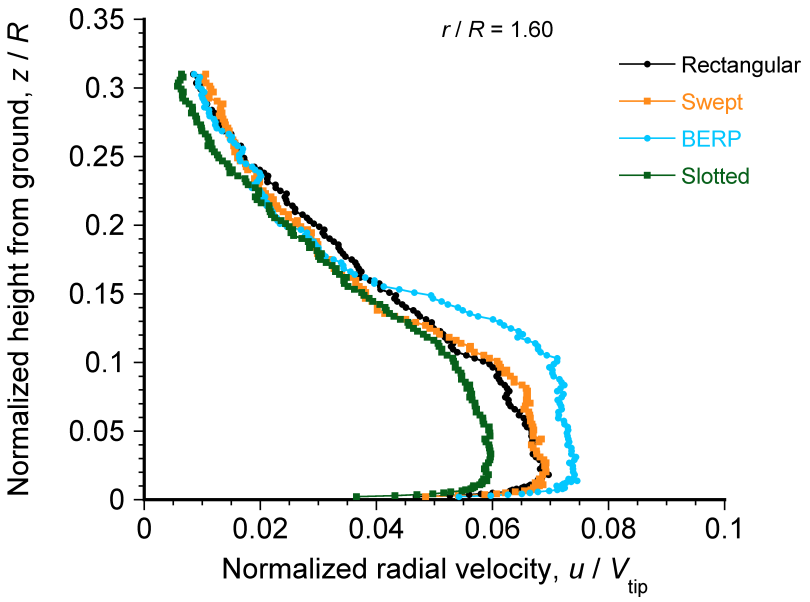

(e) $r/R = 1.60$

Figure 3.27: Phase-averaged measurements of the radial flow velocity parallel to the wall for each blade tip at several downstream distances, in this case for a blade azimuth angle of 0°: (a) $r/R = 1.16$; (b) $r/R = 1.29$; (c) $r/R = 1.40$; (d) $r/R = 1.53$; (e) $r/R = 1.60$.

similar for the rectangular, swept and BERP-like blades. The smaller fluctuations in the velocity profiles are a consequence of eddies and turbulence resulting from the interaction with the ground and the entrainment of the vortical wake sheet. Interestingly the large scale fluctuations produced by the slotted-tip were significantly smaller than those produced by the other blades, and in this case the flow near the ground appeared to be dominated by turbulence rather than by any coherent vortical structures.

Figures 3.31a and 3.32a shows the instantaneous and phase-averaged velocity profile for the rectangular blade, which is also representative of the flow produced by the swept and BERP-like tips. It is clear that the perturbations in the velocities induced by the presence of the tip vortices dominate the flow at the ground, with a magnitude that is 3–4 times that of the mean radial flow and 4–5 times the mean axial flow. For the slotted-tip blade however, Figs. 3.31b and 3.32b shows that these perturbations are mostly absent.

3.5 Near-Wall Measurements

One of the goals of the present work was to determine if the flow could be measured with sufficient detail to fully assess the characteristics of the boundary layer. An example of the detail that was ultimately achieved in the current is shown in Fig. 3.33. To limit image congestion every 5th vector was shown in the radial direction, which results in the figure appearing to have a lower spatial resolution compared to what was actually achieved. Measurements were actually obtained down to $0.001R$ ($0.009c$) off the ground plane, but below that height the surface reflections began to become more significant and it became very difficult to distinguish individual seed particles to enable successful cross-

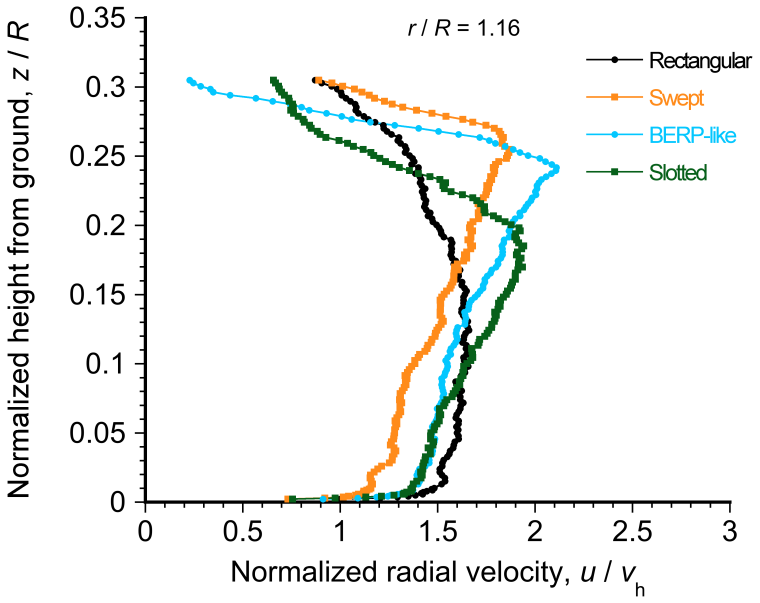

(a) $r/R = 1.16$

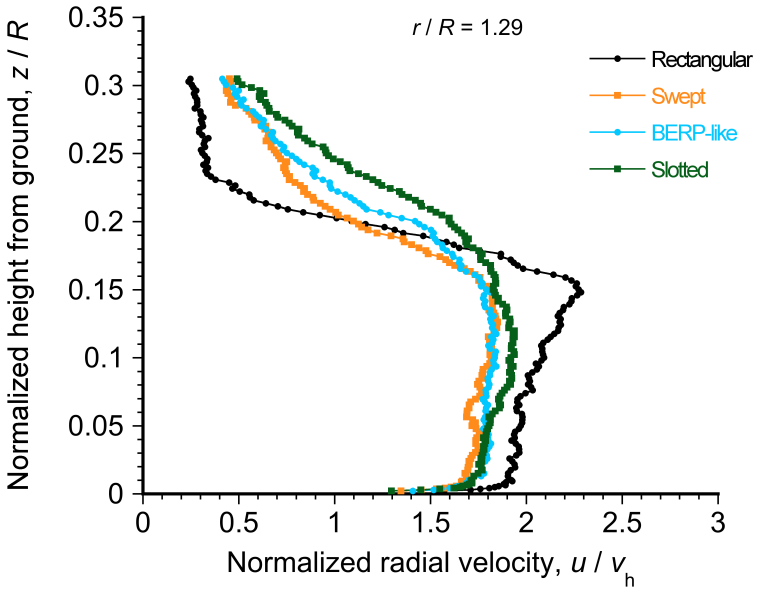

(b) $r/R = 1.29$

Figure 3.28: Phase-averaged measurements, normalized by the induced velocity, of the radial flow velocity parallel to the wall for each blade tip at several downstream distances, in this case for a blade azimuth angle of 0°: (a) $r/R = 1.16$; (b) $r/R = 1.29$; (c) $r/R = 1.40$; (d) $r/R = 1.53$; (e) $r/R = 1.60$.

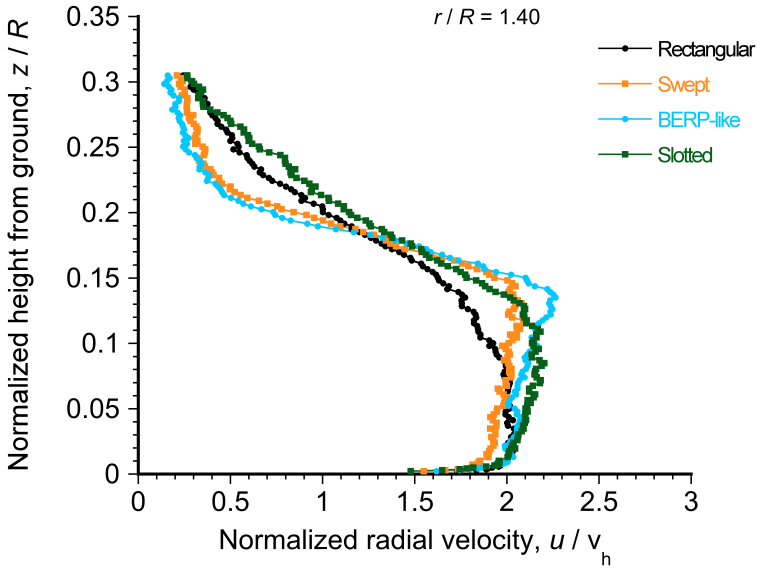

(c) $r/R = 1.40$

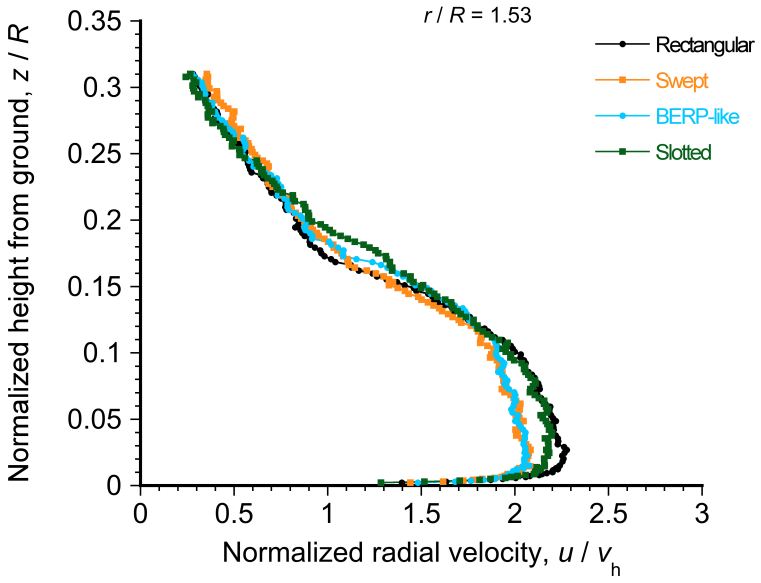

(d) $r/R = 1.53$

Figure 3.28: Phase-averaged measurements, normalized by the induced velocity, of the radial flow velocity parallel to the wall for each blade tip at several downstream distances, in this case for a blade azimuth angle of 0°: (a) $r/R = 1.16$; (b) $r/R = 1.29$; (c) $r/R = 1.40$; (d) $r/R = 1.53$; (e) $r/R = 1.60$.

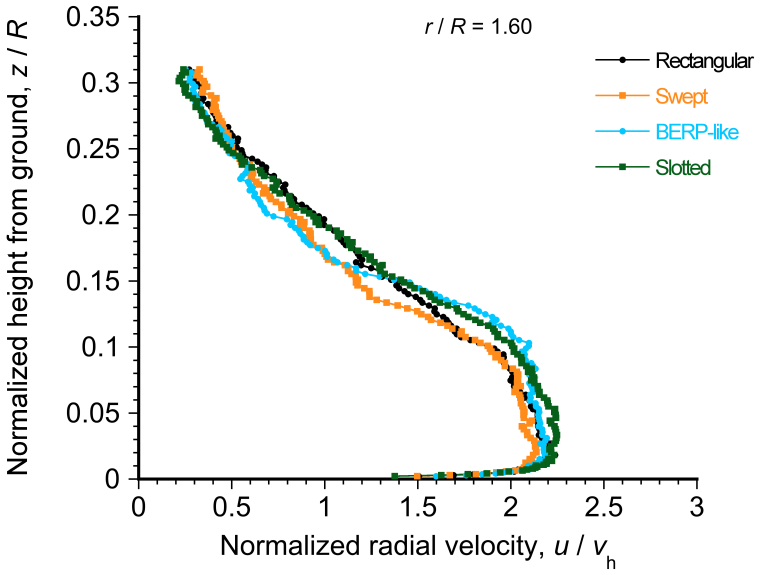

(e) $r/R = 1.60$

Figure 3.28: Phase-averaged measurements, normalized by the induced velocity, of the radial flow velocity parallel to the wall for each blade tip at several downstream distances, in this case for a blade azimuth angle of 0°: (a) $r/R = 1.16$; (b) $r/R = 1.29$; (c) $r/R = 1.40$; (d) $r/R = 1.53$; (e) $r/R = 1.60$.

correlations of the PIV image pairs.

The results in Fig. 3.33 show the locally higher flow velocities at the ground that are induced by a tip vortex in the external flow. There is also a thickening of the boundary layer over the wall, which is a consequence of the adverse pressure gradient produced by this vortex flow. In fact, the results in this case showed that the flow along the wall below the vortex was in a state of incipient separation. Boundary layer thickening resulting from the influence of a vortex was also observed by Johnson et al. [8] (formation of a separation bubble) and Geiser et al. [99] (formation of secondary vortical flow). Notice also the relatively high turbulence levels that are resolved by the PIV measurements in this case.

Figure 3.34 shows the Reynolds shear stress, $-\rho\overline{u'v'}$, at the ground normalized by the induced velocity squared, i.e. $-\overline{u'v'}/v_h^2$, for all the blades. Reynolds stresses are primary contributors to the stresses acting on the sediment bed, and they effect bedload transport as well as sediment uplift [100]. The highest shear can be seen to occur in the shear layer. The shear layer forms along the slipstream boundary, were the high-speed flow inside the rotor wake interacts with the low-speed (mostly quiescent) flow outside the rotor wake, hence generating large velocity gradients and large values of shear. While performing a simple ensemble average will tend smooth the effects of coherent vortical structures (causing the mean flow to resemble a classical turbulent wall jet), the average flow still contained the remnants of tip vortices, which acted to increase the magnitude of the shear stress in the shear layer [101]. Additionally, the stresses can be seen to go from highly negative values in the shear layer to zero in the transition regions, and ultimately then become positive in the near wall region. Figure 3.34 shows that the magnitudes

of the Reynolds shear stresses were found to be similar for the rectangular, swept, and BERP-like blades, with only minor differences in the shape of the profile. However, the slotted-tip clearly produced lower magnitudes of turbulent shear stress near the ground.

A further analysis of the data shown in Fig. 3.34 was performed to obtain the Reynolds stress profiles in the wall normal direction; see Fig. 3.35. Downstream of the rotor at $r/R = 1.34$ the rectangular, swept, and BERP-like blade tips again, showed similar profiles, with large stresses in the shear layer and a turbulent wall flow. However, the slotted tip blade produced a flow with significantly lower Reynolds stress values in the shear layer, which can be correlated to the absence of coherent tip vortices. As the measurement plane moved downstream, the Reynolds stress values for all the blades converged to a very similar profile, resembling more a classical wall-jet [98, 102]; see in Fig. 3.35e. Because the Reynolds stresses can be strongly correlated to the mobilization and transport of sediment [18], the results shown in Fig. 3.35e would seem to indicate that at downstream distances greater than about $r/R = 1.55$ the use of the different blade tips would have very similar effects on any mobile sediment.

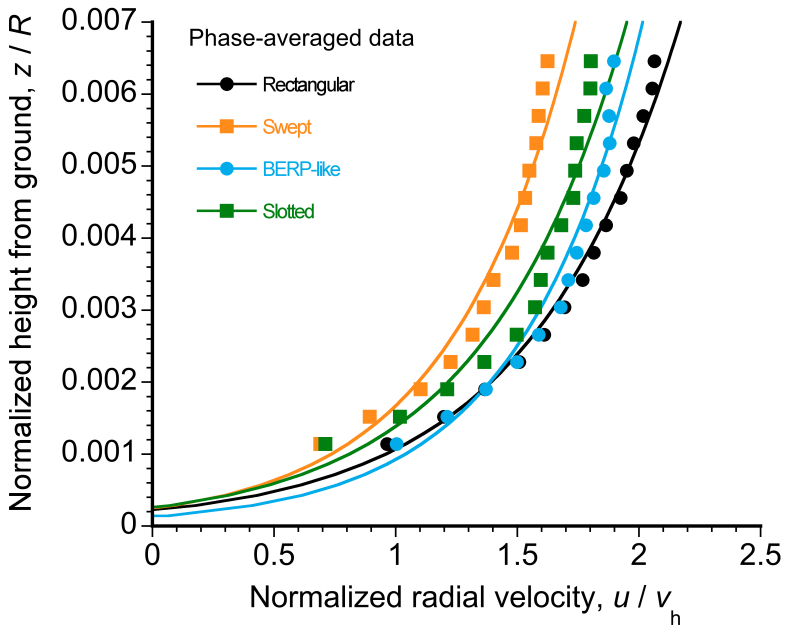

(a) Velocity profile with logarithmic curve fit

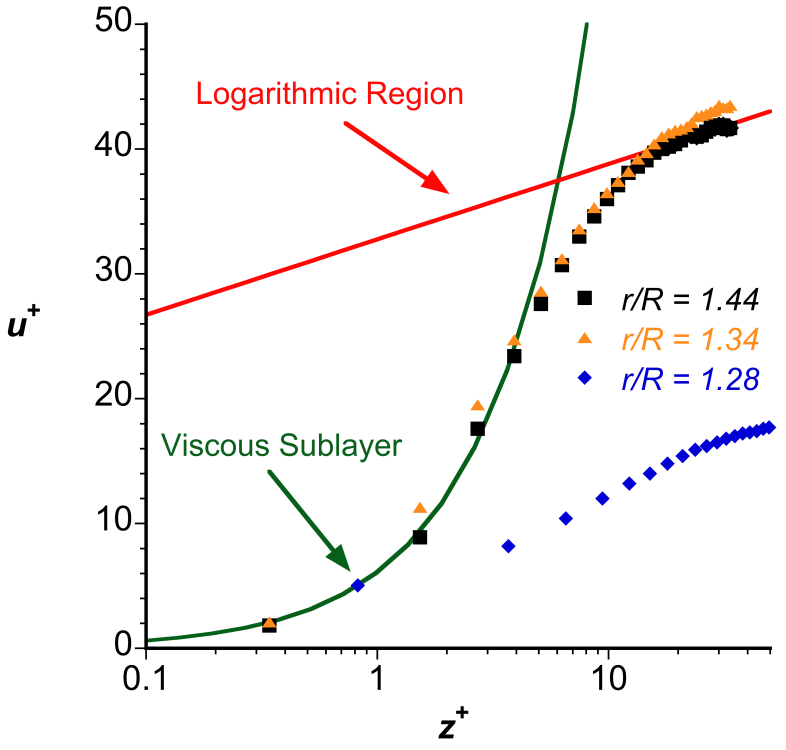

(b) Velocity profile in wall units

Figure 3.29: Close to the wall, showing the validity of the logarithmic profile: a) non-dimensional velocity profile, b) velocity profile in wall units.

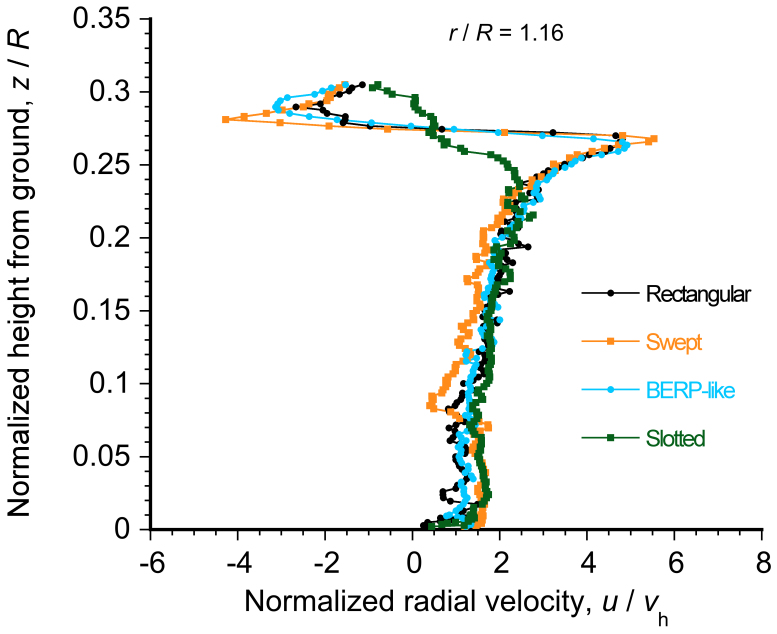

(a) $r/R = 1.16$

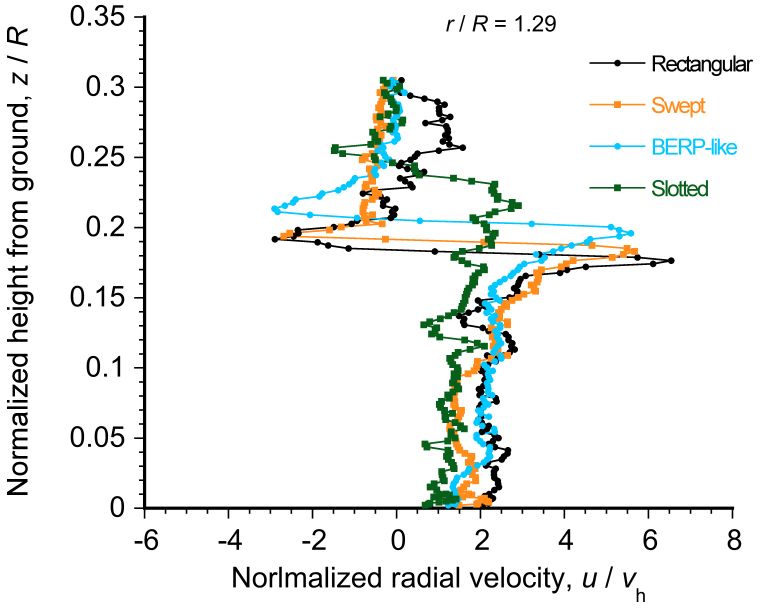

(b) $r/R = 1.29$

Figure 3.30: Instantaneous measurements of the radial flow velocity parallel to the wall for each blade tip at several downstream distances for a blade azimuth angle of 0°: (a) $r/R = 1.16$; (b) $r/R = 1.29$; (c) $r/R = 1.40$; (d) $r/R = 1.53$; (e) $r/R = 1.60$.

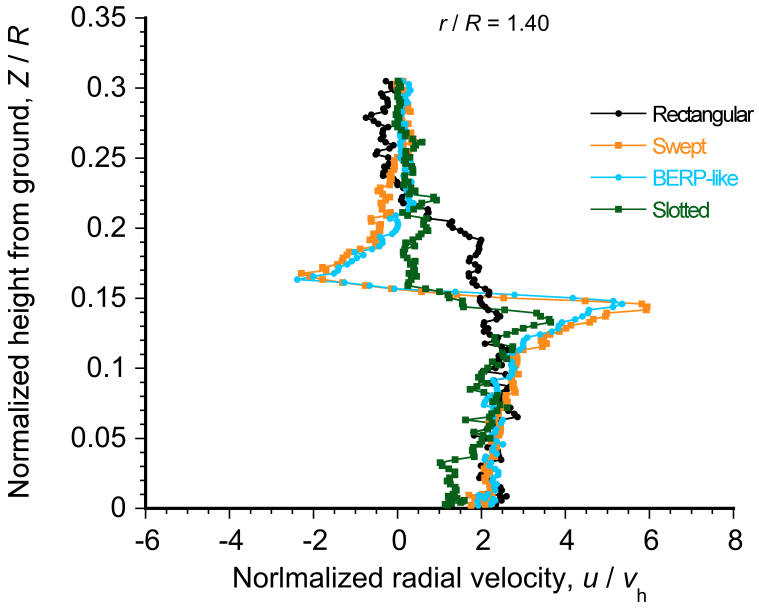

(c) $r/R = 1.40$

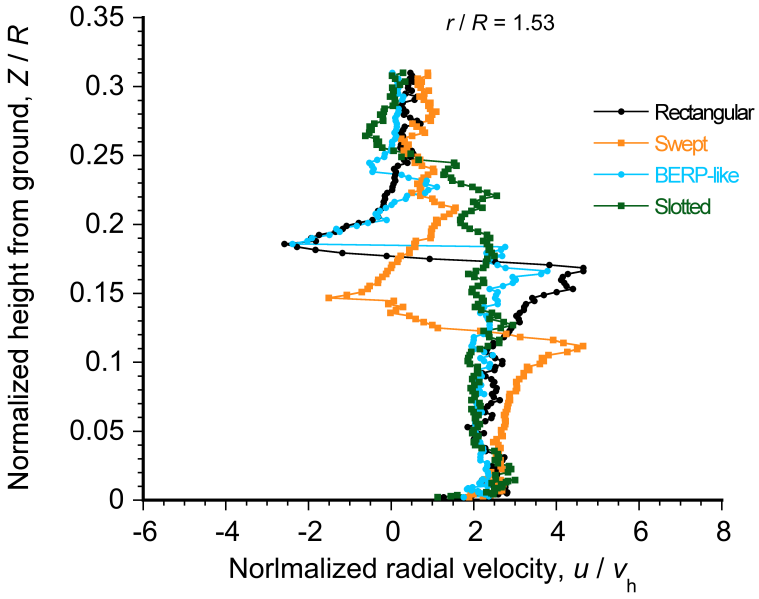

(d) $r/R = 1.53$

Figure 3.30: Instantaneous measurements of the radial flow velocity parallel to the wall for each blade tip at several downstream distances for a blade azimuth angle of 0°: (a) $r/R = 1.16$; (b) $r/R = 1.29$; (c) $r/R = 1.40$; (d) $r/R = 1.53$; (e) $r/R = 1.60$.

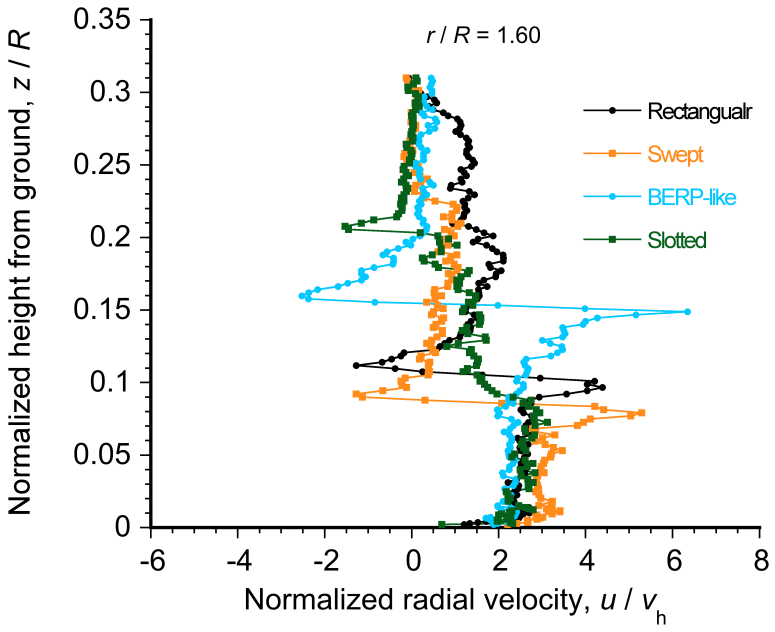

(e) $r/R = 1.60$

Figure 3.30: Instantaneous measurements of the radial flow velocity parallel to the wall for each blade tip at several downstream distances for a blade azimuth angle of 0°: (a) $r/R = 1.16$; (b) $r/R = 1.29$; (c) $r/R = 1.40$; (d) $r/R = 1.53$; (e) $r/R = 1.60$.

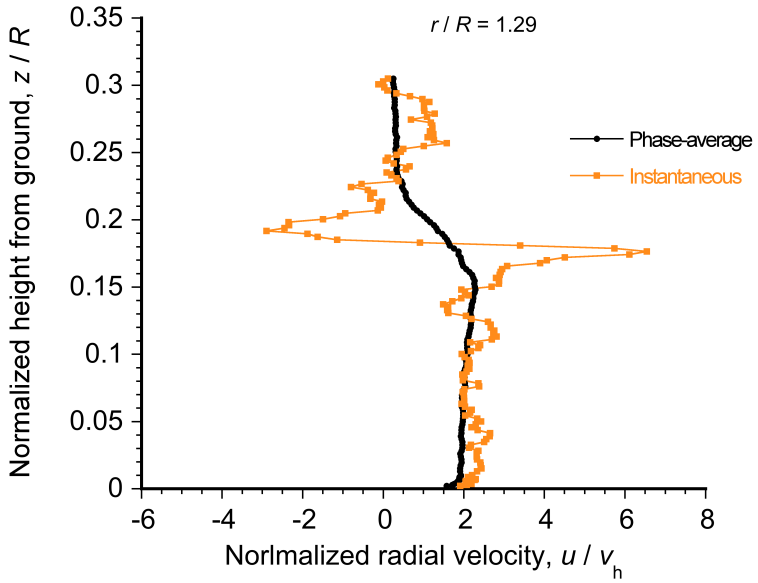

(a) Rectangular

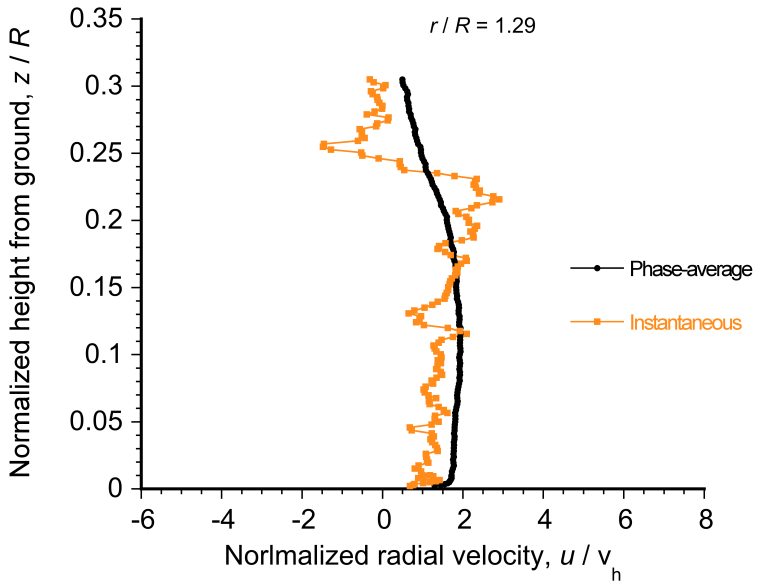

(b) Slotted

Figure 3.31: Instantaneous and phase-averaged measurements of the radial flow velocity parallel to the wall for the baseline rectangular blade at r/R = 1.29, at a blade azimuth angle of 0°: (a) Rectangular; (b) Slotted.

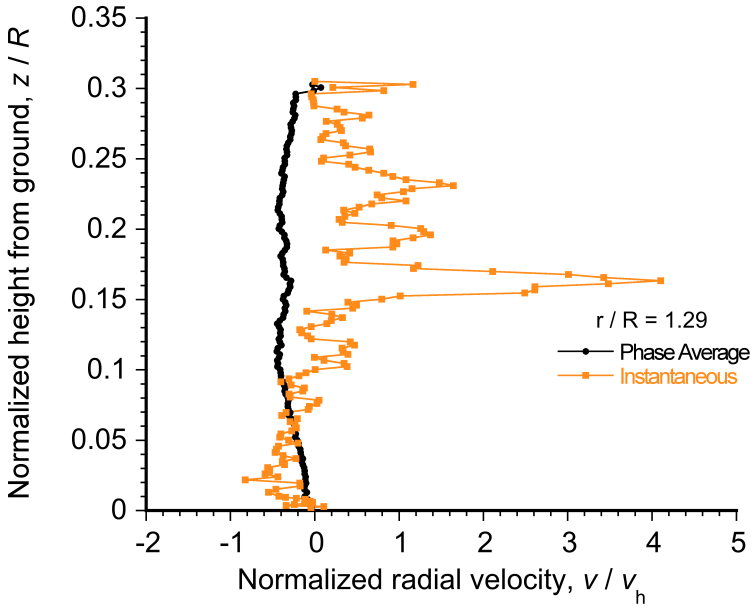

(a) Rectangular

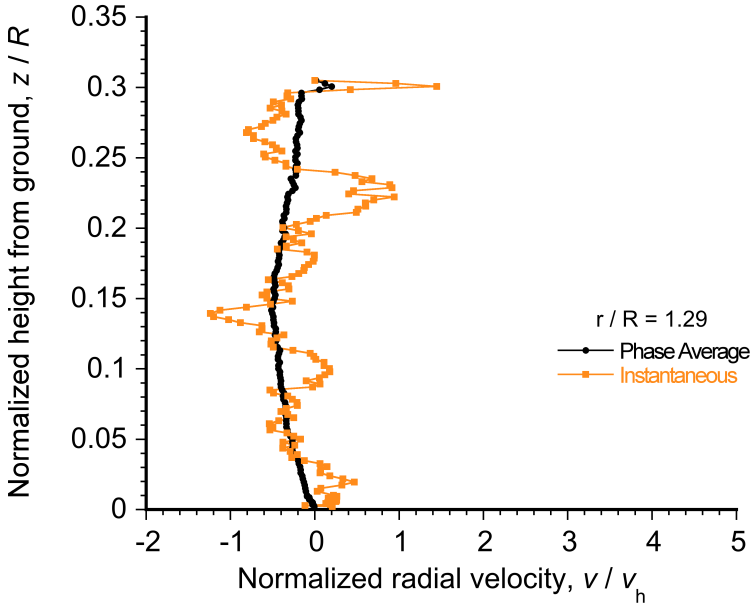

(b) Slotted

Figure 3.32: Instantaneous and phase-averaged measurements of the axial flow velocity normal to the wall at r/R = 1.29, at a blade azimuth angle of 0°: (a) Rectangular; (b) Slotted.

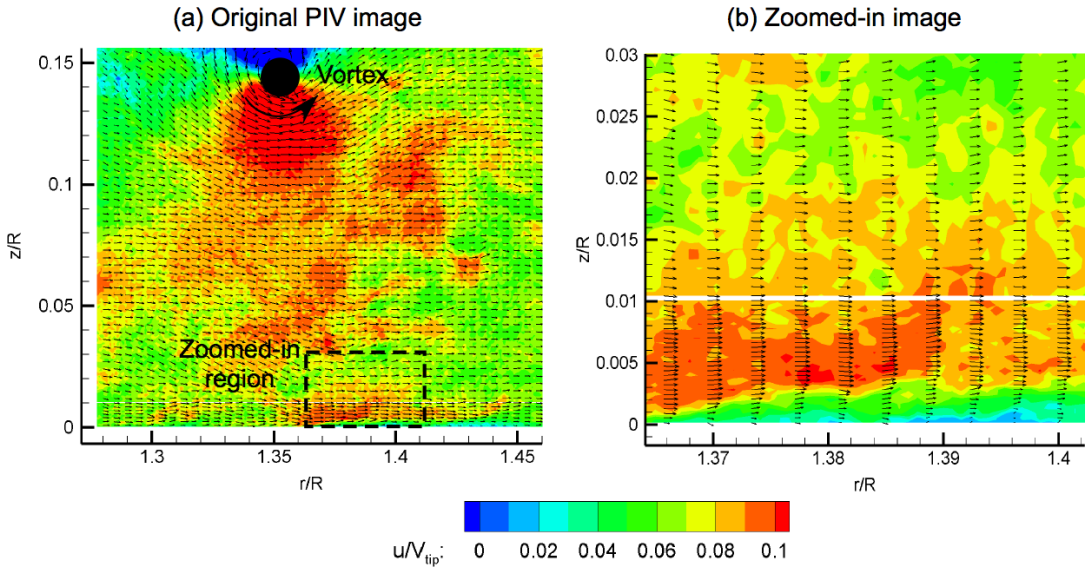

Figure 3.33: Example of the flow details resolved near the wall surface. Results show instantaneous flow vectors that were obtained with a rectangular blade. Area of zoomed-in image shown by the dashed line.

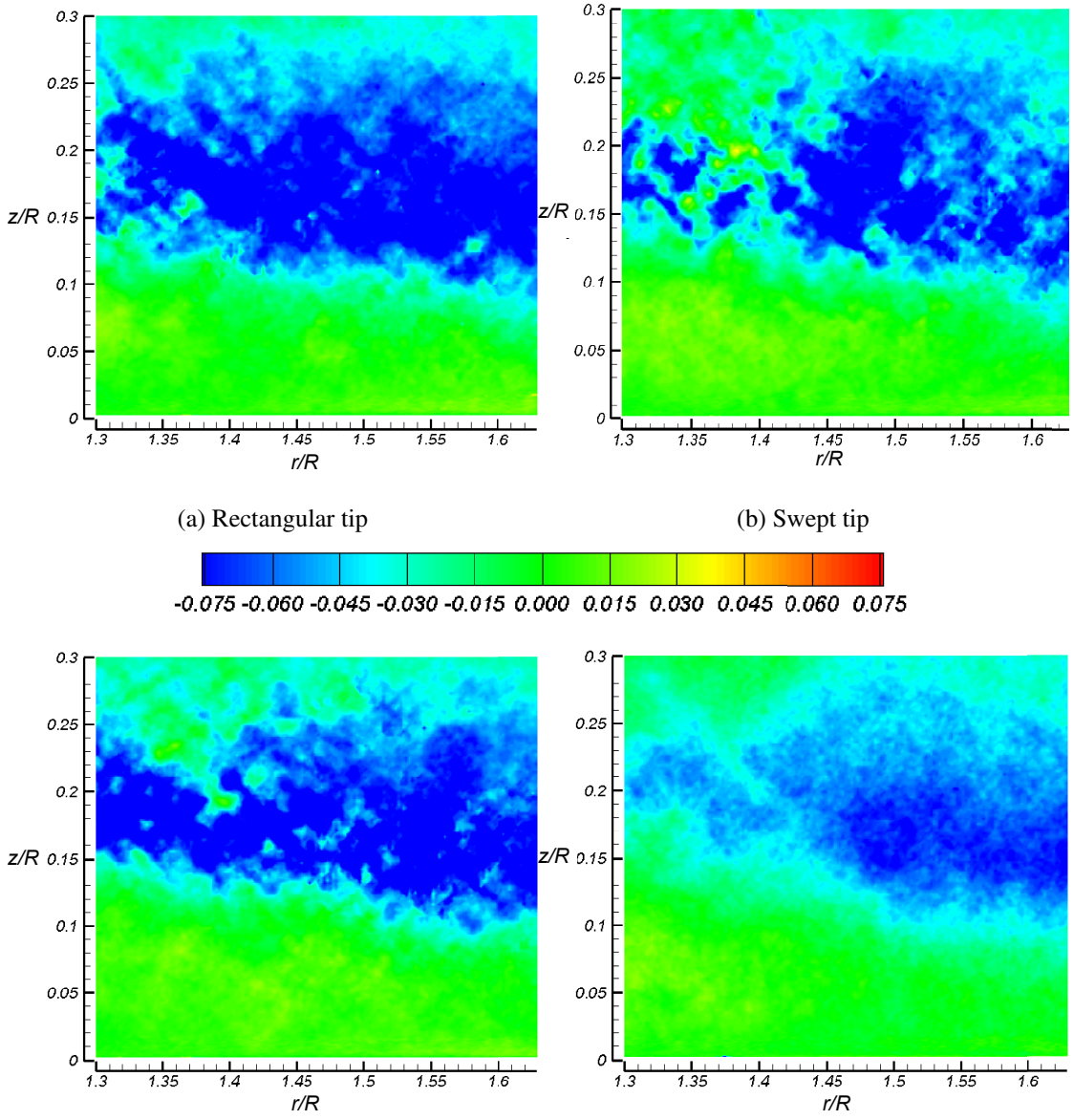

(a) Rectangular tip

(b) Swept tip

(c) BERP-like tip

(d) Slotted tip

Figure 3.34: Reynolds shear stress normalized by the induced velocity squared ($-\overline{u'v'}/v_h^2$): a) Rectangular tip, b) Swept tip, c) BERP-like tip, d) Slotted tip.

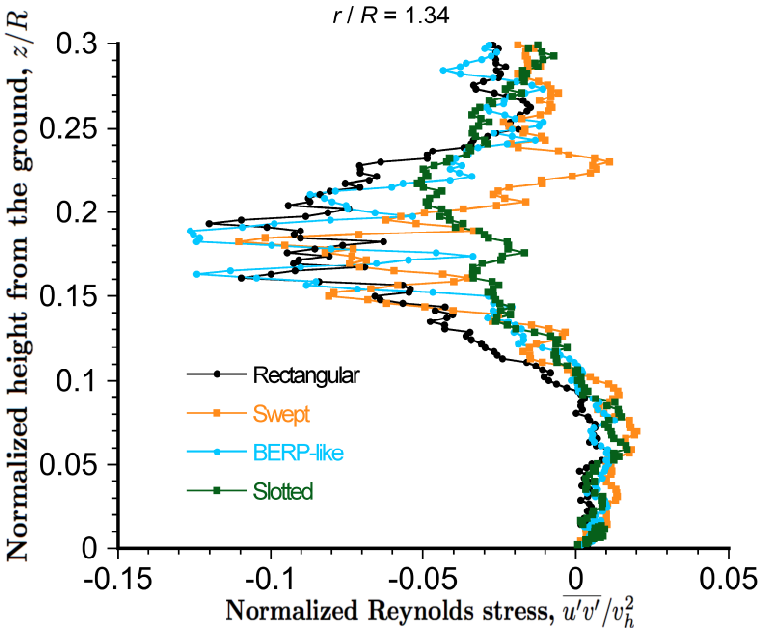

(a) $r/R = 1.34$

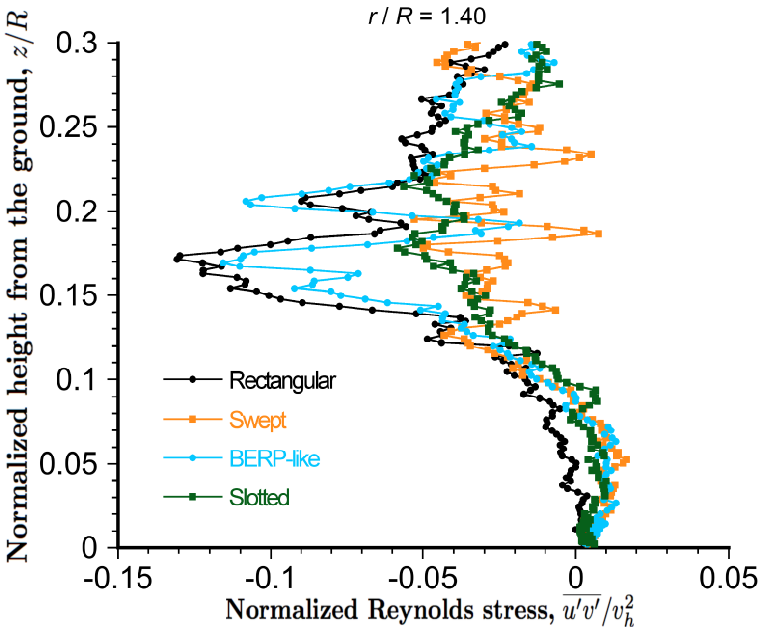

(b) $r/R = 1.40$

Figure 3.35: Measurements of normalized Reynolds stress for each blade tip at several downstream distance: (a) $r/R = 1.34$; (b) $r/R = 1.40$; (c) $r/R = 1.47$; (d) $r/R = 1.54$; (e) $r/R = 1.60$.

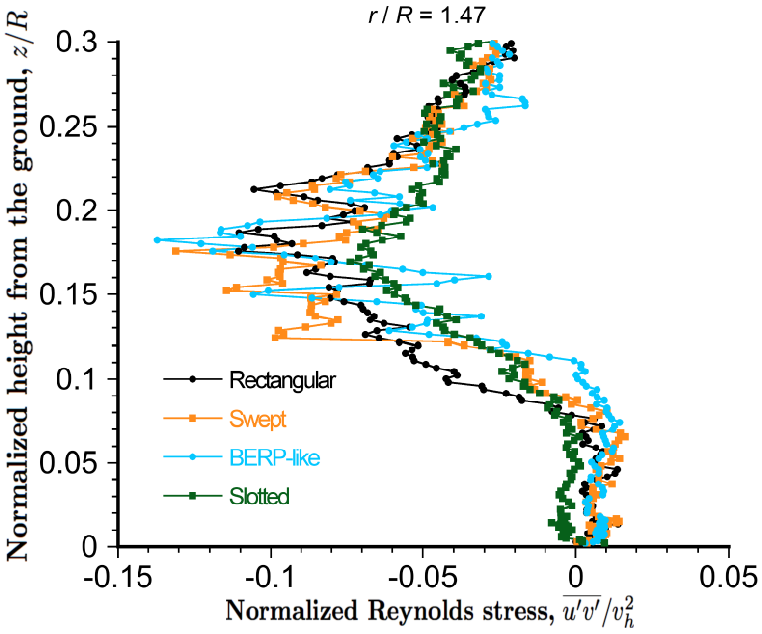

(c) $r/R = 1.47$

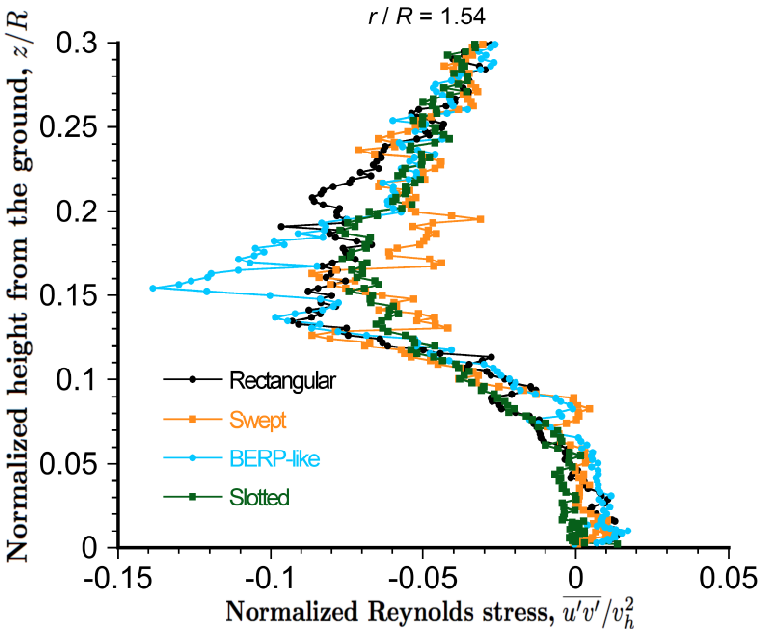

(d) $r/R = 1.54$

Figure 3.35: Measurements of normalized Reynolds stress for each blade tip at several downstream distance: (a) r/R = 1.34; (b) r/R = 1.40; (c) r/R = 1.47; (d) r/R = 1.54; (e) r/R = 1.60.

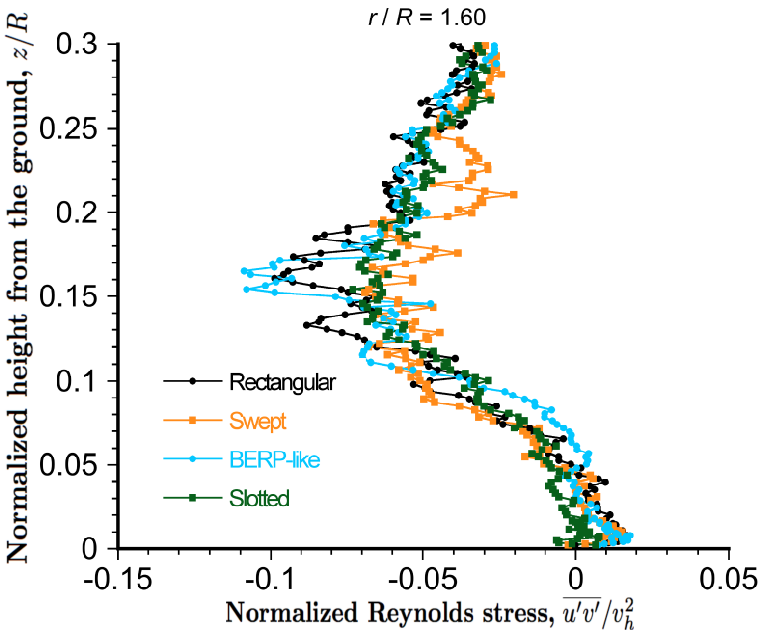

(e) $r/R = 1.60$

Figure 3.35: Measurements of normalized Reynolds stress for each blade tip at several downstream distance: (a) r/R = 1.34; (b) r/R = 1.40; (c) r/R = 1.47; (d) r/R = 1.54; (e) r/R = 1.60.

Chapter 4

Conclusions

4.1 Summary

Flow visualization and phase-resolved particle image velocimetry (PIV) experiments were conducted on a single-bladed rotor that was operating in-ground-effect to understand the fluid dynamics of the vortical rotor wake as it interacted with a horizontal ground plane. Single-bladed rotors with four different blade tips were tested: 1. A baseline rectangular tip, 2. A simple swept tip, 3. A BERP-like tip, and 4. A slotted tip. Detailed flow measurements were made in the near field of the rotor, intermediate zones where the wake began to turn and distort under the influence of the ground, and at the ground plane itself. Additionally, the work assessed the ability to perform detailed PIV measurements in regions of the flow very near a solid boundary, so as to properly resolve the characteristics of the boundary layer that would be needed to help understand the problem of rotorcraft brownout.

The following conclusions have been drawn from the research that was conducted:

1. The tip vortices generated by the rectangular, swept, and BERP-like tip blades were found to show similar flow characteristics in the initial stages after their formation. As the vortices convected in the flow, they were all shown to diffuse under the action of viscosity and (mainly) turbulence.

2. It was shown that the convecting tip vortices also interacted with their respective vortical sheets. In each case, the sheets were partially entrained into the tip vortex core regions. However, for the rectangular, swept, and BERP-like blades the turbulence that was entrained in the core from the vortical sheet was found to be relaminarized and the core regions remained mostly laminar.

3. In the near field the BERP-like blade produced a more diffused tip vortex (i.e., a lower peak swirl velocity and a larger core dimension), even though it was operating at a somewhat higher rotor thrust. The differences in the tip vortex flows seen with this blade are likely because of a modified roll-up process along the longer and highly swept side edge of the blade, although this process was not studied in detail in the present work.

4. The slotted-tip blade was found to be very effective in diffusing the vorticity contained in the tip vortex. The slots enhanced the radial diffusion of the vorticity by injecting vorticity and turbulence directly into the otherwise laminar core region of the vortex. The slotted-tip substantially reduced the swirl velocities compared to the other three blades, also reducing substantially the coherent vortical structures at older wake ages. In this case, the turbulence that was ingested into the vortex flow from the wake sheet increased the mixing process and enhanced the radial diffusion of the vorticity.

5. When the vortices produced by the rectangular, swept, and BERP-like tip blades interacted with the ground the vortex filaments were stretched causing the vorticity to reintensify and increasing the peak swirl velocities. The process of filament

stretching when the rotor was in ground effect operations was noted to cause the vortices to persist for five to six rotor revolutions.

6. Despite the differences in the vortex characteristics of the rectangular, swept, and BERP-like tip blades at early wake ages, the flow fields near the ground (at wake ages between two and three rotor revolutions) were found to be relatively similar (i.e., in terms of their swirl velocities and vortex core sizes). However, the vortices produced by the slotted-tip blade were much more diffused than for the other three blades.

7. An unsteady turbulent wall-jet type of flow was found to develop along the ground plane below the rotor. This flow contained coherent vortices trailed from the blade tip and eddies and turbulence originating from the vortical wake sheet. Interactions between these flow structures was seen to dominate the unsteady aerodynamic environment near the ground. The slotted-tip was found to be effective at diffusing the coherent tip vortices, thereby reducing the overall intensity of the velocity excursions seen at the ground.

8. Further downstream along the ground plane the four blades were found to produce generally similar flows (i.e., velocity profiles, and Reynolds stresses), with the profiles generally resembling a classical wall-jet. However, upstream the flow field was influenced significantly by the convecting tip vortices, causing the stresses to increase along the slipstream boundary (i.e., in the shear layer). Again, the rectangular, swept, and BERP-like tips were found to produce very similar flows, while the slotted more closely resembled the fully developed flow downstream. The dif-

ferences between the flow produced by the slotted-tip and the other three blades arised because of the more significantly diffused vortices produced in this case.

4.2 Suggestions for Future Work

The work that has been done to study the flow generated by various blade tip shapes has provided a new understanding into the aerodynamics of rotors operating in-ground-effect. The tip vortex characteristics have been measured versus wake age for each blade tips. However, there are still several areas of further investigation that could be perused to provide a better understanding of the effect of blade tip on the flows generated by a rotor operating in-ground-effect.

As previously discussed four different blade tip shapes (rectangular, simple swept, BERP-like, and slotted) have been studied in the present work. However, there are additional blade tip shapes that could be examined, such as more complex swept planforms (varying sweep angle), tapered, sub-wing, etc. Furthermore, twist and anhedral affect the performance of the rotor system may ultimately affect the structure of the developing rotor wake in-ground-effect [89]. Therefore, additional measurements of rotor with different values of blade twist should be examined, along with varying amounts of anhedral. Such measurements could provide further insight into the nature of the rotor wake and the effect tip shape has on the flow field at the ground.

The measurements resolution of the flow characteristics was limited by the number of experiments that were required and the volume of data that could be practically stored. In the current work measurements were taken at increments of $\approx 30^{\circ}$, which could be

reduced to obtain measurements with greater temporal fidelity.

While the single-bladed measurements performed in the current work offered advantages over multi-bladed rotors (namely increased spatial and temporal stability [78, 79]), additional experiments will be required to examine the effects of multiple blades (e.g., 2, 3, 4 blades etc.). Studies performed by Johnson et al. [8] and Sydney et al. [9] have found that the vortices trailed from a two-bladed rotor operating in-ground-effect had a propensity to pair and merge. Pairing was observed in the current work, but not to any significant degree. However, vortex pairing and merging is really the reality of the real rotor problem, which can alter the flow at the ground [8].

For the current measurements a height of one rotor radius from the ground plane was chosen because it presented a realistic IGE operating condition and had been shown to significantly influence the developing rotor wake [29]. However, the structure and development of the rotor wake changes drastically as a rotor transitions from OGE to IGE conditions [29]. Therefore, additional experiments will be required to examine the affect of blade tip shape for different rotor heights off the ground to determine the effects produced.

Appendix A

Q-criterion Algorithm

The Q-criterion is defined as the discriminant of the velocity gradient tensor as given by

$$Q = \frac{1}{4}S^2 - q \tag{A.1}$$

where S is the trace of the velocity gradient tensor given by

$$S = \frac{\partial u}{\partial x} + \frac{\partial v}{\partial x} \tag{A.2}$$

and q is the determinate of the velocity gradient tensor given by

$$q = \frac{\partial u}{\partial x}\frac{\partial v}{\partial y} - \frac{\partial u}{\partial y}\frac{\partial v}{\partial x} \tag{A.3}$$

The velocity gradients were calculated using Richardson extrapolation as given by

$$\left(\frac{\partial f}{\partial x_i}\right) \approx \frac{f_{i-2} - 8f_{i-1} + 8f_{i+1} - f_{i+2}}{12\Delta X} \tag{A.4}$$

The Richardson extrapolation method provided an accuracy of $O(\Delta X^3)$ and an uncertainty of $\approx 0.95\varepsilon/\Delta X$.

Bibliography

[1] Mapes, P., Kent, R., Wood, R., "DoD Helicopter Mishaps FY85-05: Findings and Recommendations," U.S. Air Force, 2008.

[2] NTSB, "Briefs: LAX01LA283, LAX01LA304, LAX04LA285, SEA05CA173, LAX08LA198," National Transportation Safety Board, 2001, 2004, 2005, 2009.

[3] Jansen, C., Wennemers, A., and Groen, E., "FlyTact: A Tactile Display Improves a Helicopter Pilots Landing Performance in Degraded Visual Environments," *Haptics: Perception, Devices and Scenarios*, Vol. 5024, 2008, pp. 867–875

[4] "Sandblaster 2 Support of See-Through Technologies for Particulate Brownout," Task 1 Technical Report, Sponsored by Defense Advanced Research Projects Agency (DOD) Strategic Technology Office, Issued by U.S. Army Aviation and Missile Command Under Contract No. W31P4Q-07-C-0215, MRI Project No. 110565, October 31, 2007.

[5] "Sandblaster 2 Support of See-Through Technologies for Particulate Brownout," Task 5 Final Technical Report, Sponsored by Defense Advanced Research Projects Agency (DOD) Strategic Technology Office, Issued by U.S. Army Aviation and Missile Command Under Contract No. W31P4Q-07-C-0215, MRI Project No. 110565, October 31, 2007.

[6] Wong, O. D., and Tanner, P. E., "Photogrammetric Measurements of an EH-60L Brownout Cloud," 66th Annual Forum of the American Helicopter Society, Phoenix, AZ, May 11–13, 2010.

[7] Milluzzo, J., and Leishman, J. G., "Assessment of Rotorcraft Brownout Severity in Terms of Rotor Design Parameters,? Journal of the American Helicopter Society, Vol. 55, (3), October 2010

[8] Johnson, B., Leishman, J. G., Sydney, A., "Investigation of Sediment Entrainment in Brownout Using High-Speed Particle Image Velocimetry," American Helicopter Society 65th Annual Forum Proceedings, Grapevine, TX, May 27–29, 2009.

[9] Sydney, A., Baharani, and A., Leishman, J. G., "Understanding Brownout Using Near-Wall High-Speed Dual-Phase Flow Measurements," American Helicopter Society 67th Annual Forum Proceedings, Virginia Beach, VA, May 3–5, 2011.

[10] Leishman, J. G., "Challenges in Understanding the Fluid Dynamics of Brownout: Review and Update," Proceedings of the AHS International Meeting on Advanced Rotorcraft Technology and Safety Operations, Omiya, Japan, Novermber 1–3 2010.

[11] Ryerson, C. C., Haehnel, R. B., Koenig, G. G., and Moulton, M. A., "Visibility Enhancement in Rotorwash Clouds," Paper AIAA-2005-263, 43rd AIAA Aerospace Sciences Meeting and Exhibit, Reno, NV, January 10–13, 2005.

[12] Morales, F. Naqvi, I., Squires, K. D., and Piomelli, U., "Euler-Lagrange Simulations of Particle Interactions with Coherent Vortices in Turbulent Boundary Lay-

ers," 62nd Annual Meeting of the Division of Fluid Dynamics, Minneapolis, Minnesota, November 2009.

[13] Morales, F. Naqvi, I., Squires, K. D., and Piomelli, U., "Euler-Lagrange Simulations of Particle Interactions with Coherent Vortices in Turbulent Boundary Layers," Bulletin of the American Physical Society, Vol. 54, No. 19, 2009.

[14] D'Andrea, A., "Numerical Analysis of Unsteady Vortical Flows Generated by a Rotorcraft Operating on Ground: A First Assessment of Helicopter Brownout," American Helicopter Society 65th Annual Forum Proceedings, Grapevine, Texas, May 27–29, 2009.

[15] Thomas, S., Lakshminarayan, V. K., Kalra, T. S., and Baeder, J. D., "Eulerian-Lagrangian Analysis of Cloud Evolution using CFD Coupled with a Sediment Tracking Algorithm," 67th Annual Forum Proceedings of the American Helicopter Society, Virginia Beach, VA, May 3–5, 2011.

[16] Syal, M., Govindarajan, B., and Leishman, J. G., "Mesoscale Sediment Tracking Methodology to Analyze Brownout Cloud Developments," 66th Annual Forum of the American Helicopter Society, Phoenix, AZ, May 10–13, 2010.

[17] Syal, M., and Leishman, J. G., "Comparisons of Predicted Brownout Dust Clouds with Photogrammetry Measurements," 67th Annual Forum Proceedings of the American Helicopter Society, Virginia Beach, VA, May 3–5, 2011.

[18] Haehnel, R. B., Moulton, M. A., Wenren, W., and Steinhoff, J., "A Model to Simulate Rotorcraft-Induced Brownout," American Helicopter Society 64th Annual Forum Proceedings, Montreal, Canada, April 29–May 1, 2008.

[19] Knight, M., and Hefner, R. A., "Analysis of Ground Effect on the Lifting Airscrew," NACA TN 835, 1941.

[20] Zbrozek, J., "Ground Effect on the Lifting Rotor," British ARC R & M 2347, 1947.

[21] Cheeseman, I. C., and Bennett, W. E., "The Effect of the Ground on a Helicopter Rotor in Forward Flight," ARC R & M 3021, 1955.

[22] Fradenburgh, E. A., "The Helicopter and the Ground Effect Machine," *Journal of the American Helicopter Society*, Vol. 5, (4), 1960, pp. 26–28.

[23] Hayden, J. S., "The Effect of the Ground on Helicopter Hovering Power Required," American Helicopter Society 32th Annual National V/STOL Forum Proceedings, Washington D.C., May 10–12, 1976.

[24] Prouty, R. W., "Ground Effect and the Helicopter," AIAA Paper 85-4034, AIAA/AHS/ASEE Aircraft Design Systems and Operations Meeting, Colorado Springs, CO, October 14–16, 1985.

[25] Fradenburgh, E. A., "Aerodynamic Factors Influencing Overall Hover Performance," AGARD-CP-111, 1972.

[26] Curtiss, H. C., Sun, M., Putman, W. F., and Hanker, E. J., "Rotor Aerodynamics in Ground Effect at Low Advance Ratios," *Journal of the American Helicopter Society*, Vol. 29, (1), 1984, pp. 48–55.

[27] Curtiss, H. C., Erdman, W., and Sun, M., "Ground Effect Aerodynamics," *Vertica*, Vol. 11, (1/2), 1987, pp. 29–42.

[28] Light, J. S., and Norman, T., "Tip Vortex Geometry of a Hovering Helicopter Rotor in Ground Effect," American Helicopter Society 45th Annual Forum Proceedings, Boston, MA, May 22–24, 1989.

[29] Lee, T. E., Leishman, J. G., and Ramasamy, M., "Fluid Dynamics of Interacting Blade Tip Vortices With a Ground Plane," American Helicopter Society 64th Annual Forum Proceedings, Montréal, Canada, April 29–May 1, 2008.

[30] Milluzzo, J., Sydney, A., Rauleder, J., and Leishman, J. G., "In-Ground-Effect Aerodynamics of Rotors with Different Blade Tips," 66th Annual Forum Proceedings of the American Helicopter Society, Phoenix, AZ, May 10–13, 2010.

[31] Ramasamy, M., Johnson, B., Huismann, T. and Leishman, J. G., "Digital Particle Image Velocimetry Measurements of Tip Vortex Characteristics Using an Improved Aperiodicity Correction," *Journal of the American Helicopter Society*, Vol. 54, 012004, 2009, pp. 1–13.

[32] Nathan, N. D., and Green R. B., "Measurements of a Rotor Flow in Ground Effect and Visualisation of the Brownout Phenomenon," American Helicopter Society 64th Annual Forum Proceedings, Montréal, Canada, April 29–May 1, 2008.

[33] Ramasamy, M., and Leishman, J. G., "Interdependence of Diffusion and Straining of Helicopter Blade Tip Vortices," *Journal of Aircraft*, Vol. 41, (5), September 2004, pp. 1014–1024.

[34] Ananthan, S., Leishman, J. G., and Ramasamy, M., "The Role of Filament Stretching in the Free-Vortex Modeling of Rotor Wakes," American Helicopter Society 58th Annual National Forum, Montreal, Canada, June 11–13, 2002.

[35] McAlister, K. W., "Measurements in the Near Wake of a Hovering Rotor," Proceedings of the 27th AIAA Fluid Dynamic Conference, New Orleans, June 18–20, 1996.

[36] Boisard, R., and Baeder, J. D., "Impact of Three-Dimensional and Compressible Effects of Blade Loading on BVI Noise Signature," American Helicopter Society 57th Annual National Forum, Washington D.C, May 9–11 2001.

[37] Berry, J., and Bettschart, N., "Rotor-Fuselage Interaction: Analysis and Validation with Experiment," American Helicopter Society 53rd Annual National Forum, Virginia Beach, VA, April 29–May 1, 1997.

[38] Bagai, A., and Leishman, J. G., "A Study of Rotor Wake Development and Wake/Body Interactions in Hover," Journal of the American Helicopter Society, Vol. 37, No. 4, October 1992, pp. 48–57.

[39] Crouse, G. L., Leishman, J. G., and Bi, N., "Theoretical and Experimental Study of Unsteady Rotor/Body Aerodynamic Interactions," Journal of the American Helicopter Society, Vol. 37, No. 1, January 1992, pp. 55–65.

[40] Drees, J. M., and Hendal, W. P., "The Field of Flow Through a Helicopter Rotor Obtained from Wind Tunnel Smoke Tests," *Journal of Aircraft Engineering*, Vol. 23, (266), February 1950, pp. 107–111.

[41] Landgrebe, A. J., "An Analytical Method for Predicting Rotor Wake Geometry," Presented at the AIAA/AHS VTOL Research, Design & Operations Meeting, Atlanta, GA, February 1969.

[42] Cook, C. V.,"The Structure of the Rotor Blade Tip Vortex," Paper 3, Aerodynamics of Rotary Wings, AGARD CP-111, September 13–15, 1972.

[43] Tung, C., Pucci, S. L., Caradonna, F. X., and Morse, H. A., "The Structure of Trailing Vortices Generated by Model Helicopter Rotor Blades," NASA TM 81316, 1981.

[44] Egolf, T. A., and Landgrebe, A. J., "Helicopter Rotor Wake Geometry and its Influence in Forward Flight, Vol. 1 – Generalized Wake Geometry and Wake Effects in Rotor Airloads and Performance," NASA CR-3726, October 1983.

[45] Johnson, W., "Wake Model for Helicopter Rotors in High Speed Flight," NASA CR-1177507, USAVSCOM TR-88-A-008, November 1988.

[46] Leishman, J. G., and Bi, N., "Measurements of a Rotor Flowfield and the Effects on a Body in Forward Flight," *Vertica*, Vol. 14, (3), 1990, pp. 401–415.

[47] Lorber, P. F., Stauter, R. C., Pollack, M. J., and Landgrebe, A. J., "A Comprehensive Hover Test of the Airloads and Airflow of an Extensively Instrumented Model Helicopter Rotor," Vol. 1–5, USAAVSCOM TR-D-16 (A-E), October 1991.

[48] Bagai, A., Moedersheim, E., and Leishman, J. G., "Developments in the Visualization of Rotor Wakes using the Wide-Field Shadowgraph Method," *Journal of Flow Visualization & Image Processing*, Vol. 1, (3), July–September 1993, pp. 211–233.

[49] Bhagwat, M. J., and Leishman, J. G., "Stability Analysis of Helicopter Rotor Wakes in Axial Flight," Journal of the American Helicopter Society, Vol. 45, (3), July 2000, pp. 165–178.

[50] Ringler, T. D., George, A. R., and Steele, J. B., "The Study of Blade-Vortex Interaction Sound Generation and Directionality," Proceedings of the AHS Technical Specialists Meeting, Philadelphia, PA, October 1991.

[51] Leishman, J. G., "Aeroacoustics of 2-D and 3-D Blade Vortex Interaction Using the Indicial Method," American Helicopter Society 52nd Annual Forum, Washington, DC, June 4–6, 1996.

[52] Lim, J., and Tung, C., "2GCHAS Predictions of HART Blade-Vortex Interaction Loading," Proceedings of the AHS Technical Specialists, Meeting for Rotorcraft Acoustics and Aerodynamics, Williamsburg, VA, October 28–30, 1997.

[53] Bagai, A., and Leishman, J. G., "Flow Visualization of Compressible Vortex Structures Using Density Gradient Techniques," *Experiments in Fluids*, Vol. 15, No. 6, October 1993, pp. 431–442.

[54] Caradonna, F., Hendley, E., Silva, M., Huang, S., Komerath, N., Reddy, U., Mahalingam, R., Funk, R., Wong, O., Ames, R., Darden, L., Villareal, L., and Gregory, J., "An Experimental Study of a Rotor in Axial Flight," Proceedings of the

AHS Technical Specialists' Meeting for Rotorcraft Acoustics and Aerodynamics, Williamsburg, VA, October 28–30, 1997.

[55] Leishman, J. G., Han, Y. O., and Coyne, A. J., "Measurements of the Velocity and Turbulence Structure of a Rotor Tip Vortex," *AIAA Journal*, Vol. 35, (3), March 1997, pp. 477–485.

[56] Mahalingam, R., and Komerath, N. M., "Measurements of the Near Wake of a Rotor in Forward Flight," AIAA Paper 98-0692, 36th Aerospace Sciences Meeting & Exhibit, Reno, NV, January 12–15, 1998.

[57] Martin, P. B., and Leishman, J. G., "Trailing Vortex Measurements in the Wake of a Hovering Rotor with Various Tip Shapes," Proceedings of the American Helicopter Society 58th Annual National Forum, Montréal Canada, July 11–13, 2002.

[58] Ramasamy, M., and Leishman, J. G., "Interdependence of Diffusion and Straining of Helicopter Blade Tip Vortices," *Journal of Aircraft*, Vol. 41,(5), September 2004, pp. 1014–1024.

[59] Ramasamy, M., Johnson, B., and Leishman, J. G., "Tip Vortex Measurements Using Dual Plane Digital Particle Image Velocimetry," Proceedings of the American Helicopter Society 64th Annual National Forum, Montréal Canada, April 28–30, 2008.

[60] Cotel, A. J., and Breidenthal, R. E., "Turbulence Inside a Vortex," *Physics of Fluids*, Vol. 11, (10), 1999, pp. 3026–3029.

[61] Cotel, A. J., "Turbulence Inside a Vortex: Take Two," *Physics of Fluids*, Vol. 14, (8), 2002, pp. 2933–2934.

[62] Ramasamy, M., and Leishman, J. G., "A Generalized Model for Transitional Blade Tip Vortices," *Journal of the American Helicopter Society*, Vol. 51, (1), January 2006, pp. 92–103.

[63] Bradshaw, P., "The Analogy Between Streamline Curvature and Buoyancy in Turbulent Shear Flows," *Journal of Fluid Mechanics*, Vol. 36, (1), March 1969, pp. 177–191.

[64] Bagnold, R. A., *The Physics of Blown Sand and Desert Dunes*, Dover Publications, Inc., Mineola, NY, 1941.

[65] Greeley, R., and Iversen, J. D., *Wind as a Geological Process on Earth, Mars, Venus, and Titan*, Cambridge University Press, New York, NY, 1985, Chapter 3.

[66] Greeley, R., Iversen, J. D., Marshall, J. R., and Pollack, J. B., "Aeolian Saltation Threshold: The Effect of Density Ratio," *Sedimentology*, Vol. 34, (4), 1987, pp. 699–706.

[67] Leishman, J. G., Martin, P. B. and Pugliese, G., "High Resolution Trailing Vortex Measurements in the Wake of a Hovering Rotor," *Journal of the American Helicopter Society*, Vol. 48, (1), 2003, pp. 39–52, DOI:10.4050/JAHS.48.39.

[68] Leishman, J. G., Baker, A., and Coyne, A., "Measurements of Rotor Tip Vortices Using Three-Component Laser Doppler Velocimetry," *Journal of the American Helicopter Society*, Vol. 41, No. 4, 1996, pp. 342–353.

[69] Harrison, R., Stacey, S., and Hansford, B., "BERP IV: The Design, Development and Testing of an Advanced Rotor Blade, American Helicopter Society 64th Annual Forum Proceedings, Montréal, Canada, April 29–May 1, 2008.

[70] Martin P. B., and Leishman J. G., "Trailing vortex measurements in the wake of a hovering rotor blade with various tip shapes." American Helicopter Society 58th Annual Forum Proceedings, Montreal, Canada, June 11–15, 2002.

[71] Brand, A. G., "Aerodynamic Analysis and Measurement of a Subwing Blade Tip Shape for Blade-Vortex Interaction Noise Reduction," American Helicopter Society 53rd Annual National Forum, Virginia Beach, VA, April 29–May 1, 1997.

[72] Han, O. Y., and Leishman, J. G., "Performance Measurements of a Rotor Blade With a Slotted Tip," American Helicopter Society 60th Annual Forum Proceedings, Baltimore, MD, June 2004.

[73] Han, O. Y., and Leishman, J. G., "Experimental Investigation of Tip Vortex Alleviation Using a Slotted Tip Rotor Blade," *AIAA Journal*, Vol. 42, (4), 2004, pp. 523–535.

[74] Leishman, J. G., and Han, O. Y., "Rotor Blade System With Reduced Blade-Vortex Interaction Noise," U.S. Patent 6,948,906 B2, September 27, 2005.

[75] Dancila, D. S., "Active Rotorcraft Blade Tips for Tip Vortex Core Modifications," Annual Review of the Georgia Tech Center of Excellence for Rotorcraft Technology, School of Aerospace of Engineering, Georgia Institute of Technology, Atlanta, Georgia, April 8, 2002.

[76] Vasilescu, R., and Dancila, D.S., "Modeling of Piezoelectrically Modulated and Vectored Blowing for a Wing Section," AIAA Paper 2003, The 41th AIAA, Aerospace Sciences Meeting and Exhibit, Reno, NV, Jan. 6–9, 2003

[77] Vasilescu, R., and Dancila, D.S., "Electromechanical Modeling of a Piezoelectric Actuator for Modulated/V ectored Blowing," AIAA/ASME/ASCE/AHS Structures, Structural Dynamics, and Materials Conference, Norfolk, Virginia 7–10 Apr, 2003.

[78] Martin, P. B., Bhagwat, M. J., and Leishman, J. G., "Strobed Laser-Sheet Visualization of a Helicopter Rotor Wake," 2nd Pacific Symposium on Flow Visualization and Image Processing, Honolulu, HI, 1999.

[79] Bhagwat, M. J., and Leishman, J. G., "Stability Analysis of Rotor Wakes in Axial Flight," *Journal of the American Helicopter Society*, Vol. 45, No. 3, 2000, pp. 165–178.

[80] Ramasamy, M., and Leishman, J. G., "Benchmarking PIV with LDV for Rotor Wake Vortex Flows," AIAA Journal, Vol. 45, (11), November 2007, pp. 2622–2633.

[81] Raffel, M., Willert, C., and Kompenhans, J., "Particle Image Velocimtery: A Practical Guide," *Springer*, 1st edition, Berlin, 1998.

[82] Willert, C. E., and Gharib, M., "Digital Particle Image Velocimetry," *Experiments in Fluids*, Vol. 10, (4), January, 1991, pp. 181–193.

[83] Huang, H., Dabiri, D., and Gharib, M., "On Errors of Digital Particle Image Velocimetry," *Measurement Science and Technology*, Vol. 8, (12), December, 1997, pp. 1427–1440.

[84] Leishman, J. G., "On Seed Particle Dynamics in Tip Vortex Flows," *Journal of Aircraft*, Vol. 33, (4), 1996, pp. 823–825.

[85] Scarano, F., "Iterative Image Deformation Methods in PIV," *Measurement Science and Technology*, Vol. 13, 2002, pp. R1–R19.

[86] Theunissen R., Scarano F., and Riethmuller, M. L., "On Improvement of PIV Image Interrogation Near Stationary Interfaces," *Experiments in Fluids*, Vol. 45, pp. 557–572.

[87] Ballard, J. D., Orloff, K. L., and Lueds, A., "Effect of Tip Shape on Blade Loading Characteristics and Wake Geometry for a Two-Bladed Rotor in Hover." *Journal of the American Helicopter Society*, Vol. 25, (3), 1980, pp. 30–35, DOI:10.4050/JAHS.25.30.

[88] McVeight M. A., and McHugh, F. J., "Influence of Tip Shape, Chord, Blade Number, and Airfoil on Advanced Rotor Performance," *Journal of the American Helicopter Society*, Vol. 29, (4), 1984, pp. 55–62, DOI:10.4050/JAHS.29.55.

[89] Leishman, J. G., *Principles of Helicopter Aerodynamics*, Cambridge University Press, New York, 2000.

[90] Bhagwat, M., and Leishman, J. G., "Correlation of Rotor Tip Vortex Measurements," *AIAA Journal*, Vol. 38, (2), 2000, pp. 301–308.

[91] Momayez, L., Dupont, P., and Peerhossaini, H., "Effects of Vortex Organization on Heat Transfer Enhancement," International Journal of Thermal Sciences, Vol. 43, (8), 2004, pp. 753–760.

[92] Brocklehurst, A., and Duque, E. P. N., "Experimental and numerical study of the British Experimental Rotor Programme blade," Paper AIAA-90-3008, Proceedings of the 8th AIAA Applied Aerodynamics Conference, August 20–22, 1990, Portland, OR.

[93] Ramasamy, M., Johnson, B., Huismann, T., and Leishman, J. G., "Digital Particle Image Velocimetry Measurements of Tip Vortex Characteristics Using an Improved Aperiodicity Correction," *Journal of the American Helicopter Society*, Vol. 54, (1), 2009, pp. 012004-01–012004-13.

[94] Ramasamy, M., Johnson, B., Huismann, T., and Leishman, J. G., "Procedures for Measuring the Turbulence Characteristics of Rotor Blade Tip Vortices," *Journal of the American Helicopter Society*, Vol. 54, (2), 2009, pp. 022006-1–022006-17.

[95] Vatistas, G. H., Kozel, V., and Mih, W. C., "A Simpler Model for Concentrated Vortices," *Experiments in Fluids*, Vol. 11, 1991, pp. 73–76.

[96] Glauert, M. B., "The Wall Jet," *Journal of Fluid Mechanics*, Vol. 1, 1956, pp. 625–643, doi:10.1017/S002211205600041X.

[97] Bakke, P., "An Experimental Investigation of a Wall Jet", *Journal of Fluid Mechanics*, Vol. 2, 1957, pp. 467–472, doi:10.1017/S0022112057000270.

[98] Schlichting, H., *Boundary-Layer Theory*, McGraw-Hill Book Company, New York, 1979.

[99] Geiser, S. J., "Effects of Wall Plane Topology on Vortex-Wall Interactions in a Forced Impinging Jet." Master's thesis 2010.

[100] Haehnel, R., and Dade, W. B., "Physics of Particle Entrainment Under the Influence of an Impinging Jet," Army Science Conference Proceedings, Orlando, FL, 2008.

[101] Rauleder, J., and Leishman, J. G., "Measurements of the Turbulent Flow Environment on the Ground Below a Hovering Rotor," 37th European Rotorcraft Forum, Gallarate, Italy, September 13–15, 2011.

[102] Eriksson, J. G., Karlsson, R. I., and Persson, J., "An Experimental Study of a Two-Dimensional Plane Turbulent Wall Jet," *Experiments in Fluids*, Vol. 25, 1998, pp. 50–60.